Titre: Title:	Double-Clad Fiber-Based Systems and Devices as a Therapeutic and Diagnostic Tool for Barrett's Esophagus
Auteur: Author:	Kathy Beaudette
Date:	2017
Type:	Mémoire ou thèse / Dissertation or Thesis
Référence: Citation:	Beaudette, K. (2017). Double-Clad Fiber-Based Systems and Devices as a Therapeutic and Diagnostic Tool for Barrett's Esophagus [Thèse de doctorat, École Polytechnique de Montréal]. PolyPublie. https://publications.polymtl.ca/2602/

UNIVERSITÉ DE MONTRÉAL

DOUBLE-CLAD FIBER-BASED SYSTEMS AND DEVICES AS A THERAPEUTIC AND DIAGNOSTIC TOOL FOR BARRETT'S ESOPHAGUS

KATHY BEAUDETTE
INSTITUT DE GÉNIE BIOMÉDICAL
ÉCOLE POLYTECHNIQUE DE MONTRÉAL

THÈSE PRÉSENTÉE EN VUE DE L'OBTENTION
DU DIPLÔME DE PHILOSOPHIÆ DOCTOR
(GÉNIE BIOMÉDICAL)
JUIN 2017

UNIVERSITÉ DE MONTRÉAL

ÉCOLE POLYTECHNIQUE DE MONTRÉAL

Cette thèse intitulée :

DOUBLE-CLAD FIBER-BASED SYSTEMS AND DEVICES AS A THERAPEUTIC AND DIAGNOSTIC TOOL FOR BARRETT'S ESOPHAGUS

présentée par : BEAUDETTE Kathy
en vue de l'obtention du diplôme de : Philosophiæ Doctor
a été dûment acceptée par le jury d'examen constitué de :

M. COSTANTINO Santiago, Ph. D., président
Mme BOUDOUX Caroline, Ph. D., membre et directrice de recherche
M. BOUMA Brett E., Ph. D., membre et codirecteur de recherche
M. LESAGE Frédéric, Ph. D., membre
M. DESJARDINS Adrien, Ph. D., membre externe

DEDICATION

To my husband, parents and family.

"In everyone's life, at some time, our inner fire goes out.
It is then burst into flame by an encounter with another human being.
We should all be thankful for those people who rekindle the inner spirit."
- Albert Schweitzer

ACKNOWLEDGMENTS

The work presented in this dissertation would not have been possible without the tremendous support I received in the course of my graduate studies. I would like to take the time to acknowledge here everyone that has contributed, one way or another, to the completion of my Ph.D.

I would like to thank first and foremost my Ph.D. advisors and great mentors, Profs. Caroline Boudoux and Brett E. Bouma. I would like to sincerely and deeply thank Caroline, for believing in me, even from day 1, almost 9 years ago. She is always available to share her great enthusiast and love for science. She has acted as a catalyst in my scientific and personal development, and greatly contributed to where I am today professionally. It was such a pleasure and a great privilege to share this journey with her. Thanks to her generosity, I was able to complete part of dissertation project within Prof. Bouma's lab. I would like to also sincerely thank Brett, my co-advisor, for his dedication and constant support. During my time in his lab, I learnt so much both on technical and scientific levels. I also learnt a great amount on the academic, scientific and industrial worlds as he is always available to share all his experiences. Thanks to both of you! Under your mentoring, I was definitely able to push myself further and achieve much more than I could first envision.

I would also like to acknowledge everyone who directly contributed to the success of this project. Prof. Nicolas Godbout, Wendy-Julie Madore, Étienne de Montigny and Mikael Leduc all contributed to the development of the first injection DCFC. This achievement was an important stepping stone for further developments involved in this project. Thanks to all of you for your time and generosity. I would also like to thank all members of the *Laboratoires des fibres optiques* who contributed to the project over the years. Most recent developments for the injection DCFC were achieved by Castor Optics and, more specifically, Lucas Majeau, who I would like to personally thank for his support and dedication to the project. Several of his prototypes were provided to me, thus greatly benefiting to the progression of the project.

I would also like to thank all LODI members, current or past, for their support and for creating such an enjoyable work environnement : Mathias Strupler, Fouzi Benboujja, Amber Beckley, Xavier Attendu, Thomas Perrillat-Bottonet, Étienne de Montigny and Wendy-Jullie Madore. A special thank to Xavier for his comments on this dissertation as well as to Mathias, who was a great ressource for the development of the DCF optical model. It was a pleasure and privilege to share this experience with all of you.

I would also like to deeply thank my colleague, and foremost best friend, Amélie St-Georges-

Robillard for her incredible support in the course of my graduate studies. She has always been willing to provide me with her assistance whenever, or wherever, I needed it. Her help encompassed personal, technical, scientific, and even administrative levels. From the bottom of my heart, thank you !

I would also like to thank all my colleagues from the Wellman Center for Photomedicine who all contributed to a very rich experience there. I would like first to thank Hyoung Won Baac, Martin Villiger and Néstor Uribe-Patarroyo for their incredible generosity, for all the time spent alongside me to troubleshoot systems, for assisting me with the use of high-power lasers or to explain me the magic world of speckles. A special thanks also to William Lo, Jian Ren and Milen Shishkov who all contributed to different aspects of this project. Thank you also to all group members for all the help I received : Norman Lippok, Sahar Hosseinzadeh Kassani, Chang Su Jun, Wallace Hui, Kenichiro Otsuka, Petra Bodo, and Jacque Namati.

During the course of my graduate studies, I also had the incredible opportunity to work on a project in close collaboration with NinePoint Medical. I would thus like to thank everyone I had the pleasure to interact with ; I learnt so much from this experience. I would especially like to thank Eman Namati, Tsung-Han Tsai, and Joey Jabbour for their generous support and mentoring.

I would also like to acknowledge the financial contributions from different organisms, either in the form of scholarships or travel awards : *Fondation de Polytechnique*, Natural Sciences and Engineering Research Council of Canada (NSERC), *Centre d'optique et photonique du Québec* (COPL), Hydro-Québec, and *Programme Bourses Prestige* offered by Polytechnique's International Relations Office.

This achievement would not have been possible without the tremendous support I received from my family and fiancé. I sincerely thank my love, Laurent Potvin-Trottier, for his unconditional support, for all the times I needed reassurance or someone to rationalize life for me, for his generosity, for all the coffees. You are my rock, my beacon, my light, my everything !

Je tiens également à remercier toute ma famille du fond de mon coeur. Merci à mes parents pour leur support constant et tous leurs encouragements. Ils ont su m'apprendre la valeur de la ténacité, sans laquelle je n'aurais pu me rendre où j'en suis aujourd'hui. Merci à ma soeur, pour ses encouragements quotidiens (aka "Snapchat") lors de la rédaction de cette thèse, et à mon frère pour toujours savoir me faire rire. Merci à vous tous ! !

RÉSUMÉ

L'oesophage de Barrett est une pathologie pré-cancéreuse caractérisée par la présence d'épithélium gastrique au niveau du segment inférieur de l'oesophage. La détection précoce ainsi qu'une surveillance périodique de cette pathologie sont critiques d'autant plus qu'un risque élevé de développer un adénocarcinome oesophagien, une forme cancéreuse avec un taux de survie après 5 ans de 13%, y est associé. Les patients atteints de l'oesophage de Barrett doivent subir une surveillance périodique impliquant la collection d'échantillons de biopsie dans chaque quadrant et à tous les 2 cm le long du segment affecté, une procédure réalisée sous guidage gastroscopique. Étant donné la nature aléatoire et le taux d'échantillonnage faible, cette procédure est typiquement associée avec un taux élevé de résultats faux-négatifs. L'amélioration de l'efficacité ainsi que la diminution des coûts de la surveillance de l'oesophage de Barrett aurait un impact significatif sur la gestion clinique de ces patients.

La tomographie par cohérence optique (*optical coherence tomography* ou OCT) a été proposée pour le guidage de la collection d'échantillons de biopsie afin d'en augmenter le rendement et de réduire le taux de faux-négatif. L'OCT est une technique d'imagerie optique basée sur l'interférométrie à faible cohérence permettant d'obtenir des coupes transversales de tissus biologiques jusqu'à quelques millimètres en profondeur et avec une résolution de l'ordre de 10 μm. L'OCT de l'oesophage est typiquement réalisée à l'aide d'une sonde fibrée en rotation incluse dans un cathéter à ballonet. Afin d'identifier la région d'intérêt pour la biopsie, un laser à haute puissance est utilisé, à travers la même fibre optique, afin de produire une marque superficielle de coagulation visible à la gastroscopie. Cette procédure est appelée le marquage par laser. Ce concept a d'abord été démontré à l'aide d'un laser continu avec une durée d'illumination qui, pour obtenir un marquage avec un contrast sufficient, nécessite l'arrêt de la rotation de la sonde. En plus d'allonger la durée de la procédure, le marquage et l'imagerie ne peuvent pas être faits simultanément. Nous proposons ainsi un système permettant le marquage par laser dynamique, c'est-à-dire que le marquage est réalisé avec la sonde en rotation, simultanément à l'OCT.

L'utilisation d'une puissance crête élevée et de pulses courts pourraient permettre le marquage par laser dynamique en tirant avantage du confinement thermique de l'énergie. Toutefois, lorsqu'une fibre optique monomode est utilisée pour propager un tel laser, la gestion de la puissance devient critique et la dégradation des composants du système a été observée. L'utilisation d'une fibre optique présentant une aire supérieure pour livrer le laser de marquage pourrait réduire la densité de puissance propagée dans le système en plus de réduire

les coûts associés avec la source laser. Ainsi, dans le cadre de cette thèse, nous avons étudié l'impact de l'utilisation de fibre à double gaine (*double-clad fiber* ou DCF) pour la livraison d'un laser de coagulation à haute puissance. Une DCF consiste en une structure concentrique incluant un coeur monomode, une gaine interne multimode (MM), agissant tous deux comme guides d'onde indépendants, ainsi qu'une gaine externe. L'utilisation de DCF permettrait de propager le signal d'imagerie à travers le coeur ainsi que le laser de marquage à travers la gaine interne, et ce, de façon simultanée et co-localisée. Cette thèse est ainsi basée sur l'hypothèse qu'un tel système, contrairement à l'utilisation d'un laser continu monomode, pourrait permettre le marquage par laser dynamique.

Pour vérifier cette hypothèse, un microscope OCT utilisant une DCF a été développé et validé via l'imagerie de tissus ex vivo. Ce système est composé d'un coupleur en fibre à double gaine (DCFC), développé spécifiquement dans le cadre de ce projet, permettant un couplage d'environ 70% d'un laser MM vers la gaine interne de la DCF. Les mécanismes de dégradation de la qualité d'imagerie dus à l'utilisation de la DCF ont également été étudiés et quantifiés. Nous avons ainsi montré que la présence d'images fantôme (due à la propagation du mode fondamental dans la gaine interne) peut affecter la qualité d'imagerie et contribuer à une augmentation du niveau de bruit de 9 dB. Toutefois, en optimisant la longueur des segments fibrés dans le système et en réduisant les réflexions spéculaires, il est possible de réduire considérablement l'impact de ces artéfacts.

Afin de rendre le système de marquage par laser compatible à son utilisation en clinique, une plateforme de modélisation et d'optimization de composants en DCF est présentée. Cette plateforme a été conçue en 1- développant un modèle optique décrivant à la fois les propagations monomode et MM ; 2- en adaptant une modélisation photo-thermique spécifiquement à une illumination MM pulsée.

La modélisation optique du faisceau MM est basée sur une description théorique de la lumière partiellement cohérente qui peut être représentée comme une superposition de mini-faisceaux cohérents. Les propagations monomode et MM prédites par la modélisation ont été validées à l'aide de données expérimentales avec succès. L'optimisation du design optique de la partie distale de la sonde a ainsi été réalisée en utilisant le modèle numérique développé. Différent designs optiques ont été modélisés et analysés à l'aide de cet outils.

La modélisation photo-thermique, quant à elle, a permis l'optimisation des paramètres de coagulation. À l'aide de ce modèle, validé à l'aide d'une étude histologique d'échantillons ex vivo d'oesophages porcins, nous avons montré que le seuil de coagulation par un seul pulse, pour une longueur d'onde de 1436 nm, est de 110 mJ/mm^2 et de 77 mJ/mm^2 pour des conditions ex vivo et in vivo, respectivement. Une analyse multi-paramètres incluant la

taille du faisceau laser, la largeur du pulse, la puissance crête ainsi que la vitesse de rotation de la sonde a été réalisée afin d'obtenir les requis spécifiques menant au marquage par laser dynamique.

Deux modalités supplémentaires, utilisant tous deux un système basé sur la DCF, ont été étudiées dans le cadre de l'imagerie de l'oesophage de Barrett. D'abord, la thérapie par laser guidée par l'image a été étudiée. La thérapie par laser, lorsqu'accompagnée d'un suivi efficace, a le potentiel de traiter localement les cancers épithéliaux tels que l'adénocarcinome oesophagien. L'utilisation d'une DCF permettrait d'effectuer la thérapie par laser ainsi que le suivi par OCT de façon simultanée et co-localisée. Des résultats préliminaires utilisant un laser à fibre dopée thulium injecté via le DCFC, permettant une transmission >400 mW de puissance continue, sont présentée. Le potentiel de ce système pour effectuer le suivi quantitatif de la thérapie par laser est également démontré. La faisabilité de combiner l'OCT et l'imagerie par autofluorescence pour la voie gastro-intestinale a aussi été étudiée. Il a été démontré précédemment que l'auto-fluorescence du collagène, caractérisée par une signature spectrale dans la région du vert, peut être exploitée pour détecter la dysplasie et la néoplasie. Un système basé sur la DCF a ainsi été développé afin de combiner l'OCT et l'excitation par une diode laser bleue. L'auto-fluorescence est collectée par la gaine interne de la DCF et découplée à l'aide d'un DCFC. Les résultats préliminaires de cette étude sont présentés.

En résumé, cette thèse démontre le potentiel de systèmes et composants basés sur la DCF pour le traitement et le diagnostic de l'oesophage de Barrett. Nous avons montré que l'utilisation d'un système basé sur la DCF permet le marquage par laser dynamique et les requis pour une implémentation endoscopique sont présentés. Une plateforme permettant la modélisation et l'optimisation des paramètres optiques et thermiques de la coagulation via une DCF est également présentée. L'utilisation de la DCF ouvre aussi la porte à d'autres modalités prometteuse pour l'oesophage de Barrett telles que l'imagerie par autofluorescence et la thérapie par laser pour lesquelles nous avons montrés des résultats préliminaires encourageants.

ABSTRACT

Barrett's esophagus is a pre-malignant lesion characterized by the presence of gastric epithelium lining the lower esophagus. Early detection and surveillance of this pathology is critical as it is associated with an increased risk for esophageal adenocarcinoma, a form of cancer with a 5-year survival rate of 13%. Barrett's esophagus patients undergo periodic surveillance involving four quadrant biopsies every 2 cm along the Barrett's segment under video endoscopy guidance. However, given the randomness and the low sampling ratio of the biopsy collection, the procedure is typically associated with high rate of false-negative results. Increasing the efficiency and the cost-effectiveness of endoscopic surveillance of Barrett's esophagus would have a significant impact in the clinical managements of these patients.

Optical coherence tomography (OCT) was proposed as a means to guide the biopsy procedure, therefore increasing the biopsy yield and reducing the false-negative rate. OCT is an optical imaging technique using low-coherence interferometry to provide cross-sectional images of tissues to a depth up to a few millimeters with a resolution on the order of 10 μm. OCT imaging of the gastro-intestinal (GI) tract is typically performed through a rotating fiber optic probe within a balloon-catheter. To identify a biopsy's region-of-interest, a higher power laser is propagated through the same fiber optics in order to create a superficial coagulation mark onto the tissue visible under video endoscopy, a procedure called laser marking. Previous implementations used a continuous laser such that, to achieve a coagulation mark with sufficient contrast, the duration of the irradiation required the catheter's rotation to be stopped. In addition to lengthening the procedure time, marking and imaging could not be done simultaneously. We herein propose a system capable of dynamic laser marking (i.e. marking is performed on-the-fly, while the catheter is spinning) for concurrent imaging and marking.

The use of high peak power and short pulses could enable dynamic laser marking, taking advantage of thermal confinement. When used in a single-mode fiber, however, power handling becomes critical and damaging of the diverse components was observed. Using a fiber with a larger area for delivering the marking laser would reduce the power density propagating through the system as well as decreasing the cost associated with the laser source. Herein, we therefore investigate the impact of using a double-clad fiber (DCF) to deliver the coagulating high-power laser. DCF consists in a single-mode (SM) core surrounded by a guiding multimode (MM) inner cladding, both channels acting as independent waveguides, and an outer cladding. DCF could enable simultaneous and concurrent OCT, through the

SM core, and laser marking, using the MM inner cladding to deliver a high-energy pulsed coagulation laser. We hypothesize that this scheme, compared to a continuous, single-mode scheme, would enable dynamic laser marking.

To verify this hypothesis, a benchtop DCF-based system was developed and validated ex vivo. This system includes a novel double-clad fiber coupler (DCFC), a fused fiber coupler allowing a coupling of about 70% of a multimodal laser into the inner cladding of the DCF. Potential OCT image degradation mechanisms due to the use of DCF were also investigated. We showed that crosstalk-induced artifacts could affect the imaging quality and contribute to a noise increase of 9 dB. However, carefully choosing the fiber lengths in the system and reducing specular reflection can greatly reduce the impact of these artifacts.

In order to translate this system into a clinically-compatible endoscopic system, a modeling and optimization platform for DCF devices was introduced. This two-part platform was achieved by 1- developing an optical model describing both the SM and MM propagation behaviours, and 2- tailoring a photo-thermal model to simulate a pulsed MM illumination.

Optical modeling of the MM channel is based on the theoretical description of partially coherence light, which can be represented as a combination of coherent beamlets. Both the SM and MM output beams as simulated by the model were validated using experimental data showing successful prediction of the propagation behaviour for both channels. Optimization of the probe's distal optics is achieved using the developed numerical modeling of the DCF output beams. Different optical designs were analyzed based on this model.

The photo-thermal modeling, on the other hand, allowed the optimization of parameters involved in laser coagulation. The model, which was validated with histological analysis of ex vivo swine esophageal tissue, showed that the radiant exposure threshold to achieve multimode single-pulse marking at 1436 nm is 110 mJ/mm^2 and 77 mJ/mm^2 for ex vivo and in vivo settings, respectively. A multi-parameter analysis including beam spot size, pulse width, peak power and scanning speed was performed to obtain specific requirements in order to achieve visible dynamic laser marking.

Additional impacts of DCF-based systems for Barrett's esophagus are also investigated. First, image-guided laser therapy using a DCF is investigated. Laser therapy, along with proper monitoring, has the potential to locally treat epithelium cancers such as esophageal adenocarcinoma. DCF could allow simultaneous and co-localized OCT monitoring and laser therapy. Preliminary results using a Thulium fiber laser injected through the DCFC, allowing for the delivery of a continuous power of >400 mW, are presented. Potential of the DCF-based system for quantitative laser therapy monitoring is also shown. The feasibility of combining OCT and auto-fluorescence imaging (AFI) for the GI tract is also investigated. It

was previously shown that collagen auto-fluorescence could be used to detect dysplasia and neoplasia. A DCF-based system was developed to combine OCT and blue excitation. Green auto-fluorescence is collected through the large inner cladding and decoupled using a DCFC. Preliminary results are presented.

In summary, this dissertation demonstrates the potential of DCF-based devices and systems for management of Barrett's esophagus. We showed that the use of a DCF-based system enables dynamic laser marking and requirements for an endoscopic implementation are presented. A platform allowing the modeling and optimization of a DCF-based illumination is introduced. DCF-based systems also open the door to other modalities for the diagnosis and treatment of Barrett's esophagus such as AFI or laser therapy and preliminary results for both are shown.

TABLE OF CONTENTS

LIST OF TABLES

LIST OF FIGURES

LIST OF ABBREVIATIONS

AFI	Auto-fluorescence imaging
CCD	Charge coupled device
CDV	Complex differential variance
CNC	Computer numerical control
DCF	Double-clad fiber
DCFC	Double-clad fiber coupler
FAD	Flavine adenine dinucleotide
FD-OCT	Fourier-domain optical coherence tomography
FEM	Finite-element model or modeling
FWHM	Full-width at half maximum
GEJ	Gastro-esophageal junction
GI	Gastro-intestinal
GRIN	Graded-index or Gradient index
HWHM	Half-width at half-maximum
ITR	Inverse tapering ratio
LTT	Laser thermal therapy
MM	Multimode
MMF	Multimode fiber
NA	Numeral aperture
NADH	Reduced nicotinamide adenine dinucleotide
NBTC	Nitroblue tetrazolium chloride
NURD	Nonuniform rotation distortion
OCT	Optical coherence tomography
OFDI	Optical frequency domain imaging
PMT	Photomultiplier tube
PSF	Point spread function
RFL	Raman fiber laser
RJ	Rotary junction
SIM	Specialized intestinal metaplasia
SM	Single-mode
SMF	Single-mode fiber
SNR	Signal-to-noise ratio
TFL	Thulium fiber laser

WD	Working distance
WDM	Wavelength multiplexer

LIST OF APPENDICES

CHAPTER 1 INTRODUCTION

1.1 Clinical problem

Barrett's esophagus is a pre-malignant lesion characterized by the anomalous presence of gastric epithelium lining the lower esophagus. Early detection and surveillance of this pathology is critical since it is associated with an increased risk for esophageal adenocarcinoma, a form of cancer with a 5-year survival rate of 13% [12]. Current standard of care for Barrett's esophagus patients involves periodic endoscopic surveillance along with four quadrant biopsies every 2 cm along the Barrett's segment [13]. Such biopsies are necessary as endoscopy alone is not enough to provide the level of details and depth information for the detection of pre-cancerous and cancerous lesions. However, given the randomness and the low sampling ratio of the biopsy collection procedure, it is typically associated with high rate of false-negative results. There is therefore a great interest in increasing the efficiency and the cost-effectiveness of endoscopic surveillance of Barrett's esophagus as the incidence of esophageal adenocarcinoma has increased by 600% in the last 25 years [14].

In order to improve the efficiency of the surveillance procedure, image-guided biopsy using OCT was proposed [15]. OCT is an optical imaging technique using low-coherence interferometry to provide cross-sectional images of tissues to a depth of a few millimeters and with a resolution of the order of 10 μm [16, 17]. OCT can be used to assess the tissue structure in depth providing information unavailable through standard video endoscopy. Furthermore, OCT was shown to allow identification of esophageal lesions due to Barrett's esophagus and dysplasia [18–21]. Imaging of the gastro-intestinal (GI) tract is typically performed through a rotating balloon-catheter imaging a 6-cm long section in about 2 minutes [4, 22]. Since the biopsy cannot be collected while the OCT balloon-catheter is in place, a high-power laser is used to superficially coagulate the tissue, therefore leaving a mark visible under conventional video endoscopy. The potential of systems combining OCT and laser marking was demonstrated on both a swine model [15] and human patients [23]. A commercial product, offered by NinePoint Medical Inc., was also recently developed. However, all these systems are based on a continuous high-power laser such that, to create a visible mark on the tissue, the catheter's rotation and pullback need to be stopped during the irradiation. Because of this limitation, any movement of the balloon or the esophagus during that interval induces an uncontrolled shift of the laser marking beam on the epithelium, hence producing an elongated mark [23]. In addition to lengthening the procedure time, marking and imaging can not be performed simultaneously such that marking is not assessed in real-time. Therefore, there is a need for

a system capable of dynamic laser marking (i.e. marking is performed on-the-fly, while the catheter is spinning).

1.2 Towards dynamic laser marking

As seen in the previous section, OCT combined with laser marking is promising for the surveillance and diagnosis of Barrett's esophagus. However, early implementations used a continuous high-power laser which comes with a set of limitations. The use of pulsed lasers with high peak power and short pulses could enable dynamic laser marking. If the energy is delivered within the characteristic time of thermal diffusion of the tissue ($\tau <$ few ms), heat conduction is minimal resulting in the thermal confinement and the possibility of using a lower threshold to generate a visible mark.

When used in a single-mode fiber, however, power handling becomes critical and damaging of the diverse components was observed. Using a fiber with a larger area to deliver the marking laser could reduce the power density propagating through the system as well as decreasing the cost associated with the laser source (an expensive single-mode laser source versus a cheaper multimode laser diode). Herein, we therefore investigate the impact of using a double-clad fiber (DCF) to deliver the coagulating high-power laser. A DCF, as shown in Figure 1.1, consists of a single-mode (SM) core, a multimode (MM) inner cladding and an outer cladding. In this fiber, both the SM core and the MM inner cladding acts as independent waveguides. This enables simultaneous and co-localized OCT, through the SM core, and laser marking, using the MM inner cladding, to deliver a high-energy pulsed coagulation laser. We hypothesize that this scheme, compared to a continuous, SM scheme, would enable dynamic laser marking.

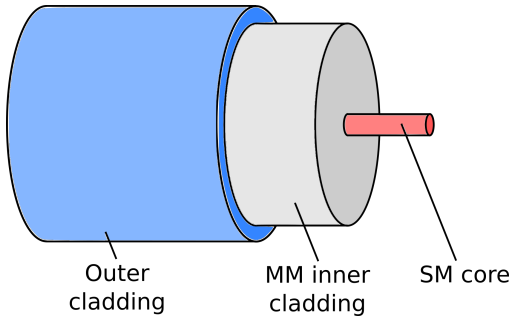

Figure 1.1 Schematic representation of a double-clad fiber.

To verify that hypothesis, a benchtop DCF-based system was developed and validated ex vivo. This system includes a novel double-clad fiber coupler (DCFC) ; a fused fiber coupler that

allows the injection of a multimodal laser into the inner cladding of the DCF. Potential OCT image degradation mechanisms due to the use of DCF were investigated. This dissertation also proposes a DCF-based endoscopic system for dynamic laser marking, compatible with current clinical setting. The design and optimization of such a system is achieved using a photo-thermal model to identify ideal coagulation laser parameters and an optical model allowing the optimization of the distal endoscopic probe optics.

1.3 DCF-based systems : other applications for Barrett's esophagus

1.3.1 Image-guided therapy

A multimodal setup combining OCT and high-power laser delivery, as presented for laser marking, could be extended to image-guided laser therapy. Barrett's esophagus can be treated through mucosal ablative therapies such as radio-frequency ablation, photodynamic therapy, and plasma or laser coagulation, among others. However, most ablative techniques require several treatment sessions over many months and, even after complete eradication, recurrence rates are rather high necessitating continuous surveillance [24]. It has been hypothesized that a limited control over the homogeneity and the depth of the treatment as well as the lack of feedback, therefore resulting in missed buried glands, could explain those limitations [25]. Moreover, due to the complex evolution of Barrett's esophagus, it is still unclear what the optimal treatment strategy is for each stage [26]. A tool allowing for a controlled delivery of energy and providing real-time monitoring of the treatment progression, such as image-guided laser therapy, could therefore have a significant impact on the treatment strategies for Barrett's esophagus. Preliminary results showing image-guided therapy using the DCF-based system developed for dynamic laser marking are included in this work.

1.3.2 Combined OCT and auto-fluorescence imaging

AFI is another promising imaging modality for the detection of early stage esophageal cancer. Dysplasia, neoplasia and inflammation result in changes in fluorescence level of endogenous molecules present in the esophagus, such as collagen and porphyrin (in the case invasive esophageal cancer). The use of AFI was shown to yield increased targeted detection of neoplastic lesions compared to standard video endoscopy, but with high false-positive rate, such that structural imaging was still required [27]. Since DCF-based systems correspond to an ideal setting to combine OCT and AFI [28], a GI compatible DCF system was developed to investigate whether the combination of structural imaging provided by OCT and molecular contrast given by AFI could increase the diagnostic yield of esophageal pathologies. As a

first proof-of-concept, the system was tested on a swine model to study the AFI contrast on healthy tissue.

1.4 Objectives

The goal of this dissertation is to investigate the use of DCF-based system and devices for dynamic laser marking to guide biopsy procedures for Barrett's esophagus and to study its extension to other modalities. In addition to covering the design and development of the hardware involved in such a system (optical probe, DCFC), this dissertation also introduces a modeling and optimization platform for DCF devices which involves photo-thermal simulations for laser coagulation and optical modeling. This dissertation can be divided into the following specific objectives :

1. Design and validation of a DCFC and DCF-based system for concurrent high-power laser marking and OCT
   (a) Development of a dedicated DCFC for high-power light delivery
   (b) Quantitative evaluation of crosstalk-induced ghost artifacts
   (c) Ex vivo validation of concurrent laser marking and OCT
   (d) Development of a clinically-compatible DCF-based system
2. Development of a DCF model for optical design optimization
   (a) Development and validation of an optical numerical DCF model
   (b) Optimization of the esophageal laser marking probe
3. Optimization of high-power laser delivery to achieve single-pulse/dynamic laser marking
   (a) Modeling of photo-thermal processes involved in single-pulse marking
   (b) Optimization of the pulse delivery parameters (i.e. laser- and probe-specific parameters) according to the requirements of current clinical settings
4. Investigation of additional modalities enabled by DCF-based system for esophageal imaging
   (a) Preliminary assessment of DCF-based laser therapy monitoring
   (b) Design of a clinically-compatible system combining OCT and AFI

1.5 Dissertation outline

First, a literature review of the state of the art for OCT-guided laser coagulation and therapy as well as for DCF-based systems and devices is presented in Chapter 2. Chapter 3 includes the article entitled "Laser tissue coagulation and concurrent optical coherence tomography through a double-clad fiber coupler" which describes fulfillment of Obj. 1a-c. Chapter 4 introduces the optical DCF model, developed based on the theoretical description of partially coherent light, and its application to different design options for the esophageal laser marking probe (Obj. 2a-b). Chapter 5 presents the photo-thermal modeling (Obj. 3a) used to optimize the laser- and probe-specific parameters to achieve single-pulse laser marking (Obj. 3b). This Chapter also presents preliminary results of a clinically-compatible DCF-based system for esophageal imaging (Obj. 1d). Chapter 6 presents preliminary results of a DCF-based laser therapy system (Obj. 4a) as well as the progress achieved on the combined OCT-AFI system (Obj. 4b). Finally, this dissertation will conclude on a general discussion (Chapter 7) as well as final recommendations, and future work (Chapter 8). Figure 1.2 provides a schematic overview of the proposed dissertation.

A list of publications, conference proceedings and presentations from the author is presented in Annexe B.

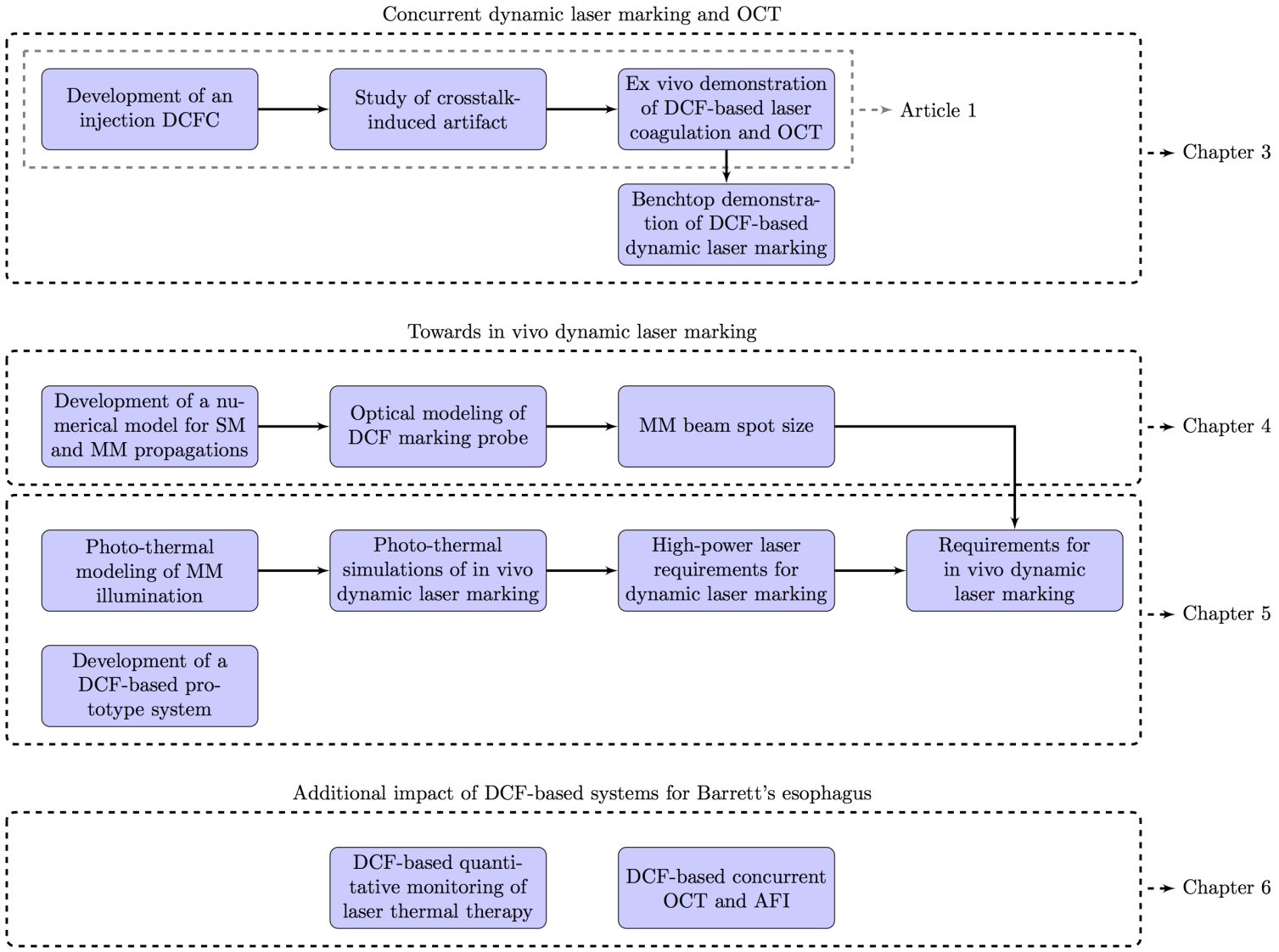

Figure 1.2 Block diagram illustrating the dissertation outline.

CHAPTER 2 LITERATURE REVIEW

This Chapter first introduces the clinical problematic targeted in this dissertation : the surveillance and diagnosis of Barrett's esophagus. An overview of the state of the art for OCT-guided laser coagulation and therapy is also provided. Previous studies investigating the use of auto-fluorescence imaging for esophageal applications are reviewed. Finally, an exhaustive review of DCF-based systems and devices for multi-modality imaging is performed.

2.1 Esophageal pathologies

Organs interact with the outside world through a layer of cells connected to one-another to form an uninterrupted layer, called epithelium [1]. The topmost layer of the skin, the epidermis, is an example of epithelium. Other systems such as the GI tract, airways and arteries all have epithelia of one form or another. The epithelial layer acts as a protective surface against the environment as well as fulfilling absorption and secretion functions. Two types of epithelia are shown in Figure 2.1 : (a) esophageal squamous epithelium, and (b) gastric columnar epithelium. The esophageal squamous epithelium forms the first layer of the esophageal mucosa and presents a stratified structure. The following layer is the lamina propria, formed by connective tissue, the supportive element of the mucosa. The last layer, the muscularis mucosa, contains longitudinal muscle fibers. The esophageal mucosa sits on the submucosa (not shown), a layer of connective tissue and containing mucous glands, as well as the muscularis propria, formed by longitudinal muscle fibers [1]. Figure 2.1b shows a histology section of gastric mucosa presenting a columnar epithelium, the lamina propria and gastric pits.

Epithelial tissues can be affected by a number of abnormalities such as metaplasia, dysplasia, or neoplasia including squamous cell carcinoma and adenocarcinoma [29]. Metaplasia refers to the replacement of one type of cell with another one whereas dysplasia refers to tissues presenting a disorganized growth. Neoplasia is a general term referring to tissues presenting a new growth ; a neoplasm (newly grown tissue), commonly called tumor. Tumors can be benign or malignant. Carcinomas are malignant tumors originating from epithelial tissues. Squamous cell carcinoma denotes a lesion whose cells resemble stratified squamous epithelial cells while adenocarcinoma (as shown in Figure 2.2) refers to the case where neoplastic epithelial cells grow in a glandular pattern.

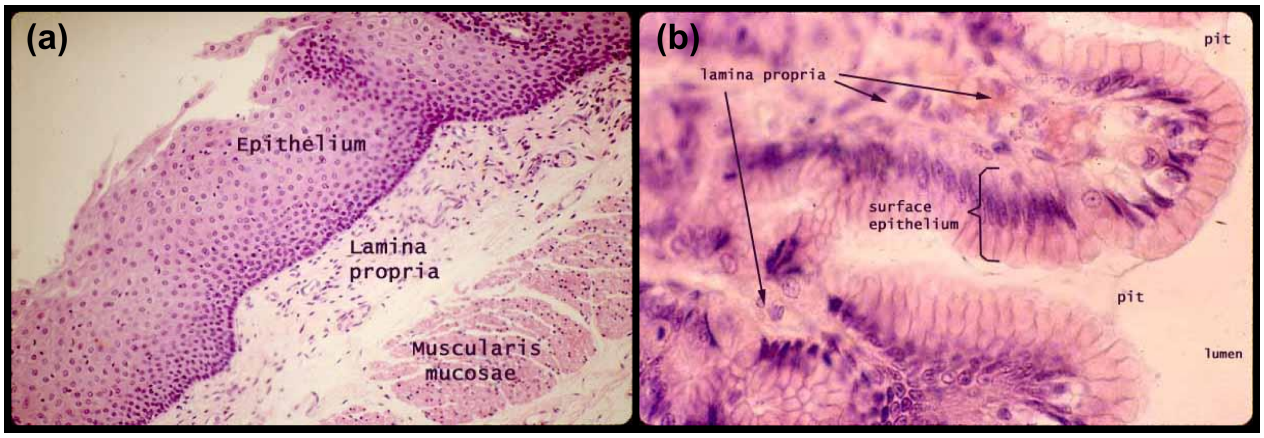

Figure 2.1 Histology sections of (a) esophageal mucosa showing typical layers and (b) gastric mucosal surface showing the columnar epithelium and the gastric pits. Images copyright David G. King, 2017, used with permission [1, 2].

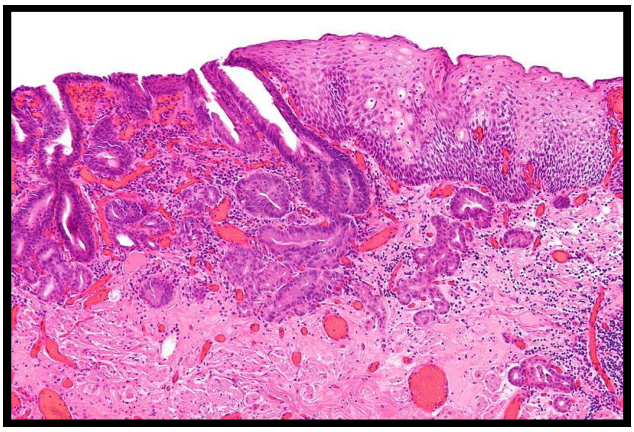

Figure 2.2 Histology section showing, on the right side, normal squamous epithelium and, on the left side, esophageal adenocarcinoma. Image copyright Nephron, distributed under the Creative Commons Attribution-Share Alike 3.0 Unported license [3].

2.1.1 Barrett's esophagus

Barrett's esophagus, named after the thoracic surgeon Norman Barrett who first described this condition, is a type of metaplasia characterized by the presence of gastric epithelium lining the lower section of the esophagus [30]. The current diagnosis of Barrett's esophagus is based on the endoscopic appearance of columnar epithelium in the tubular esophagus as well as the presence of specialized intestinal metaplasia (i.e. epithelium containing metaplastic goblet cells) in biopsy specimen [29]. The prevalence of Barrett's esophagus is about 2-6% in the general population and 15-25% among the elderly population [31]. Barrett's esophagus

can be graded as :

— non-dysplastic
— low-grade dysplasia
— high-grade dysplasia
— esophageal adenocarcinoma.

The current practice for patients with Barrett's esophagus includes periodic endoscopic surveillance to detect high-grade dysplasia and carcinomas, involving four quadrant biopsies every 2 cm along the Barrett's segment [13]. The interval between endoscopy procedures may vary between 3 months and 1 year depending on previous histological findings. The risk to develop cancer is greater for patients presenting high-grade dysplasia such that intervention is usually recommended in those cases [31]. Strategies for intervention include surgical esophagectomy (complete removal of the esophagus), observation with frequent endoscopic surveillance or endoscopic therapy. Endoscopic therapies can refer to either endoscopic mucosal resection or mucosal ablative therapy. The latter case involves the destruction of the dysplastic epithelium allowing its replacement with neoplastic squamous epithelium.

There is a great interest in increasing the efficiency and the cost-effectiveness of endoscopic surveillance of Barrett's esophagus as the incidence of esophageal adenocarcinoma has increased by 600% in the last 25 years [14]. Furthermore, early detection of pre-malignant lesions is critical as the 5-year survival rate of esophageal adenocarcinoma is 13% [12]. Optical imaging is a good candidate for endoscopic imaging of Barrett's esophagus, as it allows for an earlier diagnosis compared to other non-invasive techniques, improves the surveillance procedure through guided biopsy and could potentially improve the outcome of localized treatment through dual-modality systems involving image-guided laser therapy.

2.2 Optical coherence tomography

OCT is an optical imaging technique using low-coherence interferometry to provide cross-sectional images of tissues to a depth of a few millimeters with a resolution of the order of 10 μm [16, 17]. The development of second-generation OCT systems, based on a Fourier-domain acquisition (called optical frequency domain imaging (OFDI) or Fourier-domain optical coherence tomography (FD-OCT)), has significantly increased image acquisition rate and sensitivity [32, 33], thus allowing the clinical implementation of OCT. The use of OCT as an imaging tool to detect and diagnose pre-cancerous and cancerous lesions was demonstrated in different clinical areas, such as gastroenterology [19, 34, 35], pulmonology [36], gynaecology [37] and urology [38].

Several studies have shown the capability of OCT to identify esophageal lesions such as metaplasia and dysplasia [18–21]. Figure 2.3 shows typical OCT images of an irregular gastro-esophageal junction (GEJ) (C-F) along with the corresponding videoendoscopy snapshot (A) and histological slide (B). Figures 2.3C (red arrow) and D show an OCT cross-section with a portion of healthy tissue characterized by a clear contrast between all layers of the mucosa, the submucosa and muscularis propria. In Figures 2.3C (blue arrows) and E, tissue with appearance associated with specialized intestinal metaplasia (SIM) is observed. Specialized intestinal metaplastic tissue typically present in patients with Barrett's esophagus is characterized by a disorganized architecture (irregular mucosal surface and inhomogeneous tissue contrast) and may present glands in the submucosal region [19]. Figure 2.3F shows a longitudinal OCT image of stomach gastric mucosa, distinguishable by the pit and crypt architecture, a segment of SIM, as well as healthy squamous epithelium.

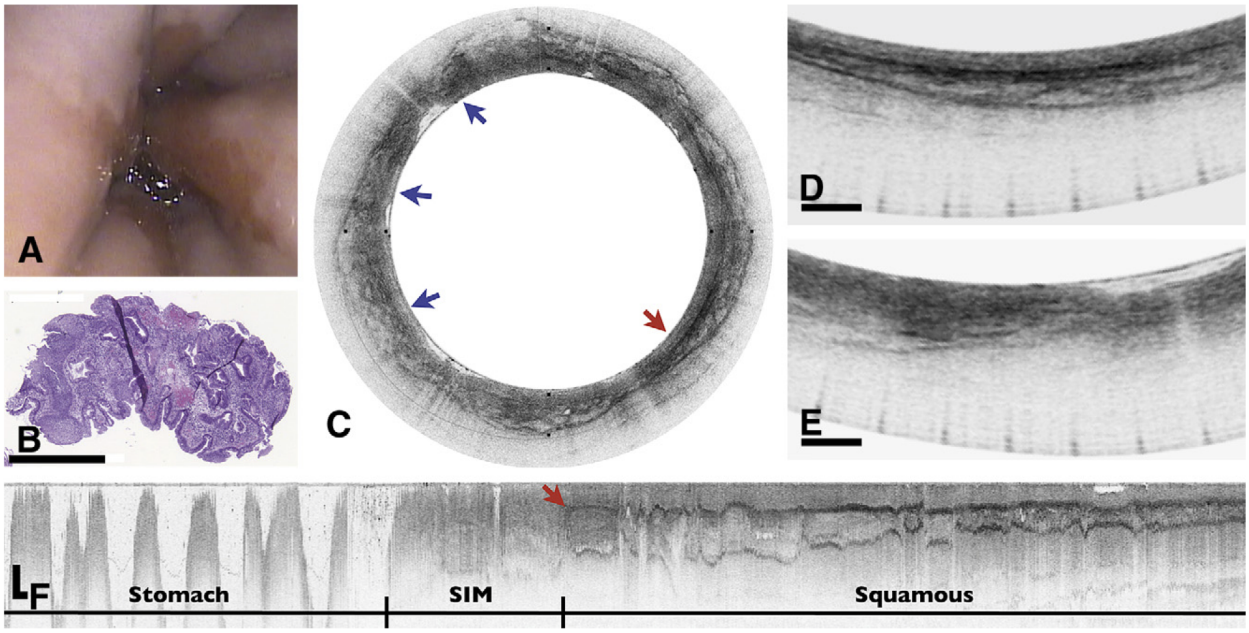

Figure 2.3 In vivo videoendoscopy (A) and OCT images (C-F) with corresponding histological section highlighting SIM (B) of an irregular GEJ. OCT cross-section (C) shows normal layered structure of squamous mucosa (red arrow and inset D) and tissue which appearance is associated with SIM (blue arrows and inset E). Longitudinal view of the GEJ (F) showing stomach, SIM and squamous regions. Reprinted from Ref. 4, copyright 2008, with permission from Elsevier. Scale bars = 1 mm.

OCT also permits distinction between normal tissue, Barrett's esophagus and esophageal adenocarcinoma, the latter presenting the typical structure of the neoplastic epithelium with large pools of mucin and surrounded by cellular stroma (connective tissue cells) [39]. In vivo

studies have also shown the capability of OCT to image the intramucosal vascular network as well as glands and vessels present below the epithelium [4, 22, 39, 40].

Current systems use a fiber optics-based balloon-catheter which, when inflated, maintains the position of the catheter in the center of the esophagus [22]. To acquire the whole area of the inner wall of the esophagus, the catheter is attached to an optical rotary junction (RJ) and a motorized translation stage providing a helical scanning of the laser beam. This system is thus capable of imaging 6-cm long section in about 2 minutes [4, 22].

2.3 Image-guided laser-based coagulation and therapy

Laser-based energy delivery is widely used in the medical field, with applications ranging from laser-based coagulation for marking [23, 41] or therapy [42] using thermal effects to tissue ablation as a surgical tool [43]. These techniques exploit laser-tissue interactions by targeting absorbers present in the tissue such as water, blood or melanin [44]. Figure 2.4a shows the absorption coefficient as a function of wavelength for the main absorbers present in biological tissues. Depending on the application, different types of laser-tissue interactions can be exploited [45] :

1. **Photochemical** Light triggers a chemical reaction within the tissue such as the generation of reactive oxygen species involved in the process underlying photodynamic therapy.
2. **Photothermal** Light is absorbed by the tissue and the energy is released under the form of heat which is then transferred to the bulk tissue. This process is used to induce the coagulation of the tissue.
3. **Photoablative** Non-thermal destruction of material.
4. **Photoplasmic** Light induces an ionizing plasma causing the removal of material.
5. **Photodisruption** Mechanical removal of material based on cavitation and jet-formation effects.

Endoscopic fibered delivery of high-power laser energy presents some challenges such as effective power transmission or fiber coupling. For example, certain laser sources such as high-energy Thulium lasers ($\lambda \sim$1.9 μm) typically requires specialized low-OH optical fiber to limit the absorption of water within the fiber [46]. Absorption by the silica will also degrade the transmission at longer wavelength (see Figure 2.4b).

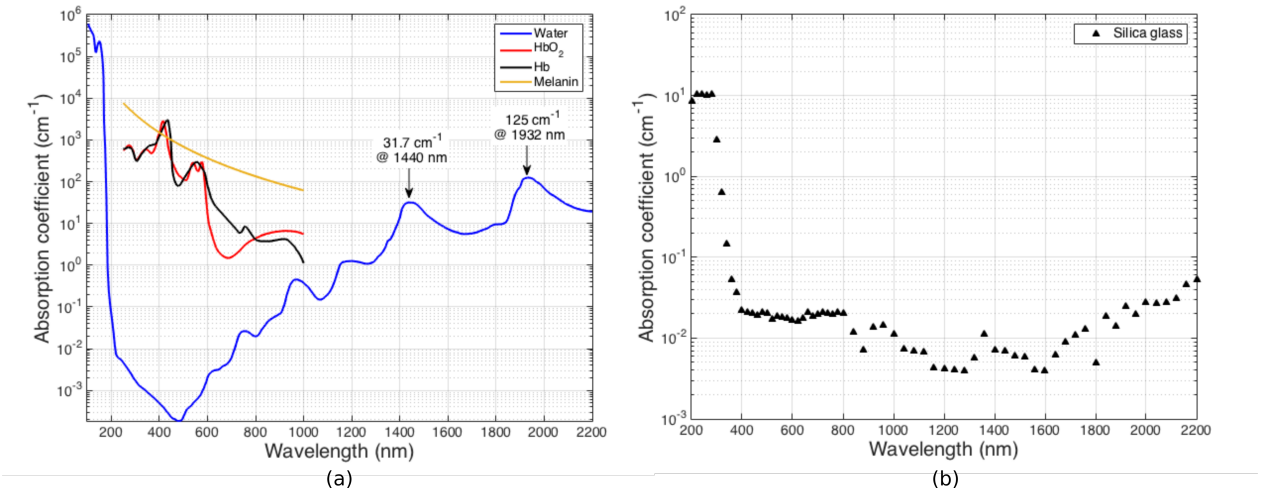

Figure 2.4 (a) Water, oxy- and deoxyhemoglobin (HbO2 and Hb, respectively) as well as melanin absorption curves as a function of wavelength. Data for water from [5] and other absorbers from [6]. (b) Absorption coefficient of silica glass. Data compiled by [7] and available online.

2.3.1 Laser marking for biopsy guidance

As mentioned before, typical endoscopic surveillance involves video endoscopy inspection as well as random four quadrant biopsies every 2 cm along the Barrett's segment. This technique is however sensitive to sampling errors and can lead to false-negative results [47]. In order to improve the effectiveness and efficiency while reducing the costs associated with such surveillance program, researchers have investigated the use of OCT in conjunction with laser marking to guide the biopsy procedure [15, 23]. Using this approach, OCT is used to identify regions of interest on the lower part of the esophagus and a higher power laser is then used to create a superficial mark through tissue coagulation, visible with conventional endoscopy. The region identified is then biopsied for further analysis. This procedure could limit the number of required biopsies as well as reduce the number of false-negative diagnoses.

Studies have investigated laser marking for biopsy guidance either in swine esophagus [15] or in human patients [23]. In both cases, a wavelength close to 1450 nm was chosen since it corresponds to an absorption peak of water (as shown on Figure 2.4) and can be coupled through a standard OCT setup without significant power loss or system modification. Both the imaging signal and the marking laser light were combined into the core of a standard single-mode fiber (SMF) using a wavelength multiplexer (WDM). During the laser marking procedure, the longitudinal pullback and rotation of the catheter had to be stopped, and

the catheter repositioned for each of laser mark. For the swine study, it was calculated that, considering the power and beam spot size, an exposure time of 2 seconds was best to provide enough contrast while limiting permanent damage. Using those parameters, it was shown that the injury was limited to about 27% of the mucosal thickness and significant healing was observed after 2 days. For the human study, two different power levels were tested. For marks induced with a power of 280 mW, only 43% of them were clearly visible with endoscopy while a power of 410 mW yielded increased visibility. Although these laser settings resulted in sufficient contrast, the relatively long exposure times remain an issue. The use of a continuous laser to achieve coagulation leads to a set of limitations. Firstly, any movement of the balloon or the esophagus during that interval induced an uncontrolled shift of the laser marking beam on the epithelium hence producing an elongated mark [23]. Also, a long duration of the laser irradiation required stopping the rotation and pullback of the catheter and repositioning it each time a mark is necessary. In addition to lengthening the procedure time, marking and imaging can not be done simultaneously and, therefore, the marking can not be assessed in real-time.

Numerical models have shown that, by using a laser which pulse duration is shorter than thermal diffusion, a lower energy threshold could be used to induce a visible mark [25, 48]. To demonstrate that concept, Baac et al. have developed an SM Raman fiber laser (RFL) at 1436 nm providing micro- to millisecond pulses with up to 40 W peak power. Using that laser source, they were able to achieve single-pulse marking on swine tissue ex vivo. The use of high-energy, and short pulses could allow dynamic laser marking, that is to say that the marking could be performed while the catheter is spinning and images are acquired and displayed simultaneously. However, considering the required peak power (about 20 W for a 500-μs pulse duration) and the core size of a single-mode fiber (about 9 μm), power handling is critical.

The marking parameters used for each study described above are detailed in Table 2.1.

Table 2.1 Laser marking parameters

Tissue	Wavelength	Beam spot size	Power or Pulse energy	Exposure time	Ref.
Swine	1480 nm	60 μm	380 mW	0.5-10 s	[15]
Human	1450 nm	40 μm	280 & 410 mW	2 s	[23]
Swine	1436 nm	37 μm	$>$ 7 mJ	900 μs	[41]

2.3.2 Laser therapy and ablation

Laser thermal therapy (LTT) has been used as an interventional tool for several applications, including Barrett's esophagus [49, 50]. LTT typically exploits the absorption peaks of water, the main constituent of biological tissues, or the absorption peaks of blood, as presented on Figure 2.4a. For tissue coagulation, absorption peaks in the near-infrared range (1000-1900 nm) are generally targeted as higher cross-section coefficients result in lower laser power requirements, which, in turn, limit damage to adjacent tissues. Moreover, as the same wavelength range is used in telecommunication, fiber components are readily available facilitating the development of endoscopic systems. The therapeutic goal of LTT is to induce coagulation of the targeted tissue in order to induce necrosis or apoptosis and initiate the regeneration of the epithelium [50]. However, used with no guidance and minimal feedback, this technique yielded highly variable results in the past, including frequent recurrence or complications due to the high aggressiveness of the treatment [51]. A DCF-based system could therefore provide a real-time assessment of the depth of the thermal injury, hence preventing unnecessary damage to adjacent tissues, in addition to accurately localizing the pathology margins. Furthermore, it has been shown that wavelength tuning (1860 to 1895 nm) combined with power tuning can be used to control the injury depth offering a range from 150 μm to 1 mm [25]. An effective and ease of use system could even be used, in the case of Barrett's esophagus, to treat patients presenting no dysplasia or low-grade dysplasia like it has been advocated due the significant costs associated with surveillance programs [52].

Thermal effects can be visualized using OCT as the thermal denaturation of protein leads to an increase in scattering properties of tissues (a phenomenon observed for example when cooking egg whites). Additionally, for tissues presenting a high birefringence, the denaturation of collagen can be assessed using polarization-sensitive OCT [53]. The use of OCT to measure dynamic changes occurring during laser coagulation was investigated for diverse tissues using a benchtop system during which changes in optical scattering and tissue morphology were observed [54]. Laser irradiation of the retina was also imaged using OCT where thermal expansion and increased scattering were noted [55]. It has also been shown that OCT can quantitatively assess dynamic tissue response to heat by using a phase-resolved Doppler processing technique or by measuring variations in the magnitude of the complex reflectivity [56]. This study showed that it was possible to outline the boundary of an induced thermal injury in real-time and with high resolution. However, this technique is very sensitive to any phase instability and was shown only for 1-D measurements. A recent study overcame these challenges using complex differential variance (CDV), which exploits phase and intensity fluctuations during thermal therapy without the need of a phase-stable OCT system [57].

Using this technique, the thermal coagulation boundary created by a Thulium fiber laser (TFL) (1860-1895 nm) was successfully delineated on retinal, esophageal and skin tissues.

Several studies investigated the use OCT to monitor laser and radio-frequency ablation. It has been used to dynamically monitor laser ablation (crater size and depth) [58, 59] and assess wound closure longitudinally [60]. OCT was also used to assess the response of radio-frequency ablation treatment for Barrett's esophagus [61, 62]. Mucosal thickness and residual glands imaged with OCT right after the ablation were found to be prediction markers for the presence of Barrett's esophagus at follow-up visits and could be used to make on-the-spot retreatment decisions [61]. However, the imaging was not performed simultaneously to the treatment meaning that no active control of the ablation laser power was done. This result nevertheless emphasizes the need for a high-resolution real-time monitoring of any endoscopic therapeutic technique.

Few studies involved an endoscopic system combining both imaging guidance and laser therapy. Either a benchtop system was used to combine different modalities [57, 59] or different probes were used, which complexified the procedure [63]. Li et al. recently presented a dual channel probe allowing co-registered and simultaneous OCT and laser ablation [64]. In this case, they used a 6.1-μm laser source such that a hollow-core waveguide was required to deliver the laser light to the sample. This waveguide was juxtaposed to a scanning fiber OCT imager. To ensure co-registration of both modalities, an angled-polished CaF2 window was used at the tip of the hollow-core waveguide, therefore requiring careful alignment and calibration.

2.4 Auto-fluorescence imaging

AFI contrast comes from the absorption of illumination photons and re-emission of photons of lower energy (i.e. longer wavelength) by fluorophores present in a tissue. Each molecule is characterized by an absorption and emission peaks providing a molecular contrast. In the esophagus, the main fluorophores are collagen (most prominent fluorophore of the GI tract), mitochondrial reduced nicotinamide adenine dinucleotide (NADH) and flavine adenine dinucleotide (FAD) present in epithelial cells, as well as porphyrin (present in invasive esophageal cancer) [65]. Table 2.2 shows excitation and emission bands for each fluorophore. Dysplasia in the esophagus is associated with an increase of the fluorescence level produced by mitochondrial NADH and FAD [65], but will actually be accompanied by a decrease of the stromal fluorescence (i.e. fluorescence from the submucosal collagen content). This decrease can come from the fact that the submucosal fluorescence level is affected by light attenuation by superficial layers (i.e. mucosal thickness or hemoglobin content variations) [66]. Neoplasia

and inflammation could also cause a decrease of stromal fluorescence [65].

Table 2.2 Main fluorophores present in the esophagus

Fluorophore	Excitation band	Emission band	Ref.
NADH	330-370 nm	380-550 nm	[67]
FAD	∼350-500 nm	∼500-600 nm	[68]
Submucosal collagen content	∼400-500 nm	∼500-600 nm	[69]
Porphyrin	∼400 nm	∼630-750 nm	[70]

Several studies have investigated the use of AFI as a diagnostic tool for esophageal pathologies. Holz et al. used auto-fluorescence spectroscopy at different illumination wavelengths (369, 395, 405, 410 & 416 nm). Their fibered probe consisted in 15 illumination and 15 collection fibers. To discriminate between intestinal metaplasia and high-grade dysplasia/esophageal adenocarcinoma, they used the ratio between fluorescence intensities at 495 nm (i.e. collagen fluorescence) and 640 nm with a single-wavelength illumination (395 nm) resulting in a sensitivity of 80.0% and a specificity of 89.5%. Illumination at 405 and 410 nm also resulted in similar sensitivity and specificity.

The use of a tri-modality endoscopic system was also investigated to detect early-stage neoplasia [27]. Their wide-field system includes high-resolution white light endoscopy, AFI and narrow band imaging (NBI - a modality that enhances the visibility of superficial mucosal structures using optical filters). AFI is performed using a blue excitation (390-470 nm) and a detection band between 500 and 630 nm. To identify lesions, they used a composite image formed by the auto-fluorescence signal and green reflectance signal. With this study, involving 87 patients, the authors demonstrated that the use of AFI results in a significant improvement of high-grade dysplasia and carcinoma detection compared to standard video endoscopy. Inspection of lesions under NBI is still necessary to reduce the false-positive rate of combined high-resolution endoscopy and AFI. Despite that, it was still shown that targeted biopsy using the trimodal system was inferior to random biopsy. A subsequent study hypothesized that the auto-fluorescence signal was sensitive to the mucosal thickness, which implies that the signal could be altered by non-dysplastic changes such as tissue inflammation [72]. To mitigate that issue, they used two narrow excitation bands (380-390 & 400-420 nm) and refined the algorithm producing the pseudo-color composite image. While they still showed that AFI increases the targeted detection of neoplastic lesions, their new-generation system presented only limited gain over its predecessor.

Although AFI provides an additional contrast mechanism, it seems like structural imaging, such as OCT, is still required to improve specificity and provide context to the signal origin. Combined OCT and AFI systems were previously developed for other pathologies, such as

pulmonary cancer. Pahlevaninezhad et al. investigated the use of AFI to detect neoplastic lesions in lung cancer using a 445-nm laser source combined with an OCT system in a benchtop system, showing strong auto-fluorescence signal coming from cartilage and dense connective tissue. In vivo results were obtained using an endoscopic system and resulted in similar observations [74] as well as evidence showing the identification of small pulmonary vasculature [28].

2.5 Double-clad fiber systems and devices

DCFs were first developed to pump high-power fiber lasers [75] and have been used in imaging systems in the last decade for a multitude of applications and modalities. Typically, the core of the DCF is used to deliver illumination light and the inner cladding, for collecting the back-scattered or emitted signal. For endoscopy, the larger area of the inner cladding allows an increased signal collection efficiency and reduced speckle noise when compared to a single-mode collection [76, 77]. DCFs were also used in multimodal imaging in which, for instance, the inner cladding is used to collect fluorescence, linear as well as non-linear, or spectroscopic signal [10, 28, 78–81]. Furthermore, DCFs present a clear advantage for multimodal imaging compare to multi-fibers setup [82] as they allow a more compact and robust probe tip as well as the intrinsic co-registration of different modalities. Another type of double-clad fibers, double-clad photonic crystal fibers, were used for endoscopic nonlinear imaging using the core to efficiently deliver excitation pulses and the inner cladding for collection [83–85]. In the presented project, the core of the DCF would be used to deliver and collect OCT signal while the inner cladding would be used to deliver higher-power laser light. Using the larger area of the inner cladding would decrease the power density propagating through the system.

When using a DCF for coherent imaging such as OCT, special care as to be taken to avoid crosstalk between the core and the inner cladding which could lead to the presence of ghost images or the broadening of the point spread function (PSF). If light traveling in the inner cladding couples into the single-mode core and reaches the interferometer, it would create additional interferometric signals but at different frequencies as the traveled path lengths would be different. Indeed, each mode traveling in the inner cladding sees a different effective refractive index. As the number of modes is generally rather large, the ghost images could completely overwhelm the signal of interest and, therefore, decrease significantly the imaging quality. This effect was studied for fiber-bundle [86, 87] and large-core fiber [88]. However, no quantitative assessment was performed in the case of DCF.

In order to couple (or decouple) the signals traveling into the core and the inner cladding, either a free space or fibered scheme can be used. For free space combiners, beam splitters

or dichroic mirrors are typically used. For systems involving a rotational catheter, the combiner can be included in the rotary junction. Such systems will be reviewed in Section 2.5.1. Section 2.5.2 will review the fibered couplers-based systems.

2.5.1 Rotary junction

To allow circumferential imaging of an organ's inner wall, such as for GI imaging, a motorized rotational device is required. Typically, the rotation is performed either using an optical RJ that will allow for the rotation of the catheter [79, 82] or using a micromotor at the distal end of the catheter to induce a rotation of the laser beam [80, 89]. The optical RJ allows the transmission of the laser light between a fixed fiber and a mobile fiber through a free space portion. This system allows a more compact, robust and less expensive catheter, as the motor is external to the endoscope. However, the free space portion within the RJ could induce crosstalk between both channels of the DCF and, therefore, the RJ has to be extremely well aligned. The advantage of using a micromotor resides in the fact that there is no crosstalk induced, but the size of the catheter, which includes the motor, is currently limited to 2-3 mm [80, 89].

Different designs of DCF-based optical RJ have been proposed. The simplest design that has been suggested used a gradient index (GRIN) lens to collimate the output beam of the DCF for free space propagation towards a second GRIN-DCF assembly [82]. GRIN lenses lengths and their relative positions were determined experimentally to optimize the core-to-core transmission of the OCT signal. Such RJ are also commercially available (Princetel Inc.). The collimator-based design is however not suited for multimodal system involving wavelength bands that are far on the spectral range (visible and near-infrared bands, for instance). Another design, also commercially available, is based on butt-coupled fibers with index-matching fluid at the interface [90, 91]. The design offers better chromatic performances, but will be more sensitive to crosstalk and could have a limited rotational speed. Kim et al. have investigated different lubricant fluids and their respective fluorescence background level when using an UV illumination (365 nm). They found that immersion oil presents a low fluorescence background compared to typical index-matching fluid. However, interaction between the immersion oil and the UV illumination caused significant damage to the fiber end facet. These results emphasize the fact that butt-coupled fibers-based RJ might not be suitable for high-power applications as well as UV-based imaging.

Dual-modality three-port RJs, based on a dichroic mirror and collimators, and also acting as combiners, were also suggested for combined OCT and near-infrared fluorescence [79, 92] as well as combined OCT and AFI [74]. In this design, the OCT signal is transmitted from

a SMF (Port 1) to the core of the DCF (Port 2) through the dichroic mirror, whereas an excitation beam (Port 3) is reflected by the mirror and coupled into the inner cladding or the core of the DCF (Port 2). On return, both modalities are de-multiplexed by the same dichroic mirror. An additional dichroic mirror can also be added at Port 3 to further decouple the excitation signal from the emission signal for fluorescence systems. Different studies reported different performances with core-to-core insertion losses ranging from 0.5 to 1.2 dB and MM coupling, from 2 to >6 dB, which suggests that careful alignment of the three-port device is critical. Moreover, the presence of the dichroic mirror results in a greater distance between the collimators at different ports, which can limit the coupling efficiency and increase the sensitivity of the design to misalignment.

Table 2.3 summarizes performances for all designs.

Table 2.3 DCF-based RJ performances

Design	SM insertion loss	MM insertion loss	Best for	Ref.
GRIN lenses	0.6 dB	3 dB	High-power applications, OCT + infrared spectroscopy	[82]
Index-matching fluid	< 0.4 dB	< 0.4 dB	OCT + fluorescence imaging	[90, 91]
Dichroic mirror	0.5 dB	2 dB (exc.) and 0.8 dB (em.)	OCT + fluorescence imaging, UV illumination-based fluorescence	[74]

2.5.2 Double-clad fiber couplers

To improve signal collection and replace free space bulk optics (beam splitters or dichroic mirrors) typically required for de-multiplexing different signals, DCFCs have been developed. Different techniques, showing different performances, have been reported for couplers aiming at extracting light from the inner cladding of the DCF as presented in Table 2.4. First DCFCs were based on a symmetric design made using two identical fibers, therefore limiting the coupling ratio to a theoretical limit of 50%. Best performances were obtained by Lemire-Renaud et al. using a fusion-tapering method achieving a MM coupling between 40 and 46% and a core transmission of >95%.

A study showed the potential of asymmetric devices for which fibers presenting different optical etendues, in this case a DCF and a higher-etendue multimode fiber (MMF), were fused together and tapered down [9]. The optical etendue G is expressed as :

$$G = \pi S \mathrm{NA}^2, \tag{2.1}$$

where S corresponds to the total mode area and the numerical aperture for fiber optics is defined as $\mathrm{NA} = n \sin \alpha$. Figure 2.5a shows a typical asymmetric coupler extracting light from the DCF (Port 2) to the MMF (Port 3). The power transmission between Ports 2 and 3 can be predicted, neglecting excess loss, by :

$$T_{2-3} = \frac{1}{1 + \frac{G_1}{G_3}}. \tag{2.2}$$

Therefore, carefully choosing fibers to obtain an optical etendue ratio above one would result in a multimode coupling efficiency greater than 50%. Figure 2.5b shows the theoretical curve obtained from Equation 2.2 along with experimental points. An etendue ratio as high as ∼15 was used, providing a transmission of more than 90% [10]. De Montigny et al. pushed the concept even further introducing a double asymmetry. The first asymmetry resides in the transverse cross-sections by using fibers with different optical etendues as demonstrated in the previous study. The second asymmetry comes from the asymmetrical fusion of the fibers, where the transition section of the DCF is fused to the constant section of the higher-etendue MMF. Those couplers were however all designed to extract light from the inner cladding. Herein, we wish to combine or inject multimode light within the inner cladding (i.e. from Port 3 to Port 2), which requires an etendue ratio below one as indicated by the shaded area in Figure 2.5b.

Table 2.4 Double-clad fiber couplers for light extraction

Type	Technique	MM coupling efficiency	Ref.
Symmetric	Side-polishing method	15% @ 750 nm	[94]
	Twisting method	30% @ 750 nm	[78]
	Twisting method	32% @ 1230-1330 nm	[82]
	Fusion-tapering method	40-46% @ 1265-1325 nm	[8]
Asymmetric	Fusion-tapering method	> 70% @ 1265-1325 nm & 400-1000 nm	[9]
	Fusion-tapering method	>90% @ 750-900 nm	[10]
	Fusion-tapering method + double asymmetry	>70% @ 600-800 nm	[93]

Originally, pump combiners were used to inject light within the inner cladding of a DCF to pump fiber lasers [95] and were, more recently, used in imaging setups [89, 96]. Such devices are based on fused fiber bundle (N multimode fibers with a probe fiber in its center) spliced

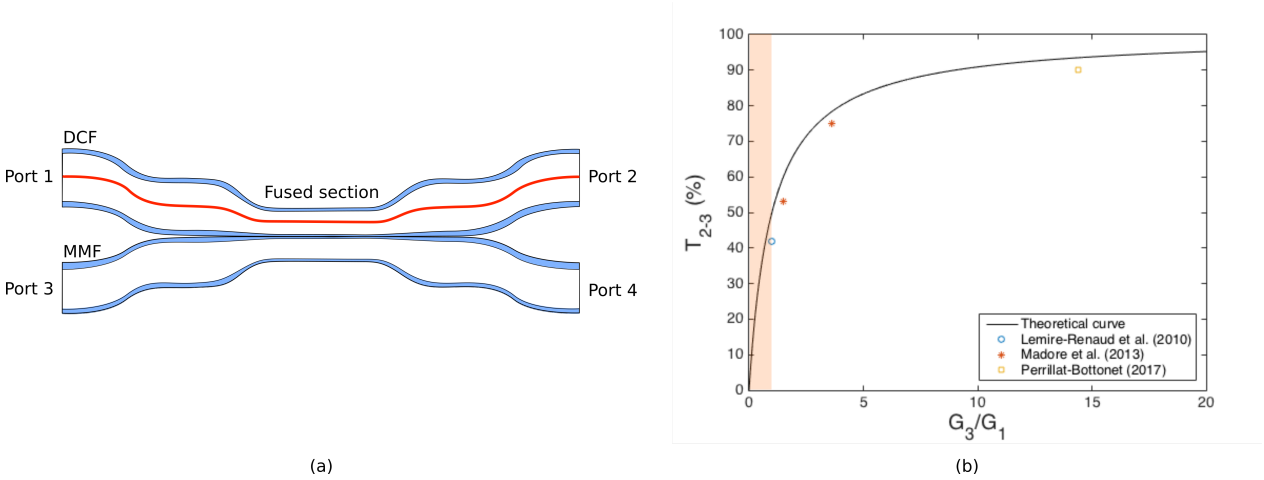

Figure 2.5 (a) Schematic of an asymmetric DCFC based on a DCF fused with a MMF. (b) Theoretical transmission as a function of fiber's etendue ratio along with experimental points taken from Refs. 8–10. The shaded area shows the targeted etendue regime for an injection DCFC. Adapted from [9].

to the output DCF. Typically, coupling efficiencies from the fused fiber bundle to the output fiber can go up to 95%. DCFCs, compared to pump combiners, present the advantage of being more versatile in the context of multimodal imaging as several DCFCs can be combined and arranged serially to combine and extract different signals with varying wavelengths. As the pump combiner design is based on a splice, it will inherently induce ghosts from back reflections. Moreover, a high-numerical aperture (NA) inner cladding is typically used in such combiners, which limits its use for biological imaging since it is highly sensitive to bending losses and complicates the distal optics design.

2.5.3 DCF catheters

Several strategies to built a DCF-based catheter were investigated over the years. Typical GRIN lens-based design [22] can be readily used with DCF. These probes typically involve a glass rod or spacer to expand the beam, a GRIN lens and a prism to deflect the beam at 90°. A GRIN lens-based design can also be used along with a distal micro-motor to which a prism [89] or a mirror [80] is attached. For non-linear DCF based systems, miniature objectives are typically used [97, 98].

Monolithic fibered designs were also investigated and consist in an attractive option due to their compactness. Ball lens catheters, made by heating a piece of no-core fiber fused to the imaging fiber and first developed for cardiovascular imaging [99], were used with DCF for

combined OCT and fluorescence spectroscopy [78] or near-infrared fluorescence imaging [79]. Ball lenses can be polished to accommodate side-looking probes. Lorenser et al. developed a needle probe also based on a monolithic fused design consisting of a no-core fiber and a GRIN fiber as well as a 45° mirror which can be mounted inside a 23-gauge needle (outer diameter of 640 μm). Pahlevaninezhad et al. presented a similar design for a 900-μm DCF catheter based on segments of MMF, GRIN fiber as well as a polished piece of no-core fiber for 90° beam reflection. The first segment of MMF acts as a beam expander for the SM signal to increase the NA of the OCT beam while maintaining the same guiding properties for the MM signal. Such monolithic fibered designs are however typically limited to short working distance designs.

Independently of the design, there is however no convenient DCF model to design and optimize distal optics for both the SM and MM channels. Also, for fluorescence systems, since the excitation and collection PSFs are decoupled when using DCF, it is unclear what the probed volume really is. Therefore, there is a need for a design platform allowing the analysis of the SM and MM beams going through a certain optical design.

CHAPTER 3 ARTICLE 1 : LASER TISSUE COAGULATION AND CONCURRENT OPTICAL COHERENCE TOMOGRAPHY THROUGH A DOUBLE-CLAD FIBER COUPLER

This article presents the first demonstration of an injection DCFC enabling concurrent OCT and laser coagulation systems. Design, fabrication and characterization of such coupler is herein described. A DCF-based benchtop system is used along with the DCFC to : 1- quantitatively assess the impact on imaging sensitivity and 2- perform concurrent OCT and laser coagulation on swine esophageal tissue. It is further shown that the DCF-based system allows for the real-time visualization of dynamic changes in signal attenuation. Section 3.5 presents ex vivo dynamic laser marking results, obtained with the experimental setup introduced in this article, that were not included in the manuscript. These results demonstrate the capability of the DCF-based benchtop system to achieve dynamic laser marking.

The article was submitted to the journal Biomedical Optics Express on January 16, 2015 and was accepted on March 16, 2015. The principal author (Kathy Beaudette) contributed to $\sim$70% of the work and was involved in all aspects. Specifically, her contribution includes the realization of the literature research, the design and fabrication of the coupler, the design and execution of coagulation and sensitivity experiments, the data analysis, as well as the redaction of the manuscript. Dr. Hyoung Won Baac contributed to the design and execution of the coagulation experiments, the data analysis and the redaction. Dr. Wendy-Julie Madore contributed to the design of the coupler, the sensitivity analysis and the redaction. Dr. Martin Villiger contributed to the design of the coagulation and sensitivity experiments, the results analysis, the redaction and provided assistance with the imaging setup. Prof. Nicolas Godbout contributed to the design of the coupler as well as the sensitivity analysis. Profs. Brett E. Bouma and Caroline Boudoux are the principal investigators on this project, provided assistance in the design of the coupler and experiments and contributed to the redaction and results analysis.

Authors : Kathy Beaudette, Hyoung Won Baac, Wendy-Julie Madore, Martin Villiger, Nicolas Godbout, Brett E. Bouma, and Caroline Boudoux

Article published : Biomedical Optics Express, 6(4), 1293-1303 (2015).

Abstract : Double-clad fiber (DCF) is herein used in conjunction with a double-clad fiber coupler (DCFC) to enable simultaneous and co-registered optical coherence tomography (OCT) and laser tissue coagulation. The DCF allows a single channel fiber-optic probe to be shared : i.e. the core propagating the OCT signal while the inner cladding delivers the coagulation laser light. We herein present a novel DCFC designed and built to combine both signals within a DCF (>90% of single-mode transmission ; >65% multimode coupling). Potential OCT imaging degradation mechanisms are also investigated and solutions to mitigate them are presented. The combined DCFC-based system was used to induce coagulation of an ex vivo swine esophagus allowing a real-time assessment of thermal dynamic processes. We therefore demonstrate a DCFC-based system combining OCT imaging with laser coagulation through a single fiber, thus enabling both modalities to be performed simultaneously and in a co-registered manner. Such a system enables endoscopic image-guided laser marking of superficial epithelial tissues or laser thermal therapy of epithelial lesions in pathologies such as Barrett's esophagus.

OCIS codes : (060.2340) Fiber optics components ; (170.2150) Endoscopic imaging ; (170.3880) Medical and biological imaging ; (170.3890) Medical optics instrumentation ; (170.4500) Optical coherence tomography.

3.1 Introduction

Optical coherence tomography (OCT) [16] is currently investigated as an aid to guide biopsy for the diagnosis and surveillance of Barrett's esophagus, a pre-malignant lesion that bears an increased risk of progressing to esophageal adenocarcinoma [15, 23]. Image-guided biopsy shows great potential to reduce false-negatives and increase the overall efficiency of the procedure as opposed to performing randomized biopsy sampling, the current surveillance strategy [23]. Imaging of the esophagus is done through an inflated balloon-catheter, which maintains distal optics in the center of the lumen. An optical rotary junction is used to acquire circumferential images of the inner wall of the esophagus, along with a motorized translation stage providing a helical scanning of the laser beam over a 6-cm long segment in about 2 minutes [4, 22]. A second higher power laser source is used to perform laser tissue coagulation leaving on the epithelium marks, that are visible with conventional white light endoscopy [23]. These marks are then used to guide sample collection under endoscopic visualization. Previous coa-

gulation lasers were coupled directly to single-mode fiber (SMF) based OCT systems through wavelength division multiplexers, thus requiring minimal modification to the imaging system. Laser coagulation for tissue marking was demonstrated in vivo using a continuous-wave laser source with 410 mW output power at a wavelength of 1450 nm during 2 s [23]. A pulsed Raman fiber laser was also used to demonstrate single-pulse marking using 900-μs pulses at a wavelength of 1436 nm with pulse energies greater than 7 mJ [41], taking an advantage of the temporal confinement of the thermal energy delivery to achieve higher temperature in a shorter time in the optical zone [100]. However, the first configuration required stopping the probe's rotation to provide continuous irradiation over a few seconds, preventing real-time monitoring of the coagulation process. A pulsed laser source could therefore allow for a more efficient procedure, but the single-mode delivery previously demonstrated required a rather expensive and cumbersome laser source, not commercially available, which, additionally, lead to power densities in the fiber core very close to or higher than the damage threshold of many elements within the balloon-catheter and the rotary junction.

We herein investigate the use of a double-clad fiber (DCF) based system combining OCT – through the single-mode core – and laser tissue coagulation – through the multimode inner cladding – simultaneously and in a co-localized manner. Such a system would allow the use of a less expensive multimode marking laser, an increased mark visibility through a larger beam spot size as well as lower power density travelling through the catheter. Furthermore, the use of DCF presents a clear advantage for multimodality optical systems, compared to multi-fiber setups [82], as it allows for a more compact and robust probe tip as well as the intrinsic co-registration of different modalities. Such a system could additionally be extended to monitor dynamic processes during laser therapy allowing an increased control over the energy deposition and treatment depth [22, 54, 55, 101].

The use of DCFs was previously demonstrated for endoscopy [76, 102] and multimodal imaging combining OCT through the core and using the inner cladding to collect fluorescence or spectroscopic signal in, for instance, [74, 78–81, 89]. Furthermore, double-clad fiber couplers (DCFCs) have been demonstrated to efficiently extract inner cladding light out of the DCF [8, 103]. To optimize extraction ratio, our group introduced an asymmetric design, exploiting waveguides presenting uneven optical etendue. This design provides a multimode coupling ratio of >70% while preserving the core signal ($\geq$ 95%) [9]. Such DCFCs were however optimized for light extraction from the inner cladding and are, therefore, not suitable for the present application, which requires injection of light into the DCF's inner cladding. In this paper, we report the use of DCF and a dedicated DCFC enabling simultaneous and co-localized OCT and laser tissue coagulation. The fabrication and characterization of this novel DCFC optimized for simultaneous OCT imaging and multimode light injection are

presented. We also quantitatively assess potential OCT image degradation mechanisms due to crosstalk between both channels of the DCF at junction sites and propose strategies for their minimization. Finally, we demonstrate the potential of this combined system for image-guided laser tissue coagulation by acquiring OCT images simultaneously to laser irradiation on ex vivo biological tissue.

3.2 Materials and methods

3.2.1 Double-clad fiber coupler

Figure 3.1 shows the DCFC designed to deliver coagulation laser energy to the OCT imaging site. This design is inspired from a theoretical description of DCFCs introduced by Madore et al. [9], which showed that power distribution between ports of the coupler is proportional to the ratio of fiber's etendues. The etendue, G, of a fiber is given by :

$$G = \pi S(\mathrm{NA})^2 \tag{3.1}$$

where S is the mode field area and NA is the fiber's numerical aperture. Previously demonstrated couplers were intended for extraction, i.e. the transfer of light from the DCF inner cladding into a larger multimode fiber. For this application, however, injection into the DCF is required such that the ratio of etendues must therefore be inversed. The injection fiber was thus chosen for its small etendue, which, according to Eq. 3.1, is achieved either by a very low NA, a small area or a combination of both. The fabrication technique was further amended by pre-tapering the multimode fiber, therefore allowing multimode expulsion for easier transfer into the DCF's inner cladding, and by using an asymmetrical fusion geometry resulting in a doubly asymmetrical DCFC, as described in [93].

The proof-of-principle prototype of such a DCFC was fabricated using a commercial DCF (Nufern, SM-9/105/125-20A) for the imaging fiber as it matches the standard SMF used in our OCT system in core and outer cladding dimensions as well as core numerical aperture. A small inner cladding DCF (core, inner cladding and outer cladding diameters of 4.1 :25.8 :125 μm, respectively) was used as the injection fiber for its multimodal inner cladding, neglecting the core, which does not guide light at long wavelengths. These particular fibers were used as the refractive index of the outer cladding of the injection fiber (which acts as the multimode waveguide in the tapered section) matches that of the inner cladding of the imaging DCF, therefore enabling coupling between these two regions. A custom-built fusion-tapering setup using a micro-torch was used to fabricate the coupler [104]. The injec-

tion fiber was first tapered down to an inverse tapering ratio (ITR) of 0.13 such that, in the constant section, most light escapes the multimode inner cladding and leaks into the outer cladding. To further maximize multimode transmission from the injection fiber to the inner cladding of the imaging DCF, the outer cladding of the imaging fiber was removed over a 30-mm section by hydrofluoric acid etching, as described in [9]. Both fibers were then placed side-by-side, the transition section of the injection fiber facing the etched region of the imaging fiber (illustrated in Fig. 3.1(a) – dashed box) and maintained with a geometry favoring maximum contact during the fusion. The fusion step was stopped when losses in single-mode transmission reached a maximum value of 0.5 dB.

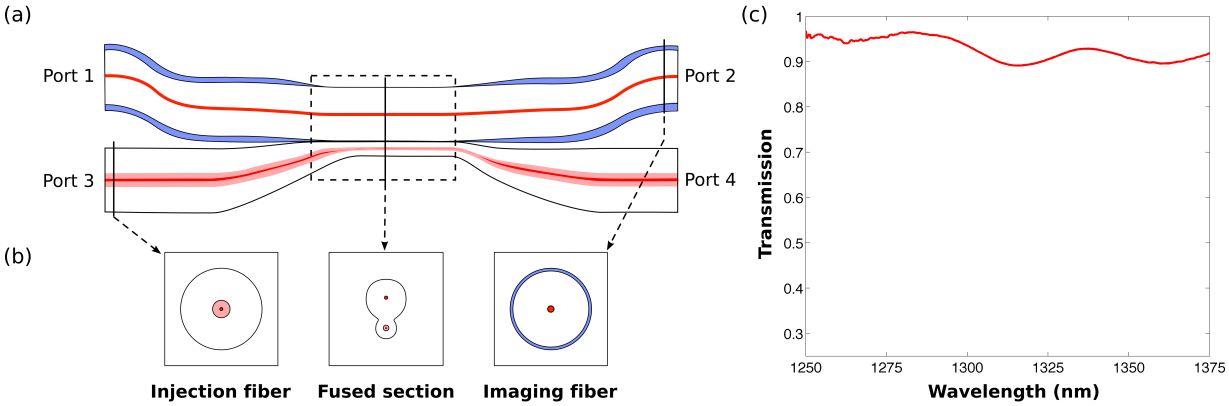

Figure 3.1 (a) Schematic diagram of the DCFC achieved by asymmetrically fusing the imaging fiber (top) to the transition segment of the injection fiber (bottom). The dashed box represents the section along which the fibers were fused. (b) Schematic diagram of cross-sections of, from left to right, the injection fiber, the fused section and the imaging fiber. (c) Single-mode transmission spectrum (smoothed using a moving average filter) of the core signal from Port 1 to Port 2.

Single-mode transmission was characterized over the wavelength range of our OCT system (∼1260–1375 nm) while multimode coupling was measured at 1436 nm, corresponding to the operating wavelength of our coagulation laser. Single-mode transmission was monitored in-line during the fabrication process by injecting a broadband source (Hewlett-Packard, Broadband Light Source, 83437A, 1200–1650 nm) into the DCF core at Port 1 and detected with an optical spectrum analyzer (ANDO Electric, AQ6317). To ensure that only single-mode light was collected, a SMF was spliced to Port 2, therefore filtering out any multimode light. Within the OCT spectral range, ≥90% of the core signal was preserved through the coupler (Fig. 3.1(c)). Transmission curve presented in Fig. 3.1(c) was smoothed to eliminate spectral features of the source. Multimode transmission of the coupler was measured using

a continuous-wave modulated Raman fiber laser (RFL) built in-house, as described in [41], which provides a narrow bandwidth spectrum centered at 1436 nm corresponding to a strong absorption peak of water (main constituent of biological tissues), making it suitable for laser coagulation. The RFL light is injected at Port 3 using a lateral offset splice to excite the inner cladding modes of the injection fiber. For an average input power of 300 mW, approximately 66% of the laser power (i.e. ∼200 mW average power) was transferred to Port 2 through the inner cladding.

3.2.2 Experimental setup

The OCT setup used for this work was previously described in [40, 105]. Briefly, it comprises a polygon-based wavelength-swept laser [106] centered at 1320 nm with a full sweep range of 115 nm. This results in a full width at half maximum (FWHM) of the intensity point spread function of 13 μm in air assuming a Hanning-window for the spectral shape. OCT images were acquired at a rate of 54k axial scans per second providing frames of 4,096 A-lines at a rate of 13 per second, which is suitable for in vivo esophageal imaging as demonstrated in [23]. The system uses an acousto-optic frequency shifter to remove depth-degeneracy, therefore allowing for a full imaging range of ∼6 mm, as well as dual-balanced and polarization-diverse detection.

Figure 3.2 shows a schematic diagram of the experimental setup used to combine OCT imaging with laser tissue coagulation. DCF was integrated to the combined system by splicing the SMF output of the OCT system to the imaging fiber (at S_1). OCT illumination is guided to the sample through the core of the DCF (red path in Fig. 3.2). Coagulation light from the RFL is delivered to the system through the injection fiber at Port 3 using a lateral offset splice (at S_4) as described above. The DCFC, as described in the previous section, was used to transfer light from the RFL within the inner cladding of the imaging fiber. An additional length of DCF and a pigtailed angle-polished connector were spliced (S_2 and S_3, respectively) at Port 2. Port 4 was connected to a beam dump to avoid undesirable back-reflections.

For ex vivo and in vivo imaging, galvanometer-mounted mirrors were used for scanning in the lateral directions. The beams were focused on the sample using a scanning lens (Thorlabs, LSM03) providing an OCT beam spot diameter of 33 μm. The coagulation laser beam spot diameter at the sample (i.e. after the galvanometer-mounted mirrors and scanning lens) was estimated using the 10/90 knife-edge method yielding a width of ∼220 μm. A dispersion compensator (Thorlabs, LSM03DC) was used in the reference arm. For coagulation experiments, a manual shutter was placed immediately after the collimator in order to control the irradiation time. To acquire sensitivity measurements, a calibration arm including an

achromatic lens was used to ensure optimal light re-collection and precise alignment.

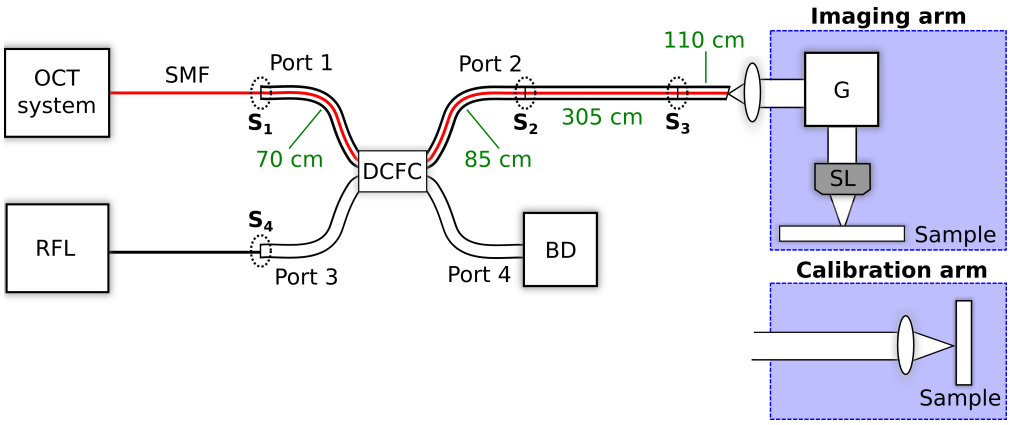

Figure 3.2 Experimental setup combining OCT imaging and coagulation laser (RFL) through a DCFC. Ex vivo and in vivo images were acquired using the imaging arm while the calibration arm was used to acquire sensitivity measurements. DCF lengths are indicated in green. BD : beam dump ; G : galvanometer-mounted mirrors ; SL : scanning lens. S_{1-4} indicates fusion splices.

3.2.3 Image quality

Using DCFs and DCFCs for coherent detection may introduce image artifacts from the crosstalk between inner cladding modes and the fundamental mode (i.e. core mode) occurring at different coupling interfaces. Artifacts occur when inner cladding modes, excited at a primary crosstalk site, propagate within the inner cladding and couple back into the core at a secondary coupling site. Such light travelling through the inner cladding will accumulate a phase shift compared to light travelling through the core. In our system, potential crosstalk sites include fusion splices between the OCT system's SMF and Port 1 of the DCFC (Fig. 3.2 – S_1), splices between segments of DCF (Fig. 3.2 – S_{2-3}), the DCF-air interface at the distal tip of the imaging arm and the fused section of the DCFC. At fusion sites, a misalignment between cores may result in the excitation of some inner cladding modes.

This crosstalk-induced delay is proportional to the optical path difference, defined as the product of the physical distance travelled, l_{DCF}, with the refractive index difference, $\Delta n = n_{fm} - n_{eff}$, between the effective refractive index of a particular inner cladding mode, n_{eff}, and that of the fundamental mode, n_{fm}. The delayed light may interfere with the reference arm causing a ghost image of the sample, i.e. an attenuated replica of the sample shifted with respect to the main image. The delay, ΔL, between the main image and a ghost produced by a certain inner cladding mode is given by [87] :

$$\Delta L = \Delta n \cdot l_{DCF} \tag{3.2}$$

3.3 Results

3.3.1 Sensitivity analysis

In order to quantify respective artifact contributions from each site, we imaged two samples. Sample 1 is a mirror providing specular reflection and, thus, limited excitation of inner cladding modes at the distal end of the system assuming a proper alignment. Sample 2 is a frosted microscopy slide emulating a scattering sample. Index-matching gel was applied to the clear face of the microscopy slide to avoid contribution from the second glass-air interface. A fibered attenuator was used in the imaging arm to avoid saturation and to control the sample arm power to levels representative of biological tissues. Figure 3.3(a-f) shows OCT M-mode (i.e. depth profiles as a function of time) images (1,024 A-lines) of Samples 1 (a-c) and 2 (d-f) acquired with an imaging arm composed of standard SMF (a & d), of DCF without attenuation (b & e) and of DCF with attenuation (c & f). For the latter case, attenuations of 8 and 12 dB were used for Sample 1 and 2, respectively, therefore mimicking signal levels representative of biological tissue imaging. The arrow points at signal from a sample positioned at a particular depth within the imaging range while curly brackets identify the region used for noise level measurement. SMF images are artifact free and their curly bracket region defines the benchmark lowest noise floor. When using the DCF, fine lines appear above the signal line. These lines are constant across A-lines and correspond to the excitation of particular cladding modes each associated with a phase delay. As inner cladding modes have a lower effective index of refraction than the fundamental mode, the axial position of the artifact-ridden region is shallower than that of the main signal. The artifact region contains fewer ghost lines for the mirror than for the scattering sample, suggesting that reflected light excites fewer modes, which is consistent with the limited angular span of the specular reflection.

For each sample type, signal and artifact levels are defined as the maximum intensity in the region identified by the arrow and curly brackets, respectively, and averaged over the 1,024 A-lines of the M-mode image. Signal and artifact levels were measured for different axial positions of Sample 1 (Fig. 3.3(g)) and Sample 2 (Fig. 3.3(h)) across the axial field of view. SMF and DCF signal collection are similar, however, the artifacts cause the noise floor to go up by up to 8 dB for the reflective sample (Fig. 3.3(g) blue curve) and by 9 dB for the scattering sample (Fig. 3.3(h) blue curve) for the regions affected by the artifacts (yellow

curly brackets area). When signal levels are attenuated, artifacts disappear below the noise floor for the reflective sample (Fig. 3.3(g) overlapping red (artifacts) and black (noise) curves) and reach a maximal value of 3.5 dB above the noise floor for the scattering sample (Fig. 3.3(h) magenta (artifacts) and black (noise) curves).

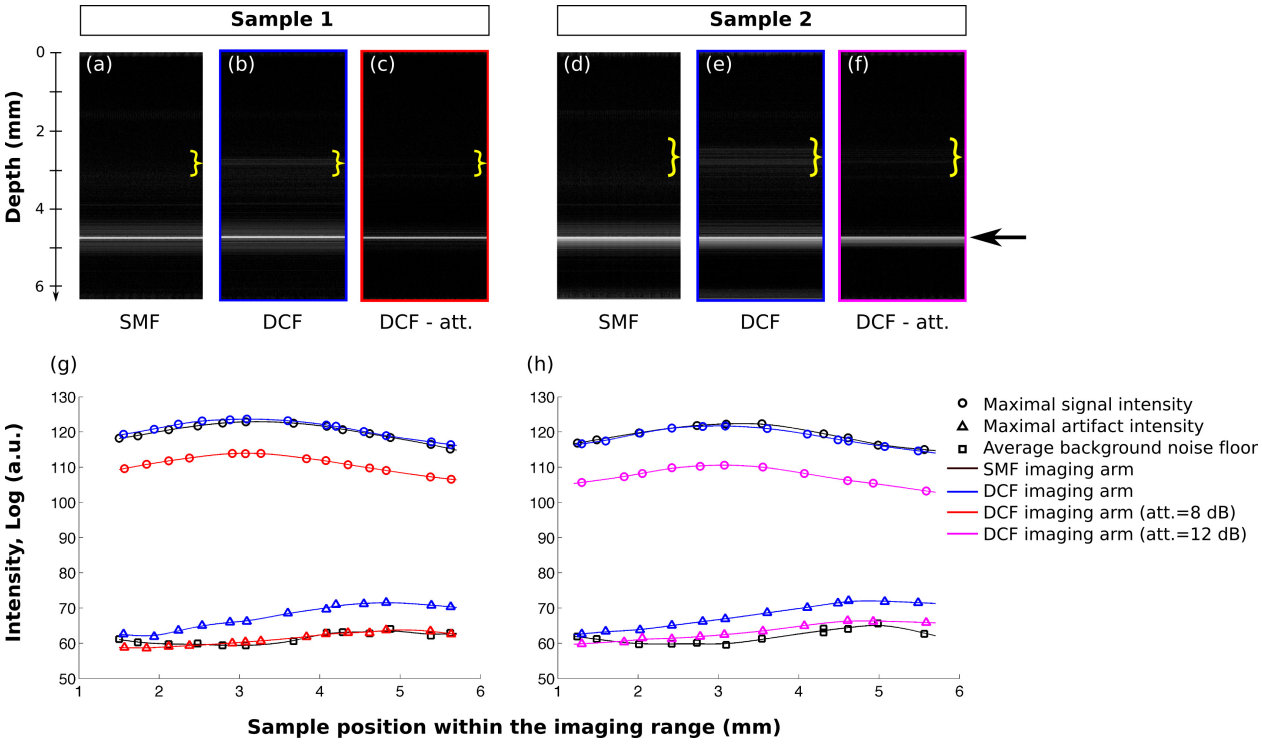

Figure 3.3 Sensitivity analysis. OCT M-mode images of a mirror (a-c : Sample 1) and of a scattering sample (d-f : Sample 2) using a SMF imaging arm (a & d) or a DCF imaging arm (b-c & e-f). Black arrow indicates the position of the samples while curly brackets highlight the regions used for artifact assessment. In (c) and (f), sample power was further attenuated by 8 and 12 dB, respectively. Graphs (g) and (h) present signal (upper curves) and noise (lower curves) levels for different positions of Samples 1 and 2 across the imaging range. Solid lines were obtained using a spline interpolation.

To further track the origin of artifacts, we measured the delay between the signal and ghost lines from Fig. 3.3(b & e), as ranging from 1.6 to 2.3 mm. This delay can be converted into fiber length, l_{DCF}, between crosstalk sites using Eq. 3.2, by comparing the effective index of refraction of the fundamental mode ($n_{fm} \cong 1.4490$) to that of higher order modes having an effective refractive index ranging from $n_{ic} = 1.4468$ to $n_{oc} = 1.4329$. The estimate for l_{DCF} responsible for artifacts thus ranges from 10 cm for artifact contribution from higher order modes to 105 cm for artifact contribution from lower order modes, having an effective index closer to that of the fundamental mode. The contribution of each crosstalk site was

experimentally assessed observing fluctuations of ghost images when each of these DCF segments was moved, as modes propagating through the inner cladding are highly sensitive to the fiber's motion. Doing so, we identified DCF segments on each side of the DCFC (S_1-DCFC and DCFC-S_2), which are the shortest segments in our setup, to be responsible for most of the artifacts. Considering that the excited inner cladding modes are most likely to present an n_{eff} in the upper range, the length of these segments, 70 and 85 cm respectively, correspond well to our prediction.

Figure 3.4 shows in vivo images of human skin (adjacent to the finger nail bed) acquired with the DCFC-based OCT system. Images were taken with the sample at two different axial locations within the field of view by moving the position of the reference arm to ensure the same focusing conditions. The curly bracket highlights ghosts produced from the tissue-air interface when the sample occupies the lower half of the image (Fig. 3.4(b)). Signal coming from subsurface structures is too low to produce ghosts above the noise floor. Figure 3.4(c-d) shows that artifacts are indeed mitigated when index-matching gel is applied on the skin. Artifacts do not alter imaging of sub-surface structures, as they do not overlap with the image of the sample.

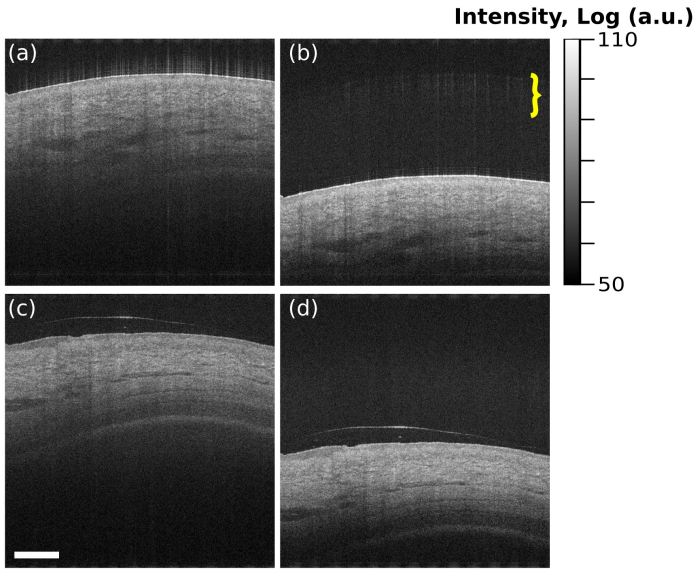

Figure 3.4 In vivo OCT images of human skin (a-b) without and (c-d) with index-matching gel. The sample was imaged at different positions within the imaging range. The position of the focal plane is constant relative to the sample across images. Curly bracket highlights ghost lines. Scale bar : 1 mm.

3.3.2 Simultaneous optical coherence tomography imaging and laser coagulation

A preliminary coagulation experiment was performed on a sample of swine esophagus ex vivo to assess the potential of the multimodal system to perform real-time monitoring of tissue laser coagulation. The coagulation process can be monitored through the increase of the scattering properties of the tissue which results from the thermal denaturation of proteins [107]. The RFL was set to provide a duty cycle of 1% and a repetition rate of 20 Hz, resulting in a pulse width of 500 μs. Two different average power settings, 113 mW and 172 mW, were used, providing pulse energies of 5.7 mJ and 8.6 mJ on the sample, respectively. Figure 5 presents images taken before (a & e) and after (c & g) irradiation as well as M-mode images (b & f) acquired in real-time for each power setting. For both power settings, a region of increased scattering at the surface of the tissue can be observed after irradiation. This increased scattering also caused a shadow obscuring the view of deeper layers. M-mode images Fig. 3.5(b & f) show the real-time progression of the thermal injury during the irradiation. In Fig. 3.5(b), for the lower power setting, the coagulation threshold (yellow arrow) is reached $\sim$1.4 s after the beginning of the irradiation (corresponding to 14 pulses), which results in a sudden change in scattering properties. As heat propagates through the tissue over time, tissue coagulation extends to deeper layers. For the highest power setting, the coagulation threshold (yellow arrow) is reached after only 3 pulses (red arrows) as seen in Fig. 3.5(f). Individual pulses are seen on OCT images as what may be the result of the motion of scatterers due to a thermal excitation. Figures 3.5(d & h) show a bright field microscopy image (Olympus, UC500) of the coagulation spots resulting from laser irradiation using the DCFC-based system. The laser-induced marks measure $\sim$315 μm and $\sim$930 μm for the low and high pulse energies, respectively.

Fig. 3.5(i-j) shows the reflected signal intensity as a function of depth (i.e. light attenuation) for the lower (Fig. 3.5(i) – 5.7 mJ/pulse) and higher (Fig. 3.5(j) – 8.6 mJ/pulse) power settings at different time points before and after coagulation. Linear fits, solid lines, were performed after averaging 265 consecutives A-lines within each region of interest. In each case, the attenuation slope is more pronounced post-coagulation. Coagulation also results in superficial signal increase due to scattering.

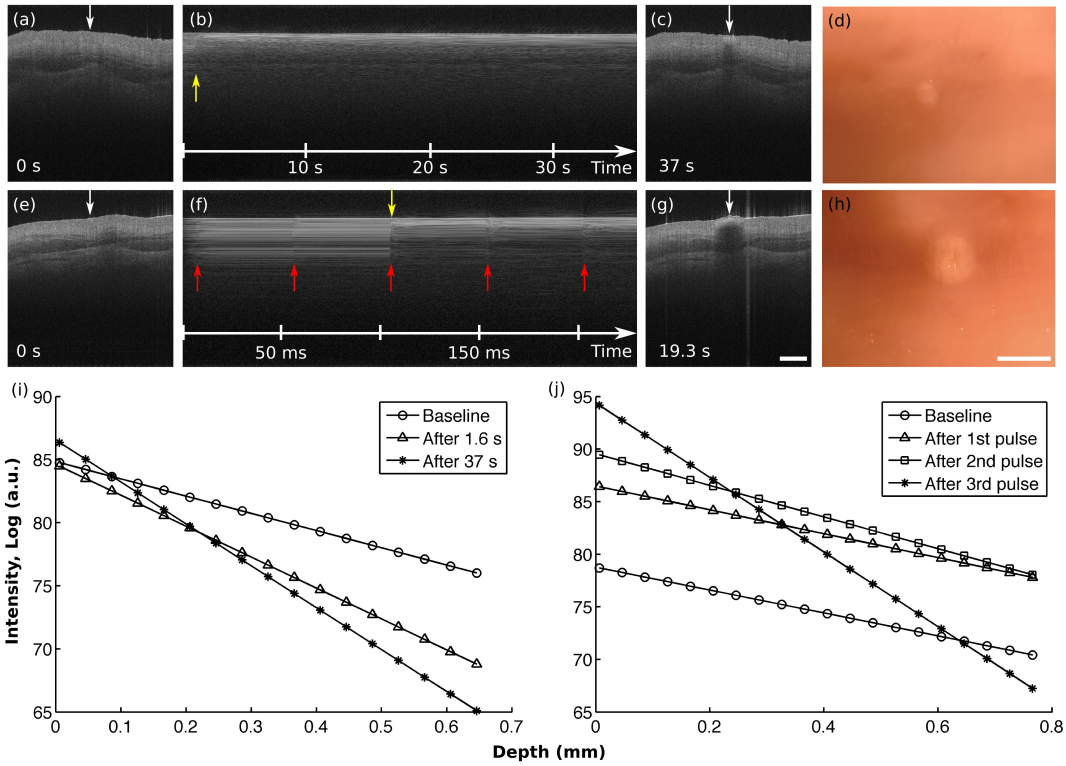

Figure 3.5 OCT images of swine esophageal tissue before (a & e) and after (c & g) laser coagulation are shown along with simultaneous M-mode acquisitions (b & f) showing real-time monitoring of coagulation processes. The M-mode in (b) has been down-sampled by a factor of 1,000. Upper and lower panels show results of irradiation performed using pulse energies of 5.7 mJ and 8.6 mJ, respectively. Red arrows highlight individual coagulation laser pulses. Yellow arrows indicate reaching coagulation threshold. Right panels (d & h) show microscope photographs (4x) of the coagulation marks. Attenuation curves for (i) lower and (j) higher power settings shown at different time points. Scale bars : 1 mm.

3.4 Discussion and conclusion

OCT, used along with laser tissue coagulation, shows promising potential to guide biopsy in the context of surveillance of Barrett's esophagus. However, no system allowing for real-time monitoring of the coagulation laser delivery has been developed yet. Herein, we investigated the use of a DCFC-based system allowing OCT (through the core) and coagulation laser delivery (through the inner cladding) to be performed simultaneously through a single fiber. Such a system allows the use of a multimode laser diode, which is a relatively low-cost commercial option.

We developed a dedicated DCFC enabling injection of the coagulation laser light into the inner cladding of a DCF. This coupler provides single-mode transmission of more than ∼90%

over the wavelength range of our OCT system as well as 66% multimode coupling at 1436 nm. This novel scheme allows the coupling of high power laser light necessary to induce coagulation, without free space optics, thus providing safe and alignment-free procedures compatible with clinical practice. The first DCFC prototype was developed using fibers on hand and could in theory provide multimode coupling of more than 97%. To minimize multimode losses, we believe that fibers combination, ITR, as well as pre-processing and fabrication techniques could be further improved.

A quantitative sensitivity analysis of the DCFC-based OCT system was performed to assess the effect of crosstalk-induced artifacts on the imaging quality. These artifacts are the result of light that travels in the inner cladding, therefore accumulating a delay compared to the fundamental mode, and interferes with the reference signal. The effect of multimodal crosstalk on OCT imaging was previously assessed for fiber bundles [86, 87] and large-core fibers [88], but has not been thoroughly assessed in the case of DCF-based imaging. Our analysis showed that the artifacts could be as high as 9 dB above the typical OCT background noise floor when imaging a scattering sample and great care should therefore be taken for their minimization. For a reflectivity comparable to biological tissue, the SNR penalty of using DCF is reduced to $\sim$3 dB as the amplitude of the artifacts is proportional to the tissue reflectivity. Moreover, we have shown that, when imaging a biological tissue, most artifacts arise from the air-tissue interface and that using index-matching gel to reduce reflectivity of this interface is sufficient to completely suppress ghost images under our experimental conditions. In addition, for optimal sample positioning, typically in the first half of the imaging range, we observed that no artifacts are visible and the system SNR is not altered.

As mentioned in [74, 89], another way to manage artifacts is to add enough fiber length to create a delay that would be higher than the depth of the imaging range. For a 6-mm imaging range, this requires adding meters of fibers between each coupling sites. By measuring the signal-ghost delay, we showed that the DCFC was responsible for most artifacts (either as a primary or secondary crosstalk site) such that DCF segments surrounding the coupler are critical. Therefore, it is believed that using a DCFC with much longer ports could push the artifacts out of the imaging range. Even tough this condition was not met in the current setup, the delay between the signal and ghost images was sufficient to avoid any overlapping.

Using the DCFC-based system, simultaneous and co-localized OCT imaging and laser coagulation was performed. Our results show that the DCFC-based system allows real-time monitoring of dynamic processes associated with laser coagulation through changes in scattering properties. In addition, laser pulses were seen on OCT images as speckle motion, which may be due to a thermal shock wave. We, as well as others, have demonstrated real-time OCT

imaging of thermal effects of laser irradiation [55, 56, 101]. Our DCFC-based system however presents the advantage of being intrinsically co-registered and compatible with an endoscopic implementation. Co-registration of the monitoring modality with laser irradiation is of paramount importance in the context of laser marking and therapy as it ensures the safety and the simplicity of the procedure.

Using the real-time feedback provided by OCT, it was possible to determine that the cumulative effect of 3 pulses of ∼8.6 mJ each was sufficient to reach the coagulation threshold of esophageal swine tissues. It was shown previously that using single-mode delivery (beam spot size of ∼37 μm), a single pulse of more than 7 mJ was sufficient to create a visible coagulation mark [41]. As expected, using the DCF inner cladding to deliver the coagulation laser requires higher energy to yield equivalent results, as the beam spot size (∼220 μm) is much larger and, therefore, less spatially confined. The larger beam spot represents the advantage that the mark produced is necessarily larger than that of a single-mode delivery and, therefore, better visible under white-light endoscopy in the context of biopsy guidance. We believe that using a higher peak power along with an adequate combination of pulse width (while maintaining temporal confinement) and repetition rate will allow a single pulse to create a visible mark enabling on-the-fly laser marking. Further optimization of the DCFC multimode coupling would likewise increase the pulse energy reaching the sample.

The RFL was used for this proof-of-principle, as it was readily available. Based on the results presented here, it should be possible to replace the RFL with a multimode diode laser, significantly reducing cost and complexity while also enabling simple control and synchronization of pulse parameters. In conclusion, we have herein demonstrated a DCFC-based system using a novel DCFC to simultaneously combine OCT imaging with laser coagulation for the first time, to the best of our knowledge, through a single fiber. The combined system is intrinsically co-registered and induces minimal imaging quality degradation. In combination with suitable laser source, this system has the potential to enable on-the-fly laser marking with concurrent OCT guidance and monitoring of the marking process.

Acknowledgments

The authors thank Mikael Leduc for precious laboratory help as well as Etienne De Montigny and Mathias Strupler for fruitful discussions. This work was supported in part by Ideas to Innovation Grant from the Natural Sciences and Engineering Research Council of Canada (NSERC) and by the National Institutes of Health, grant P41 EB015903. KB and WJM were supported by a NSERC graduate scholarship ; KB is additionally supported by the Fonds de recherche du Québec – Nature et Technologies (FRQ-NT) International Training Program.

3.5 Complementary results : dynamic laser marking

Using the experimental setup shown in Figure 3.2, it was possible to achieve single-pulse laser marking therefore demonstrating DCF-based dynamic laser marking ex vivo. To do so, the galvanometers scanning speed and the high-power laser repetition rate were adjusted in order to ensure that the energy, at each pulse, hit a different location on the tissue. OCT images were acquired simultaneously at ∼30 frames/s. A repetition rate of 10 Hz and a pulse width of 1 ms were used. The pulse energy and averaged power at the sample were 17 mJ and 170 mW, respectively.

Figure 3.6 presents the results of dynamic laser marking on swine esophageal tissue showing an OCT image acquired at the end of the marking procedure along with a white light microscope photograph. Coagulated regions are characterized by an increased scattering creating a shadow over underlying structures. Single-pulse coagulation produces clear margins, as it is free of heat dissipation, resulting in a high marking contrast compared to surrounding tissue. The laser marks are ∼275 μm in diameter, which is close to the measured MM beam spot size.

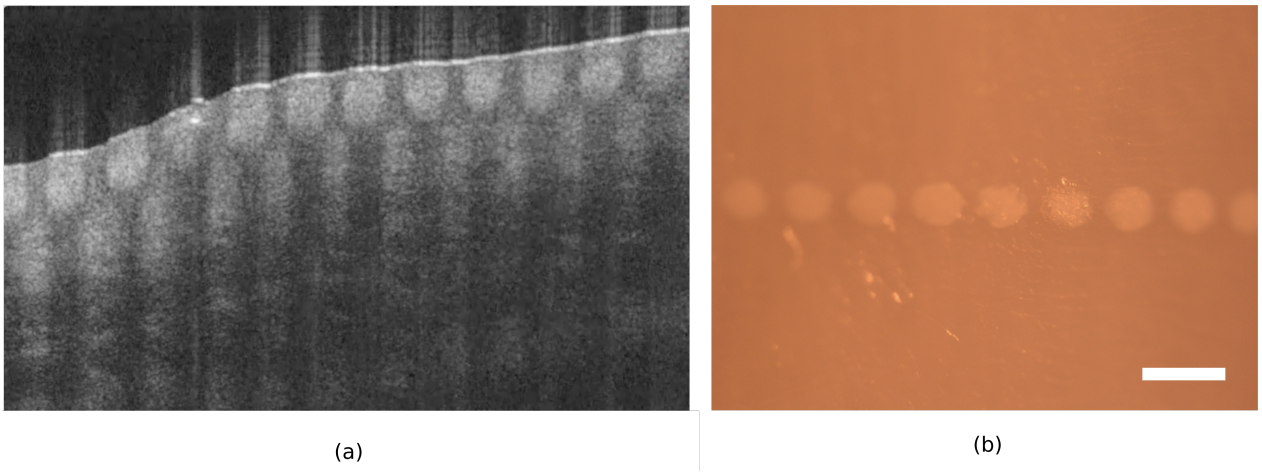

Figure 3.6 Dynamic laser marking results : (a) OCT image acquired at the end of the marking procedure and (b) 4X white light microscope photograph. Scale bar = 500 μm.

CHAPTER 4 MODELING SINGLE- AND MULTIMODE PROPAGATION

Chapter 3 showed that single-pulse laser marking is possible using a DCF-based benchtop system. In order to translate that system into the clinic, an endoscopic approach accommodating both the SM and MM channels is required. We herein aim at developing a numerical model of a DCF, including both SM and MM propagation of light, in order to simulate and optimize DCF-based optical systems. To fully grasp the subtleties involved in such a model, we will first describe SM and MM illuminations in terms of coherence and etendue. The DCF model herein developed will then be presented. The model is further validated and used to evaluate potential designs for the laser marking probe and study MM light propagation. This Chapter will finally conclude by discussing different designs suitable for endoscopic marking. A portion of this work, including the experimental validation, was presented at *SPIE Photonics West* conference in 2016 and published as a conference proceeding entitled : "Towards in vivo laser coagulation and concurrent optical coherence tomography through double-clad fiber devices".

4.1 SM versus MM propagation

The SM and MM outputs of the DCF represent two different types of illumination such that, even though they both propagate through the same optics, they will show distinct propagation behaviours. To explain the distinction between SM and MM propagations, we will here use the concepts of coherence and etendue as defined in Ref. 11. We introduced the etendue earlier to describe the propagation within a DCFC using Equation 2.1, but it can similarly be used to describe light beams as we will see below [1].

4.1.1 Mutual intensity

In order to describe the nature of a partially coherent beam and to derive relations for the etendue, we use the mutual intensity. The mutual intensity ($J(\vec{\rho}, \vec{\rho'})$), which characterizes the correlation between two fields located at different radial or lateral positions, $\vec{\rho}$ and $\vec{\rho'}$, in the same axial plane, as shown in Figure 4.1a, can be expressed as follows :

$$J(\vec{\rho}, \vec{\rho'}) = \langle E(\vec{\rho}) E^*(\vec{\rho'}) \rangle, \tag{4.1}$$

1. Some authors used the term "throughput" to describe the etendue of an optical system to avoid confusion with the etendue of the light beam.

where $E(\vec{\rho})$ and $E(\vec{\rho'})$ describe the fields at locations $\vec{\rho}$ and $\vec{\rho'}$, respectively, and $\langle\cdot\rangle$ represents the temporal average. For a partially coherent beam, the mutual intensity function can be expressed using independent intensity (I) and coherence (μ) functions :

$$J(\vec{\rho_c}, \vec{\rho_d}) = I(\vec{\rho_c})\mu(\vec{\rho_d}), \tag{4.2}$$

where $\vec{\rho_c}$ and $\vec{\rho_d}$ denote the mean vector and the difference vector, respectively, between a pair of points $\vec{\rho}$ and $\vec{\rho'}$, as illustrated in Figure 4.1a.

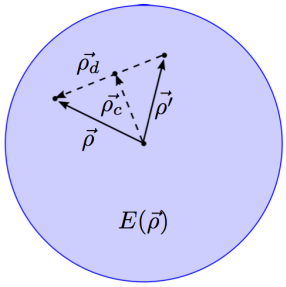

(a)

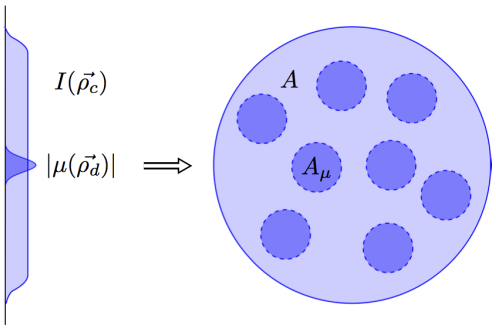

(b)

Figure 4.1 (a) Coordinate system used for the mutual intensity and (b) schematic representation of a partially coherent beam showing individual modes within an area of uniform intensity. Adapted from [11].

The intensity and coherence functions can each be associated with a characteristic area. The intensity function is associated with the total beam area as defined by :

$$A = \frac{|\int I(\vec{\rho_c})d^2\vec{\rho_c}|^2}{\int I(\vec{\rho_c})^2 d^2\vec{\rho_c}} = \frac{W^2}{\int I(\vec{\rho_c})^2 d^2\vec{\rho_c}}, \tag{4.3}$$

where W is the total beam power and $d^2\vec{\rho_c} \to 2\pi\rho d\rho$. By convention, the coherence area is

described as :

$$A_\mu = \int |\mu(\vec{\rho_d})|^2 d^2\vec{\rho_d}. \tag{4.4}$$

The number of coherence areas, which may be conceptualized as the number of modes, included within the total beam area is therefore :

$$N_\mu = \frac{A}{A_\mu}. \tag{4.5}$$

Figure 4.1b shows a representation of the intensity and coherence functions along with their characteristic areas. N_μ refers to the number of spatial "modes" supported by the beam. For the case of $N_\mu = 1$, the beam is said to be perfectly coherent, whereas, if $N_\mu > 1$, the beam is partially coherent. A partially coherent beam can be described as a combination of coherent "beamlets", each of coherence area A_μ, as shown in Figure 4.1b. The etendue of a beam G is directly proportional to the number of modes it supports as described by :

$$G = \kappa^{-2} N_\mu = \kappa^{-2} \frac{A}{A_\mu}, \tag{4.6}$$

where κ is related to the angular spatial frequency by $k = 2\pi\kappa$ as defined in Ref. 11.

4.1.2 Etendue

Let us now consider the case where the beam propagates in free space between two planes separated by distance z as shown in Figure 4.2. I_0 and μ_0 describe the intensity and coherence functions, respectively, at the original plane, whereas I_1 and μ_1 are similarly associated with the second plane.

It can be shown that, in free space propagation, there exists a scaled Fourier transform relationship between $I_1(\vec{\rho_{1c}})$ and $\mu_0(\vec{\rho_{0d}})$, and another one between $I_0(\vec{\rho_{0c}})$ and $\mu_1(\vec{\rho_{1d}})$. Using Equations 4.3 and 4.4 and applying Parseval's theorem yield :

$$A_1 = \frac{z^2}{\kappa^2 A_{\mu 0}}, \tag{4.7}$$

$$A_{\mu 1} = \frac{z^2}{\kappa^2 A_0}, \tag{4.8}$$

which describe the beam and coherence areas after propagation. From these equations, one

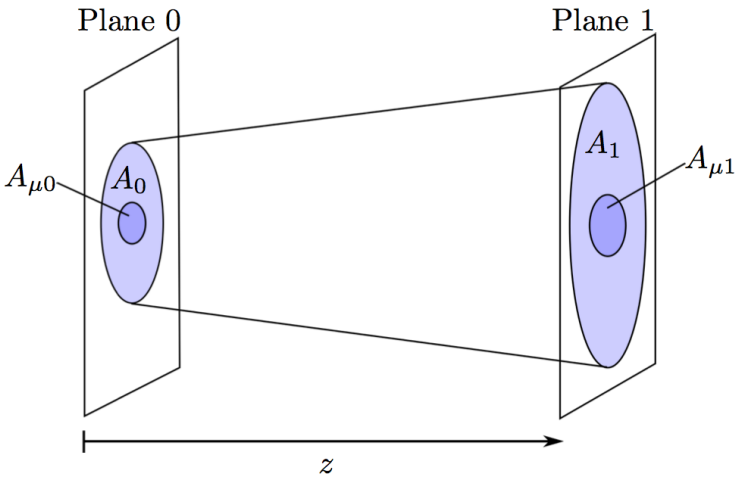

Figure 4.2 Free-space propagation between planes 0 and 1 each associated with corresponding total beam and coherence areas.

can observe that both A_1 and $A_{\mu 1}$ expand proportionally to z^2/κ^2, meaning that a diverging beam will be associated with a proportional increase of its coherence area. Also, re-arranging the terms :

$$\frac{A_0}{A_{\mu 0}} = \frac{A_1}{A_{\mu 1}}, \tag{4.9}$$

implies that the etendue is conserved upon propagation through free space. The etendue will also be conserved through an imaging system assuming there is no power loss. This conservation law can also be written as :

$$G = A_0\Omega_0 = A_1\Omega_1, \tag{4.10}$$

where $\Omega_0 = A_1/z^2$ and $\Omega_1 = A_0/z^2$ represent the beam divergences at each of these planes. Equation 4.10 can be recognized as the conservation law known from geometrical optics. Combining Equations 4.6 and 4.10, we can then obtain :

$$A_{\mu 0}\Omega_0 = A_{\mu 1}\Omega_1 = \kappa^{-2}, \tag{4.11}$$

which states that, independently of the number of modes N_μ, the far-field angular divergence is dictated by the width of the beam's local coherence, $A_{\mu 1}$, and that its global angular divergence is equivalent to that of a purely coherent beam described by a coherence area A_μ. In the SM regime, a Gaussian beam corresponds to a coherent beam as $N_\mu = 1$. Since

the mutual intensity can be described by independent intensity and coherence functions, we write :

$$J_0(\vec{\rho_{0c}}, \vec{\rho_{0d}}) = I_0(\vec{\rho_{0c}})\mu_0(\vec{\rho_{0d}}) = \left(I_0 \exp(-2\rho_{0c}^2/\omega_0^2)\right)\left(\exp(-2\rho_{0d}^2/2\omega_0^2)\right), \tag{4.12}$$

where ω_0 corresponds to the waist of the beam. For the fundamental Gaussian beam, $A = A_\mu$, and, per Equation 4.6, the etendue is $G = \kappa^{-2}$. Gaussian propagation is described as :

$$A_1 = \frac{z^2}{\kappa^2 A_0}, \tag{4.13}$$

$$A_{\mu 1} = \frac{z^2}{\kappa^2 A_0}. \tag{4.14}$$

This result implies that the beam and coherence areas expand identically and, consequently, the beam remains coherent.

A MM beam, on the other hand, corresponds to a partially coherent beam supporting multiple modes. Its etendue is described as :

$$G = \kappa^{-2} N_\mu, \tag{4.15}$$

resulting in a beam propagation described by :

$$A_1 = \frac{z^2}{\kappa^2 A_0} N_\mu, \tag{4.16}$$

$$A_{\mu 1} = \frac{z^2}{\kappa^2 A_0}. \tag{4.17}$$

From Eq. 4.16 and 4.17, we see that, in the MM case, the beam and coherence areas do not expand identically. Indeed, the beam area expands with an effective solid angle N_μ times larger than that of the coherence area. Consequently, a partially coherent beam, compared to a coherent beam and given the same propagation distance, diverges much more rapidly.

4.1.3 Imaging with a DCF

To illustrate this concept, let us model the inner cladding MM output as a combination of beamlets emanating from different points, whereas the SM core signal is represented by

a purely coherent beam. Both beams are propagated through a GRIN lens collimator as shown in Figure 4.3. The SM beam (in red) exits the system perfectly collimated in the case where the fiber tip is located at the front focal plane of the lens. The fields composing the MM beam (in blue) will also exit collimated, but angled with respect to the optical axis. The superposition of these fields (shaded blue area) will create a beam that first narrows, creating a waist located at the lens back focal plane, and then will quickly diverge out. This "waist location" corresponds to the exit pupil plane of the optical system. The exit pupil corresponds to the image of the aperture stop created by the limited NA of the MM core, which, in this case, is positioned at infinity.

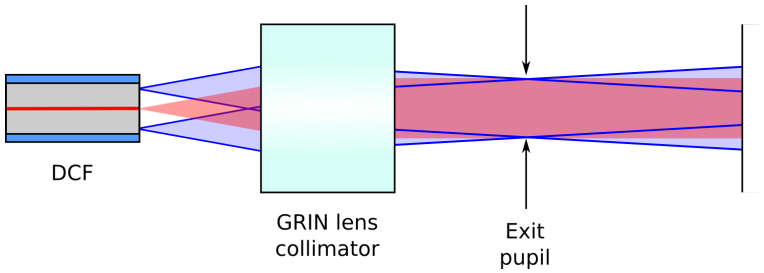

Figure 4.3 SM versus MM illumination through a GRIN lens collimator. SM beam is represented in red whereas the MM beam is represented by the shaded blue area. The different fields used to describe the MM propagation are outlined in blue.

For an imaging system, this effect could lead to the creation of two distinct waist locations for the SM and MM channels. This is the case for a single-lens imaging probe, for example, as shown in Figure 4.4a. Unlike the SM beam, which focuses light at the image plane, the MM minimal beam diameter is located at the exit pupil plane and, then, diverges out as it propagates. In order to achieve co-localisation of the SM and MM waists, at least two lenses are necessary as shown in Figure 4.4b. A 4-f system is an example of such a combination where the second lens is used to image the intermediate pupil onto the image plane of the system.

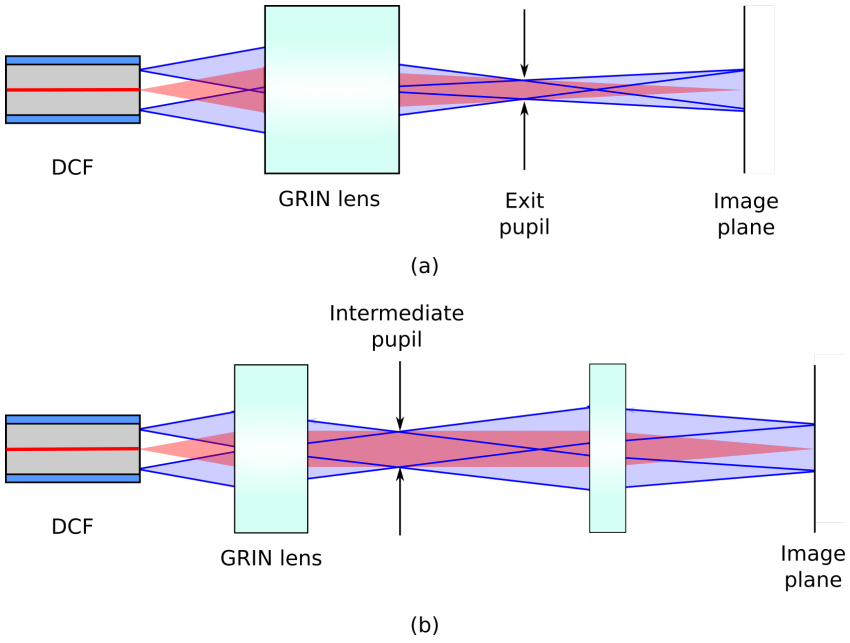

Figure 4.4 (a) Single-lens imaging system showing the two distinct waist locations. (b) 4-f system where the SM and MM waist locations coincide.

4.2 DCF model

Optimizing the catheter's distal optics involves developing a model that adequately simulates both single- and multimode propagations. The SM propagation will define the OCT imaging resolution and penetration. The MM propagation is used for laser marking such that the irradiance distribution along the optical axis is the parameter of interest in this case. Optical modeling is performed using design software such as OpticStudio (formerly known as Zemax), which can operate one of several modes defining how the ray tracing is achieved. Most imaging systems are typically modeled using a sequential mode. A sequential approach assumes a pre-defined sequence of surfaces that must be hit by the rays being traced. As seen in the previous section, we showed that a MM beam can be modeled as a superposition of coherent beams, which could be achieved using different fields (i.e. beamlets) emanating from different points over the inner cladding's area. However, using the sequential mode, this setup can quickly become cumbersome as several fields are required to have a good representation. In addition, most analytical tools provided in the sequential mode are not adapted to such a configuration. We therefore make use of the non-sequential mode to describe the MM beam. The non-sequential mode implies that there is no pre-defined sequence such that the objects that are hit by the rays are only defined by the physical positions and properties of said objects. This means that the rays may hit any part of an object, may hit an object multiple

times, or not at all. This is not the case for the sequential mode where all the rays must hit the same surfaces in the same order.

In this section, we therefore evaluate that approach and experimentally verify the results. The optical design software OpticStudio [2] was used throughout this work. To reflect the experimental setup, we used the specifications of a commercial DCF (DC1300, Thorlabs) described in Table 4.1.

Table 4.1 Fiber specifications describing the DCF (DC1300, Thorlabs)

Parameter	Core	Inner cladding	Outer cladding
Physical diameter	9 μm	105 μm	125 μm
Mode field diameter	9.2 μm	-	-
Numerical aperture	0.12	0.2	-

To model both the SM and MM channels of the DCF output, two different strategies were assessed. The first case, which was reported in Ref. [108], uses a multi-configuration approach where the SM channel is modeled in sequential mode, whereas the MM output is described as a non-sequential source. The second strategy uses a pure non-sequential mode in a single configuration where both the SM and MM channels are modeled as non-sequential sources.

For the sequential model, the SM signal is modeled as a Gaussian output described by the core mode field diameter and NA. For the non-sequential model, the SM signal is modeled as a diode source, described by its divergence and presents a Gaussian profile. The MM output, on the other hand, is modeled as a circular source using multiple rays distributed across the area of the inner cladding. Each ray exits the source with an angle comprised within the cone limited by the inner cladding's NA. This representation, here again, corresponds to the concept of using several coherent beamlets to simulate a MM propagation. The impact of the SM core on the MM output is neglected. Table 4.2 provides the detailed parameters for each channel for the non-sequential mode. Figure 4.5 shows both outputs as modeled using the pure non-sequential mode. Both strategies yield the same results, but each presents different strengths from an optimization point of view. For the multi-configuration approach, the sequential treatment of the SM allows simulating fiber coupling. The paraxial Gaussian beam analyses can also be used facilitating the SM beam optimization. For the pure non-sequential approach, since a single configuration is used, the effect of a change of optics on the beam spot size and working distance can be observed simultaneously for both channels.

2. Zemax OpticStudio 16.5 SP3, Professional Edition.

Table 4.2 Non-sequential parameters used to described SM and MM outputs

SM		MM	
Parameter	**Value**	**Parameter**	**Value**
Object type	Source diode	Object type	Source two angle
X and Y divergence[a]	5.2°	X and Y half width	0.052 mm
X and Y-superGauss	1	X and Y half angle	7.6°
X and Y-sigma $(s_{x,y})$[b]	4.6 μm	Spatial shape[c]	1
X and Y-width $(H_{x,y})$[b]	1	Angular shape[c]	1

a. Assuming $\lambda = 1310$ nm and using $\theta = \lambda/\pi\omega_0$ with $\omega_0 = 4.6$ μm.

b. Describing the following spatial distribution : $I(x,y) = I_0 e^{-2\left(\left(\frac{x}{s_x}\right)^{2H_x}+\left(\frac{y}{s_y}\right)^{2H_y}\right)}$.

c. Defining a rectangular (0) or elliptical (1) shape.

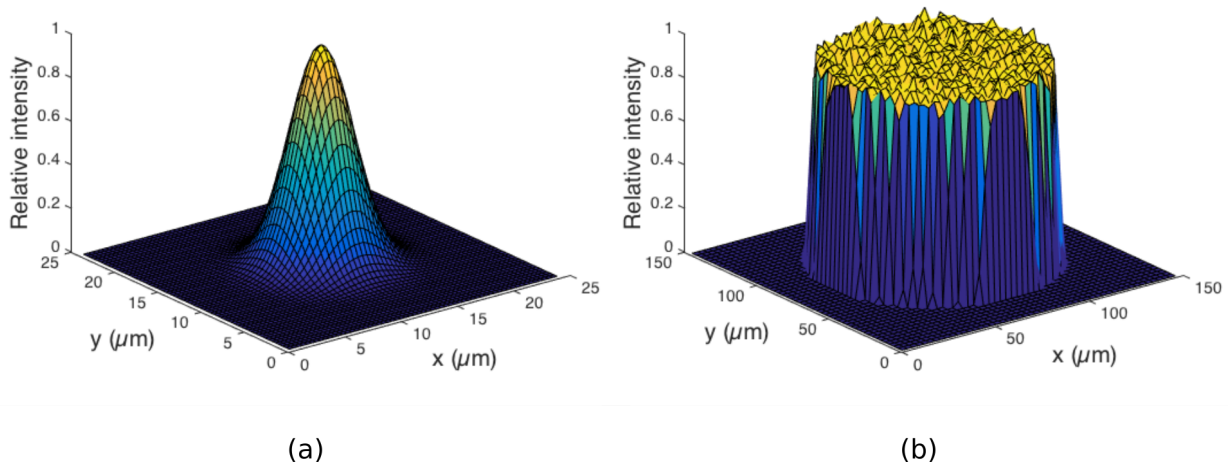

Figure 4.5 Non-sequential representation of the modeled (a) SM and (b) MM outputs, represented as Gaussian and flat-top beam profiles, respectively.

4.2.1 Model validation

To validate the model and verify that the non-sequential source can indeed well describe a MM propagation, a forward-viewing GRIN lens-based catheter was fabricated and tested. Such an assembly reproduces the conditions shown in Figure 4.4a. The design consists of a 5.57-mm long GRIN lens (GRIN2913, Thorlabs) directly placed against a ferrule containing the DCF. The GRIN profile (SLW-1.8) is described by Eq. A.5 using the parameters presented in Table A.2 (see Annexe A). Using this assembly, we experimentally imaged the MM beam at different locations along the optical axis using a charge coupled device (CCD) camera (WinCamD, Data Ray Inc.) placed on a translation stage to obtain measurements of MM beam spot size. A swept-source (1260-1375nm) injected into the inner cladding through the DCFC, along with a fibered attenuator, was used as the illumination source. To validate the simulation for the SM configuration, the back coupling intensity reflected from a normal incidence mirror was measured at different axial positions. Simulation results were obtained by computing the fiber coupling efficiency through a symmetric source-receiver system and plotted against half the lenses' separation (corresponding to the experimental lens-mirror separation).

Figure 4.6a shows the evolution of the beam spot size for SM and MM as a function of depth, comparing experimental data to simulation results. Using the multi-configuration model, a working distance of $\sim$7.5 mm and an SM $1/e^2$ waist diameter of 37.7 μm are obtained. The MM beam was characterized by its half-width at half maximum (HWHM) providing a value of $\sim$208 μm at the image plane. For both channels, a good agreement is observed between simulation and experimental data. This result shows that the beamlets approach to simulate a MM beam is indeed valid and provides accurate estimation of optical performances. From this result, one can see that the MM beam spot size first decreases, reaching a minimal size at about 4 mm away from the lens, and, then, diverges. As seen previously, the discrepancy in waist location between the SM and MM channels comes from the fact that the focal and exit pupil planes in this system do not coincide. Simulated and experimental MM beam profiles are presented in insets on Figure 4.6b. In both cases, one can see that a sharp image of the fiber tip is created at the image plane (i.e. $\sim$7.5 mm from the end face of the GRIN lens). For the simulated spots, a texture due to the ray distribution discretization is observed. For the experimental results, the speckle pattern is washed out due to the wavelength sweeping of the source used. The effect of the core, which is neglected in the model, can be observed experimentally and results in a donut-shaped beam. A brighter region is also observed in the center of the beam, which could be explained by a higher density of the low-order modes populating the DCF. The dark line present on the left side of the beam likely corresponds to

a defect of the fiber-end facet or the GRIN lens.

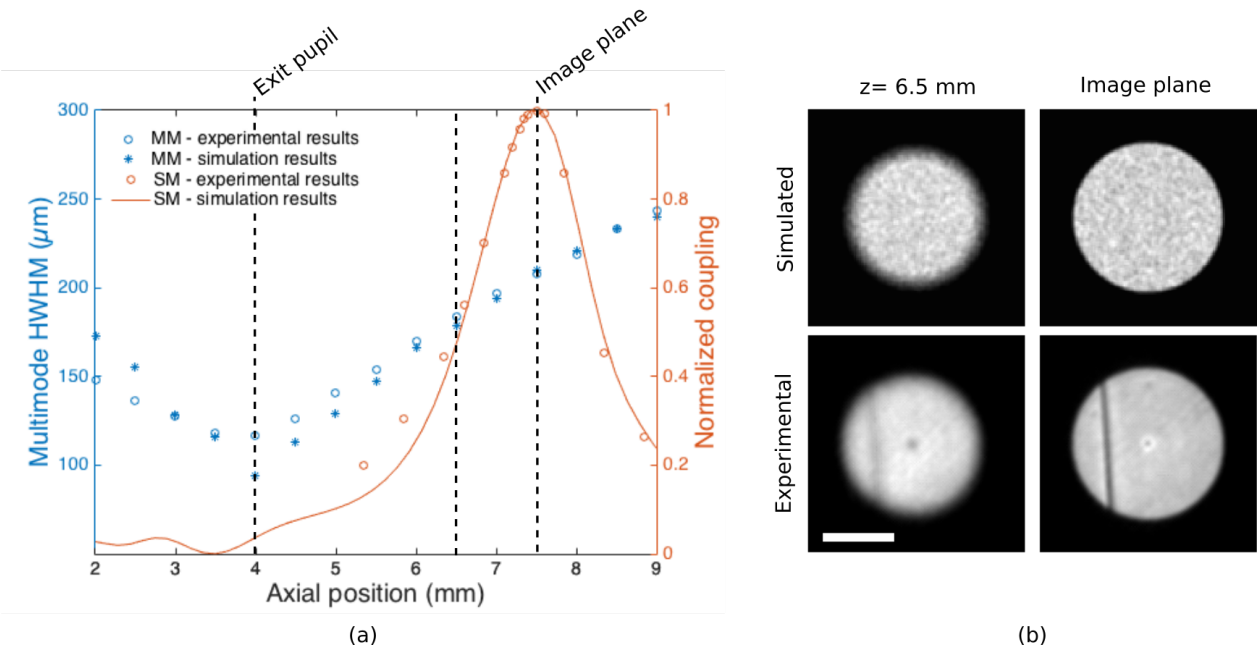

Figure 4.6 Experimental versus simulation results. (a) MM beam HWHM (left axis in blue) and SM coupling efficiency (right axis in orange) both as a function of axial position with respect to the end face of the GRIN lens. The exit pupil and image plane are identified by dashed lines. (b) MM beam profiles at 6.5 mm and at the image plane obtained through non-sequential simulations using 150,000 rays (top row) and experimentally with a CCD camera (bottom row). Scale bar : 200 μm.

4.3 Catheter design optimization

With the use of the model, we evaluated and optimized potential optical designs for the laser marking probe. The constraints of the design are defined by the clinical settings in which the probe will be used. Figure 4.7 shows a schematic of the probe as used in a typical clinical system. The distal optics consists of a ferrule, which aligns the fiber along the optical axis, some focusing optics and a prism or a mirror for side-viewing. The distal optics is contained in a hypotube, which is fixed to the torque coil (not shown) that will convey torque and rotation to the distal end of the probe. The assembly is contained within a transparent window tube placed at the center of the balloon when fully inflated. The working distance (WD) is dictated by the balloon size, which typically varies between 14 and 20 mm. The WD is defined as the distance between the last optical surface and the SM waist position (also called image plane). To optimize imaging quality, the SM waist is positioned 0.5 to 1 mm deep within the

tissue, resulting in WD between 7 and 10.5 mm, depending on the balloon size used. The SM waist diameter will determine the imaging resolution and depth range (i.e. twice the Rayleigh range), such that a compromise must be made. For compatibility with commercially available balloon-sheaths, torque coil and hypotube, the distal optics diameter is set to 1 mm. The rigid length of the distal optics and hypotube should be minimized to ensure the probe's flexibility and reduce nonuniform rotation distortion (NURD) artifacts [3].

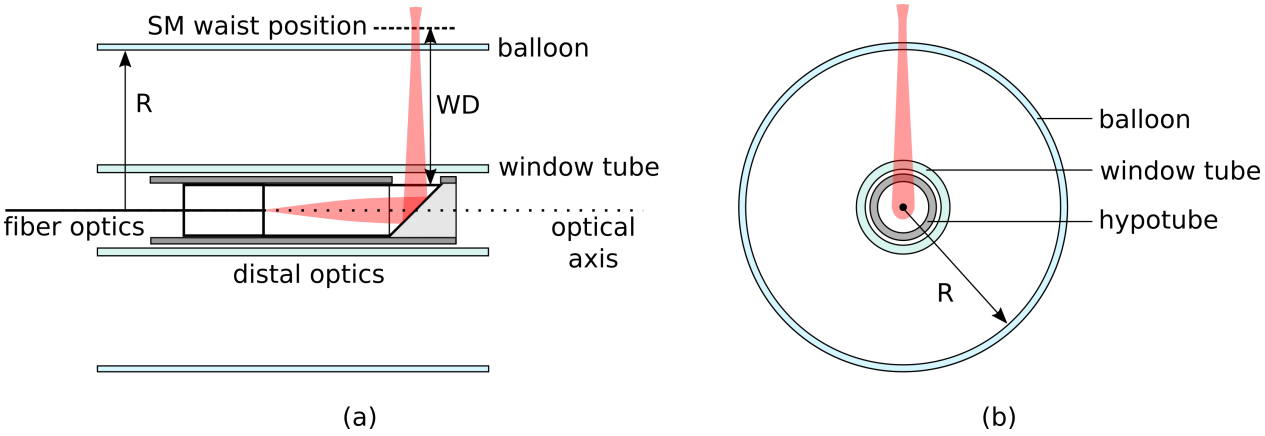

Figure 4.7 (a) Longitudinal and (b) cross-sectional schematics of a typical balloon catheter showing the distal optics included in the hypotube, the window tube and the balloon. WD : working distance, R : balloon radius.

4.3.1 GRIN lens-based designs

Single-lens design

Typical GI catheters are based on a single GRIN lens design including a spacer, which acts as a beam expander, a GRIN lens and a reflective prism for side-viewing. This system images the fiber tip with a certain magnification, applied to both the SM and MM beams. The non-sequential model was used to simulated different combinations of spacer and GRIN lens lengths (presented in Table 4.3) resulting in different magnification factors for a 7.5-mm WD probe for use in a 14-mm balloon-sheath. It should be noted that the window tube was not considered here for simplicity. However, the cylindrical window is known to induce astigmatism and compensating for this curvature using, for example, a prism with a curved face is necessary. For this simulation, the spacer was modeled as a glass rod made of fused

3. NURD arises because of the nonuniform rotational velocity of the probe distally, even if driven at constant speed proximally [109]. NURD depends on mechanical properties of the catheter and can be exacerbated by tortuous bends.

silica and the SLW-1.0 glass from SELFOC® was used for the GRIN lens (properties defined in Table A.2). A 0.7 mm x 0.7 mm rectangular BK7 prism was used to deflect the light.

Table 4.3 Simulation results for a 7.5-mm working distance single GRIN lens-based probe

No	SM $1/e^2$ radius (μm)	MM FWHM image (μm)	MM FWHM surface (μm)	Spacer (mm)	GRIN (mm)
1	35	737	647	0.570	2.225
2	30	625	544	1.042	1.831
3	25	530	461	1.556	1.511
4	20	428	368	2.228	1.223
5	15	322	274	3.256	0.956
6	10	213	185	5.228	0.703

Figure 4.8 shows the shaded model along with SM and MM ray traces and beam spot sizes as a function of axial position for combination No. 4, which provides a 20-μm SM waist radius, as detailed in Table 4.3. The image plane, located at 7.5 mm from the last optical surface and 7.85 mm from the optical axis, and the tissue surface position, at 7 mm from the optical axis, are also shown. The Gaussian mode has a radius ω, which evolves as a function of z as :

$$\omega(z) = \omega_0 \sqrt{1 + \left(\frac{z}{z_R}\right)^2}, \tag{4.18}$$

with a $1/e^2$ waist radius (ω_0) of 19.42 μm and a Rayleigh range (z_R) of 0.92 mm. In Eq. 4.18, $z = 0$ corresponds to the image plane location. As observed previously when validating the model, the MM FWHM will first decrease to 175 μm then expand to reach a value of ~430 μm at the image plane. For laser marking purposes, the beam spot profile at the tissue surface will dictate the incident radiant exposure such that we will consider that diameter for photo-thermal simulations to be presented in the following Chapter. For this particular configuration, the MM FWHM at the tissue surface is ~370 μm. This smaller diameter implies, for a constant peak power, an increased peak irradiance, critical to reaching coagulation.

Results for all six lens-spacer combinations are summarized in Table 4.3. For this WD, the smallest achievable spot size is limited by the clear aperture of the prism such that a 10-μm SM spot size design (combination No. 6) will suffer from 9% and 42% losses of the SM and MM signals, respectively. The ray trace for this design is presented in Figure 4.9 emphasizing ray leakage at the prism. Using a cylindrical prism could resolve the issue, but an additional cylindrical surface crossed by the beams would induce further astigmatism. A micro-mirror could also be used in lieu of the prism without adding any aberrations. In this case, anti-

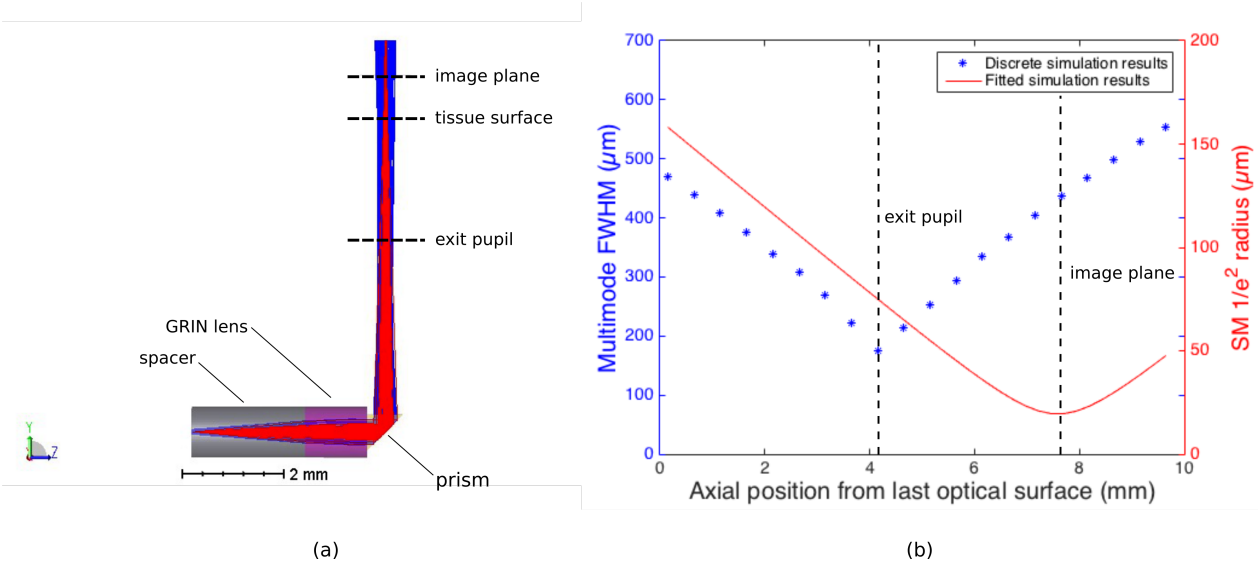

Figure 4.8 Simulation results for combination No. 4. (a) Single GRIN lens-based probe assembly simulated using the non-sequential model. SM (in red) and MM (in blue) rays are overlaid. The image plane, tissue surface, and exit pupil positions are represented by the dashed lines. (b) SM beam spot size radius (fitted using Eq. 4.18) and MM FWHM as a function of axial position with respect to the prism surface.

reflection coating or angle polishing should be considered on the last surface of the GRIN lens to reduce back-reflections.

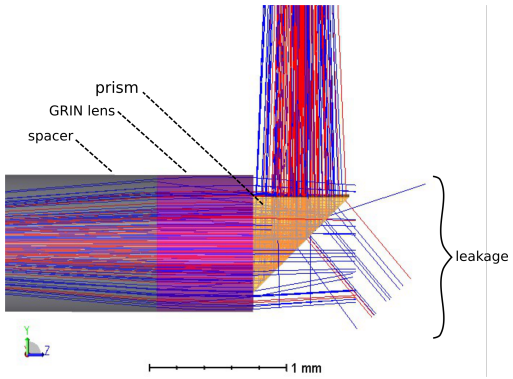

Figure 4.9 Single GRIN lens-based probe assembly simulated using the non-sequential model (combination No. 6) showing the limited clear aperture of the prism leading to rays leakage. SM and MM signals are represented by the red and blue rays, respectively.

Double-lens design

In the single lens design, one can observe that the SM and MM minimal beam diameters do not occur at the same axial position. As explained previously, this is due to the fact that the MM beam corresponds to a partially coherent beam as opposed to the SM beam which is a purely coherent beam. By using a double-lens system, it is possible to modify the location of the MM waist with respect to the SM waist. This concept is demonstrated here using a double spacer-GRIN lens configuration, shown in Figure 4.10, where the spacers and GRIN lenses are made of BK7 glass and SLW-1.0 glass, respectively. The first spacer-GRIN lens pair is optimized to collimate the SM beam, while the second pair focuses the light at a WD of about 7.5 mm. The resulting SM $1/e^2$ radius is 20 μm. In this configuration, the length of the second spacer would not affect the SM beam spot size but will modify the propagation of the MM beam.

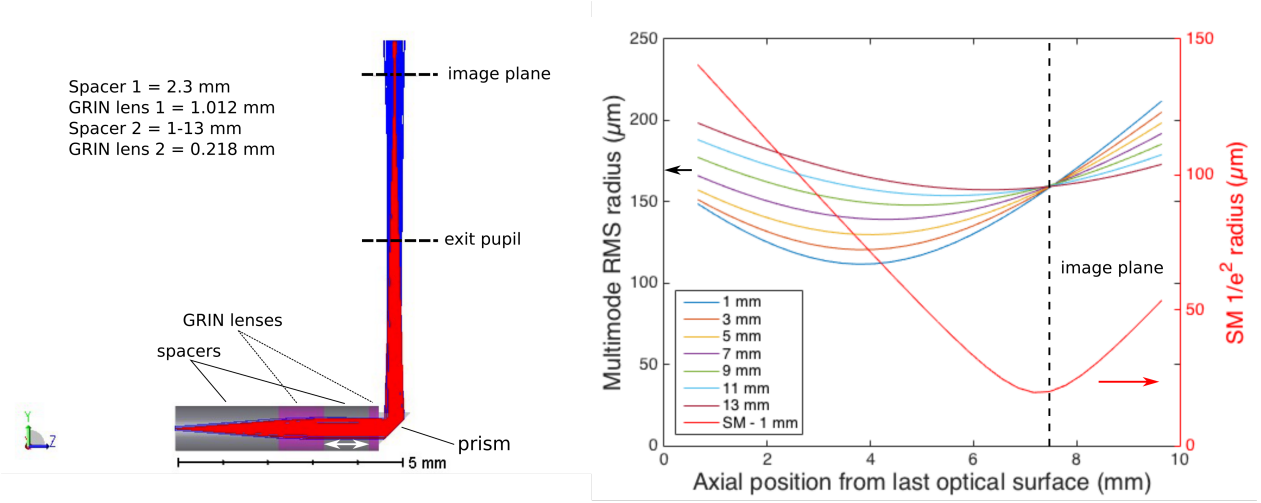

Figure 4.10 Simulation results for the double spacer-GRIN lens configuration. (a) Double GRIN lens-based probe assembly simulated using the non-sequential model. SM and MM signals are represented in red and blue, respectively. The second spacer length (double white arrow) was varied to shift the position of the MM waist location. (b) SM beam spot size radius for a spacer length of 1 mm (in red) and MM RMS radius for different spacer lengths.

Figure 4.10b shows the resulting SM beam radius as a function of axial position (in red) along with results for the MM beam for different lengths for the second spacer. One can observe that, for increasing spacer length (i.e. approaching a 4-f configuration), the MM waist location will shift towards the SM waist location, but the actual MM beam spot size at the image plane will remain constant. In this configuration, the MM RMS radius at the

image plane is ∼160 μm, which corresponds to a FWHM of 450 μm [4].

4.3.2 Reflective designs

The use of a reflective design is another promising option where a mirror is used to focus and deflect the light. With the use of diamond turning or optical grade computer numerical control (CNC) machining tool, it is possible to design reflective aspheric surfaces which could allow the optimization of the SM and MM beams independently. To model the mirror surface, a biconic aspheric surface is used. The equation describing the z-component (i.e. along the optical axis) of the displacement of the surface with respect to the vertex is called the sag equation. Each axis (x and y) of the mirror is described by a radius of curvature (R_x and R_y), a conic factor (k_x and k_y), and 10 aspheric parameters (α and β). The final surface curvature is therefore described by the following sag equation :

$$z(x,y) = \frac{c_x x^2 + c_y y^2}{1 + \sqrt{1 - (1+k_x)c_x^2 x^2 - (1+k_y)c_y^2 y^2}} + \sum_{i=1}^{16} \alpha_i x^i + \sum_{i=1}^{16} \beta_i y^i, \tag{4.19}$$

where $c_x = 1/R_x$ and $c_y = 1/R_y$. Assuming the MM beam takes a larger area on the mirror compared to the SM beam, the outer rim of the mirror could be modified in order to increase its curvature and reduce the MM beam waist without affecting the SM waist. Figure 4.11 shows the normalized aspheric functions from Equation 4.19. One can see that the high-order even aspheric functions can be used to increase the radius of curvature at the edges of the mirror only.

Using a single-lens configuration with a mirror does not provide enough flexibility to independently optimize the SM and MM beam since the area of the mirror illuminated by each channel is not significantly different. Figure 4.12 shows such a configuration with a 1.89-mm long glass spacer and a concave mirror optimized to provide a SM $1/e^2$ radius of 20 μm at a distance of 7.85 mm from the optical axis (Figure 4.12c). In this example, the aspheric functions were optimized to correct spherical aberrations and astigmatism of the SM beam waist. The resulting mirror surface is represented by the sag function represented in Figure 4.12b. The resulting MM FWHM at the image plane is 436 μm therefore providing similar results to an equivalent single GRIN lens probe. Onto the mirror, the MM beam area is only 1.2 times larger than the SM beam spot providing very low freedom to shape them independently.

To increase the area illuminated by the MM beam with respect to the SM beam, a GRIN lens

4. RMS, or root-mean-square, is defined as : $r_{RMS} = \sqrt{\langle r^2 \rangle}$. For a Gaussian profile, the RMS radius is about 72% of the $1/e^2$ radius.

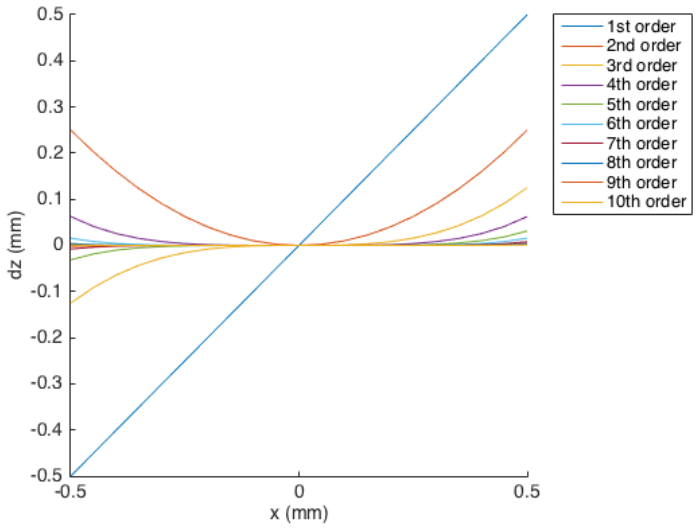

Figure 4.11 Normalized aspheric functions describing the sag equation (Eq. 4.19).

is first used to collimate the SM signal. The GRIN lens-mirror distance can then be adjusted to further optimize the MM beam spot size. Figure 4.13a shows such a configuration where a 2.585-mm long GRIN lens (SLW-1.0 glass) is used in front of a 45° concave mirror. The mirror's x and y radii of curvature are then optimized to focus the SM light at a WD of about 7 mm resulting in a $1/e^2$ waist radius of 20.3 μm. As mentioned previously, using the even high-order aspheric functions, the MM beam spot size can be further shaped independently of the SM beam. In this case, it was found that the 4^{th} and 6^{th} orders allow a significant modification of the MM beam spot with no effect on the SM waist radius and location. Figure 4.13b presents the resulting MM FWHM before and after that optimization for different values of lens-mirror separation. Since the ratio between the SM and MM areas onto the mirror is proportional to the lens-mirror separation, one can see that the correction is greater for larger separation. Figure 4.14 shows the detailed results for a separation of ∼4.5 mm as well as the resulting freeform mirror surface before and after optimization. As expected, the SM propagation shows negligible changes (Figure 4.14b). The surface optimization, for that lens-mirror separation, results in a reduction of about 30% of the MM FWHM. As shown in Figure 4.14c, the optimization results in a deformation of the original MM beam shape, from flat-top to quasi-Gaussian, but shows an increased peak irradiance, which is desirable for laser coagulation.

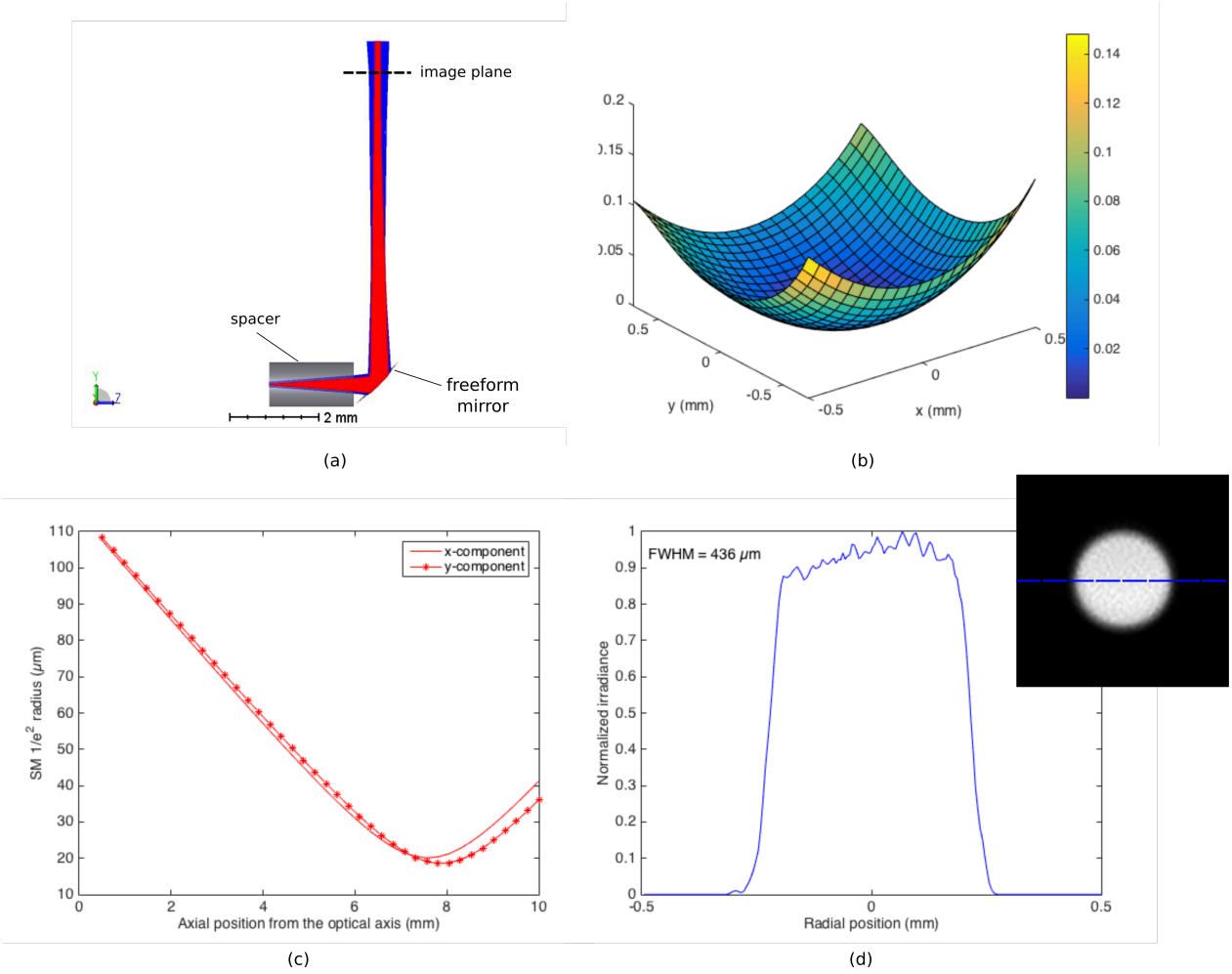

Figure 4.12 Simulation results for a single-lens configuration based on a reflective design : (a) glass spacer and concave mirror assembly, (b) mirror surface after aberrations optimization, (c) x- and y-component of the SM propagation along the axial position, and (d) MM beam spot profile at the image plane.

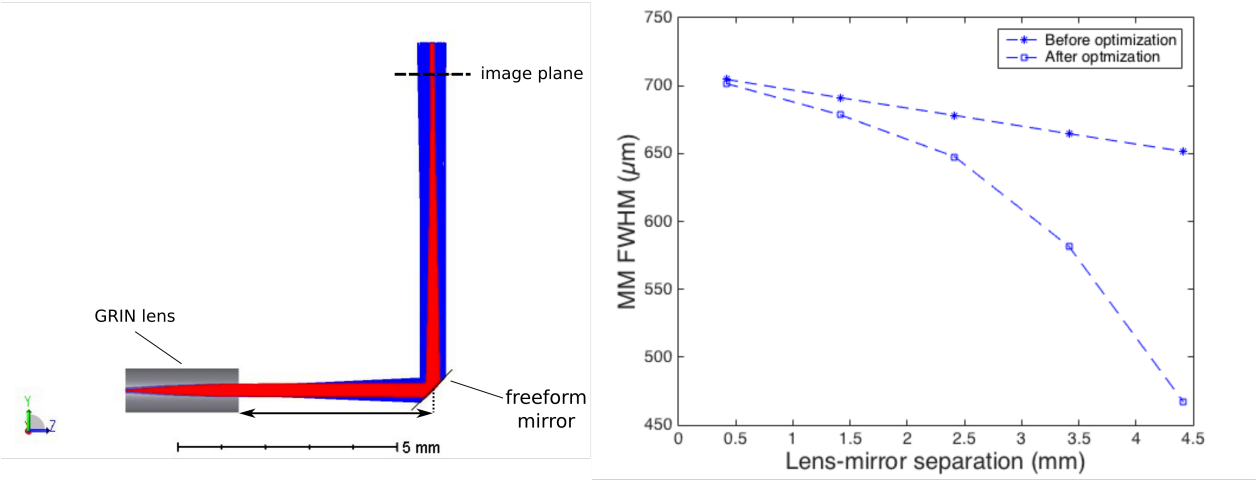

Figure 4.13 Simulation results for the GRIN lens-mirror configuration. (a) GRIN lens-mirror assembly with a lens-mirror separation (indicated by the double arrow) of ∼4.5 mm. (b) MM FWHM before and after the high-order aspheric functions optimization as a function of lens-mirror separation.

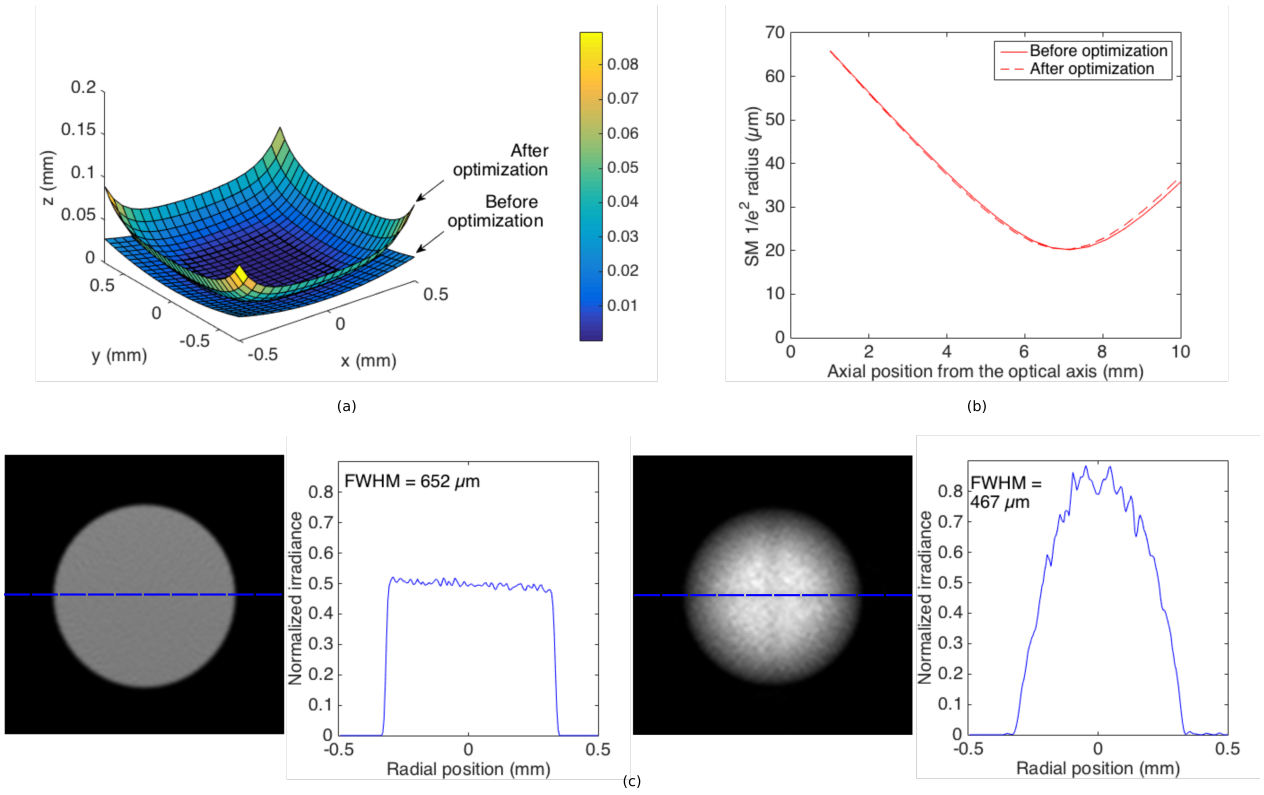

Figure 4.14 Results for a GRIN lens-mirror configuration with a ∼4.5-mm lens-mirror separation before and after the optimization of the high-order aspheric functions : (a) mirror surface, (b) SM propagation along the axial position and (c) MM beam spot profile at the image plane (left : before optimization and right : after optimization).

4.4 Discussion

As mentioned at the beginning of this Chapter, a MM beam will exhibit different propagation characteristics compared to a SM beam due to its partially coherent nature. With the help of the DCF model developed herein, it is possible to assess these differences for various optical systems and optimize the performances accordingly. We indeed demonstrated that our model can successfully predict the MM propagation behaviour taking into account its partially coherent nature. Using the developed model, it was possible to evaluate two different types of design : GRIN lens-based design and reflective design for which different cases were analyzed. We focused our analysis on these specific designs since they respect the specific constraints of GI imaging in terms of size, imaging performances and ease of manufacturing.

For GRIN lens-prism assembly, the MM FWHM at the image plane is fixed by the magnification of the system. Therefore, a lower magnification will result in a smaller beam diameter, but is limited by the clear aperture of the prism. Reducing the system's magnification also means reducing the SM beam diameter, which will provide a better imaging resolution, but will also reduce the Rayleigh length and might therefore reduce the imaging depth range. For a beam with a radius of 15 μm, the depth range (i.e. twice the Rayleigh range) is about 1 mm, which is still suitable for GI imaging.

To study the effect of the position of the exit pupil on the MM FWHM, a double-GRIN lens assembly was simulated. By increasing the lenses separation and getting closer to a 4-f system (Figure 4.10b), the MM beam approaches collimation. However, the FWHM at the image plane is invariant and is actually dictated by the system's magnification as it is the case with the single-lens configuration. Having a quasi-collimated beam presents the advantage of being less sensitive to any decentering of the catheter thus maintaining a constant MM beam diameter on the tissue surface. However, the length of the second spacer required to do so for such long WD results in a distal optics with total length >16 mm (not including the ferrule), which is not compatible with standard hypotube. On the other hand, minimizing the second spacer length allows obtaining a smaller beam spot size at the tissue surface, which will prove beneficial for laser marking purposes. Therefore, a single-lens configuration, assuming that the catheter's centering, and thus the image plane location, can be maintained, seems to be more suitable than a double-lens configuration.

Performances of reflective designs, based on a 45° freeform concave mirror, were also assessed. With new optical grade CNC machining tool or high-resolution 3D printing, it is now possible to envision almost any surface shape which could affect SM and MM beam independently. A simple design based on a spacer and a mirror was first simulated. We first observed that such

a design is prone to more aberrations than a GRIN lens-based design such that the surface needs to be optimized to achieve the best SM beam spot possible. After proper optimization, performances of this design yield results similar to that of the GRIN lens design. However, since the mirror area illuminated by each channel is not significantly different, it is not possible to dramatically reduce the MM beam spot size without affecting the SM propagation.

To increase the area ratio between the SM and MM beams onto the mirror, a GRIN lens was used in front of the mirror to collimate the SM beam. As shown in Figure 4.13 and 4.14, it was possible to reduce the MM beam spot size by up to 30% (with a lens-mirror separation of 4.5 mm) without significantly affecting the SM propagation. However, by looking at MM FWHM before optimization, one can see that it is significantly larger than other equivalent design ($\sim$650 μm versus $\sim$430 μm) such that the final value of $\sim$470 μm does not correspond to a major improvement compared to the spacer-mirror configuration. This is due to the fact that the MM beam is diverging after the GRIN lens as opposed to the other designs.

In general, the use of a GRIN lens-based design is easier to manufacture compared to reflective designs. A reflective design involves an assembly that is far more sensitive to the alignment of the different parts with respect to each other. Proper tolerancing analysis is therefore required to assess the sensitivity of the design to misalignment. Considering all the elements discussed above, a single-GRIN lens-based design provides the best performances in terms of MM FWHM at the tissue surface and respects all the constraints of GI imaging. For a 14-mm balloon-sheath, the minimal MM beam spot size at the tissue surface that can be achieved through a probe is between 275 and 350 μm, which results in an SM $1/e^2$ radius between 15 and 20 μm (Table 4.3). The analyses presented here focus on one balloon size, but most conclusions are readily applicable to larger size. However, the magnification could be further limited such that the minimal beam spot size achievable might be larger than the values stated previously.

CHAPTER 5 TOWARDS ENDOSCOPIC DYNAMIC LASER MARKING

The success of a laser mark is defined by its visibility to the endoscopist's naked eye. We first define a visibility criteria specific to dynamic laser marking based on the coagulation mark's size. Photo-thermal simulations were used to predict the width and depth of the coagulation zone. The simulations took into account the beam size and profile shape (flat-top or Gaussian beam). Laser-specific parameters such as pulse duration and peak power are also considered. Finally, the effect of the scanning speed of the beam over the tissue, dictated by the rotation speed of the probe, is investigated. The photo-thermal model was validated for dynamic laser marking with ex vivo data. Specific requirements to achieve endoscopic dynamic laser marking under the current clinical settings were extracted from photo-thermal simulations. This Chapter also presents the first prototype of an endoscopic dynamic laser marking system along with preliminary ex vivo imaging. The photo-thermal modeling along with preliminary results was presented at *SPIE Photonics West* conference in 2017 in the talk entitled : "Towards double-clad fiber-based endoscopic dynamic laser marking and concurrent optical coherence tomography".

5.1 Visibility criteria

Before simulating photo-thermal effects, it is important to identify the attributes of a visible mark. Such attributes are : 1- presence of clear edges, 2- contrast provided by the coagulation effect, and 3- size of the coagulation spot. Since single-pulse coagulation targets a regime free of heat dissipation, the marks will present clear edges resulting in high contrast with surrounding tissue (as seen in Figure 3.6). Therefore, the only criteria for a visible mark in this regime are whether the coagulation threshold is reached, and the mark is large enough to be seen under videoendoscopy.

In order to determine the minimal size visible using a standard gastroscope, laser marking was performed ex vivo on swine esophageal tissue. Different pulse energy settings were used to produce marks of different sizes. Figure 5.1 shows the resulting coagulation marks as imaged using a conventional gastroscope (EG-2990i with EPK-i video processor, Pentax Medical). It is possible to observe that even the smallest marks ($\sim$140μm) and those located further in the field of view are fully visible. This case is not exactly representative of the reality since several marks are used for each setting, therefore increasing their visibility. However, considering the average size of the marks ($\sim$150 μm) compared to the size of a typical biopsy sample (6-8 mm), one can envision that a few marks on each side of the region-of-interest

could be performed, therefore greatly increasing the visibility. For the following simulation analyses, we define a visible mark as having a diameter >150 μm.

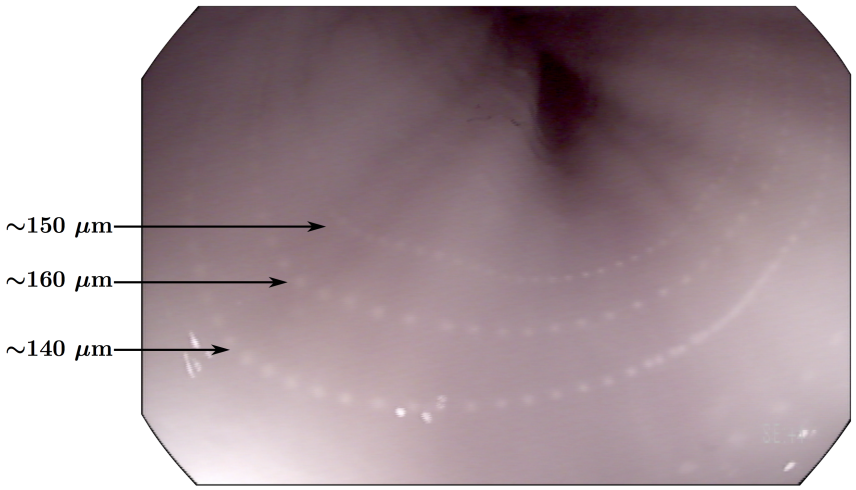

Figure 5.1 Swine esophagus image taken with a standard clinical gastroscope showing coagulation marks with diameters between 140 and 160 μm.

5.2 Photo-thermal modeling

Tissue photo-coagulation is the result of thermal damage initiated by the absorption of light energy within a tissue. Figure 5.2 shows the algorithm used to model light-tissue interactions. The methodology followed here is based on Ref. 25 with slight modifications. Briefly, a Monte Carlo simulation, based on the MCML platform, [110] is first performed to determine the fluence rate as a function of depth for an infinitely narrow beam based on the tissue optical properties (absorption and scattering coefficients as well as anisotropy). Assuming a circular symmetry, the output is interpolated on a three-dimensional grid and convoluted with the specified beam irradiance profile. The beam is assumed to be collimated. The 3D fluence rate map is converted into an absorption map by multiplying with the tissue absorption coefficient, which is then used as the heat source (Q) in a three-dimensional, time-dependent finite-element model (FEM) of the heat diffusion in the tissue. The FEM solves the heat equation, which is governed by :

$$\nabla \cdot \kappa \nabla T + Q = \rho c \frac{\delta T}{\delta t}, \tag{5.1}$$

where T is the temperature volume, κ is the thermal conductivity, ρ is the density, c is the

specific heat and t is time. The top surface is modeled as an air-tissue convective boundary. For all the other surfaces, insulating boundary conditions are assumed. The resulting time-dependent temperature profile is used to calculate tissue thermal damage (i.e. protein denaturation in this case) with the Arrhenius equation as a first-order process [111] :

$$\Omega(x, y, z, \tau) = A \int_0^{\tau} \exp\left(-\frac{E_a}{R \cdot T(x, y, z, t)}\right) dt, \tag{5.2}$$

where A and E_a are the frequency factor (s^{-1}) and the activation energy (J/mol) for denaturation, respectively, R is the universal gas constant (8.31 J/mol·K) and τ is the pulse duration. From the damage integral, we can then compute the fraction of thermally denatured proteins as follows :

$$D(x, y, z) = 1 - \exp\left(-\Omega(x, y, z, \tau)\right). \tag{5.3}$$

We consider the tissue to be fully coagulated for a damage fraction >95% [25]. This fraction threshold was chosen purposely high as a higher fraction of thermally denatured protein is associated with a higher coagulation contrast for marking visibility.

It is also possible to add an iterative loop to the algorithm to take into account dynamic changes in scattering occurring as the tissue coagulates. To do so, we start with a 1-layer uniform sample. At each time step, the coagulation zone depth is computed. If the coagulation zone has progressed, the superficial layer corresponding to this new depth will be replaced by a layer of increased scattering coefficient (μ_s^c). The photon propagation will be re-computed using this new 2-layer configuration. Dynamic changes in scattering were assumed to be important, and the iterative loop was therefore implemented, for slow- or non-scanning beam configurations. Figure 5.2 presents a block diagram showing all the steps involved in the photo-thermal modeling as described above.

5.2.1 Simulation parameters

Table 5.1 shows the optical and thermal properties used to model esophageal epithelium. A refractive index of 1.38 and an anisotropy of 0.9 were assumed. The absorption coefficient was obtained by multiplying the absorption coefficient of water (obtained from Ref. 112) by the water content (about 70% for most biological tissue) [113]. The scattering coefficient was extrapolated from Ref. 114 for a wavelength of 1436 nm. For coagulated tissue, an increased of 300% of the scattering coefficient was assumed which is consistent with observation made for other tissues [115]. Thermal conductivity and specific heat were estimated from data for

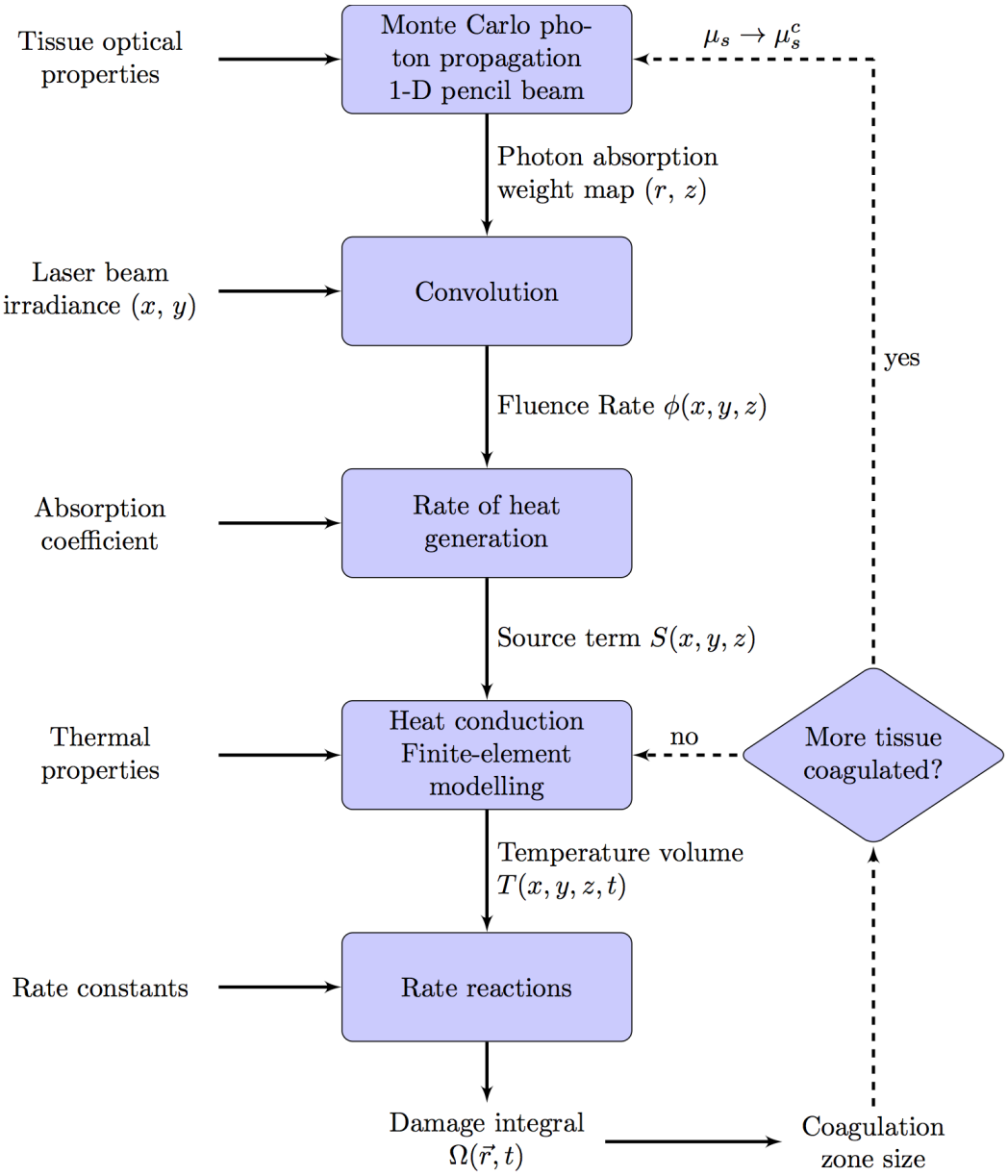

Figure 5.2 Block diagram describing the algorithm used for photo-thermal modeling. The optional iterative loop used for slow- or non-scanning beam configurations is shown using the dashed arrows.

similar tissues [116, 117]. A convective heat transfer coefficient of 500 W/m^{2}K was used to compensate for surface water evaporation [118] since some vaporization was observed during ex vivo experiments.

Table 5.1 Optical (λ = 1436 nm) and thermal properties of esophageal epithelium

Properties		Symbol	Value
Optical	Refractive index	n	1.38
	Absorption coefficient	μ_a	21.9 cm^{-1}
	Scattering coefficient	μ_s	28.2 cm^{-1}
	Coagulated tissue scattering coefficient	μ_s^c	112.8 cm^{-1}
	Anisotropy	g	0.9
Thermal	Thermal conductivity	κ	0.5 W/mK
	Specific heat	c	3.7 J/gK
	Density	ρ	1.05 g/cm^{-3}
	Convective heat transfer coefficient	h	500 W/m^{2}K

Table 5.2 presents the parameters used for the Monte Carlo algorithm for all simulations unless otherwise stated. These values were set to optimize the resolution of the photon weight map while limiting the size of the output, and therefore minimizing the computational time.

Table 5.2 Monte Carlo simulation parameters

Parameter	Symbol	Value
Number of photons	N	5 x 10^6 photons
Step size in z	dz	3 μm
Number of steps in z	Nz	1170
Step size in x, y	dr	3.5 μm
Number of steps in x, y	Nr	250
Number of angular steps	Na	30

Mesh size and resolutions used for the FEM are presented in Table 5.3. The temporal step size was adjusted to optimize the resolution versus computation time required for each specific simulation. Step sizes also needed to respect the stability criteria, given by :

$$\zeta = \alpha \frac{dt}{Dr^2} > 1/6, \tag{5.4}$$

where $\alpha = \frac{\kappa}{\rho c}$. The tissue size was chosen to avoid any boundary effects (except for the top surface) to affect the temperature solution.

In addition to these parameters, it is possible to set the period and the pulse width of the laser as well as the speed at which the temperature solution is translated with respect to the

heat source. The solution is calculated for a normalized power of 1 W and scaled afterwards using the given peak power.

Table 5.3 FEM simulation parameters

Parameter	Symbol	Value
Step size in z	Dz	6 μm
Depth (z)	Z	7 mm
Step size in x, y	Dr	7 μm
Size (x, y)	X or Y	1.8 x 1.8 mm
Step size in t	Dt	1-10 μs

5.2.2 Ex vivo validation

To validate the results given by the photo-thermal model, a benchtop system (as shown on Figure 5.3) was used for single-pulse laser marking on swine esophageal tissue. A pulsed RFL at 1436 nm, described in Ref. 41, was used as the marking laser. To inject the marking laser into the inner cladding of the DCF and allow concurrent OCT into the core, a DCFC (Castor Optics, DC1300LJ, prototype version), based on a design similar to the one reported in Chapter 3, was used. In this iteration of the injection coupler, a MMF (MM-S105/125-12A, Nufern) was used as the injection fiber and a standard DCF (SM-9/105/125-20A, Nufern) was used as the imaging fiber. Coupling ratios for the core (∼1250-1350 nm) and cladding (1436 nm) signals are >96% and ∼70%, respectively. OCT data were acquired simultaneously to laser marking using a polygon-based swept-source system centered at 1320 nm [106]. The imaging arm comprises a collimator (f = 6.2mm), a set of galvanometer-mounted mirrors and a scanning lens (10X - LSM02, Thorlabs). To ensure that each pulse hits the tissue at a distinct locations, the tissue was mounted inside-out on a shaft attached to a rotational motor (2342S012CR coreless DC motor with MCDC3006S driver, Faulhaber).

To assess the coagulation zone dimensions, each sample was imaged under a white light microscope (BX43, Olympus) with a 4X objective lens, and the hyper-scattering regions were measured using ImageJ. A subset of samples was additionally processed for histology to evaluate the shape and depth of the coagulation zone. Tissue were trimmed and sectioned for routine nitroblue tetrazolium chloride (NBTC) with eosin counterstain histology after embedding in optimum cutting temperature compound for 10-μm thick frozen section. NBTC stains positive for the thermolabile enzyme lactate dehydrogenase (LDH). Loss of LDH activity ensues rapidly upon heat-induced cell damage such that thermally damaged tissue will exhibit a lack of NBTC [119].

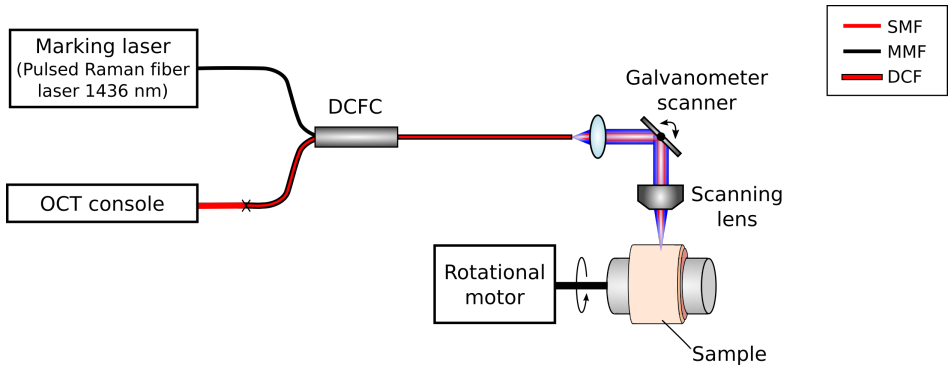

Figure 5.3 Experimental setup used for ex vivo single-pulse laser marking.

Simulation parameters

The MM beam profile evolves as it propagates, which will affect the 3D shape of the optical zone volume and will differ from the simulated collimated beam. The experimental beam profile was thus characterized at the tissue surface and at different depths along the propagation axis using a CCD camera (WinCamD, Data Ray Inc.). Figure 5.4 shows resulting beam profiles at different depths using the 10X scanning lens. At the focal plane, the beam is described by a flat-top profile, as expected, with a FWHM of ~275 μm (Figure 5.4a). As the beam propagates, the profile is going to evolve such that, at 100 μm after the focal plane, the beam is characterized by a quasi-Gaussian profile with a FWHM of 155 μm (Figure 5.4b). To take this effect into account, two cases were simulated : 1- a flat-top beam with FWHM of 275 μm, corresponding to profile shown in Figure 5.4a, and 2- a Gaussian profile with a $1/e^2$ radius of 170 μm (corresponding to a FWHM of 200 μm). The latter case corresponds to a mid-point between profiles shown in Figure 5.4a and b.

A constant peak power of 16.4 W with pulse widths ranging from 100 to 910 μs (resulting in pulse energies up to 15 mJ) is used to reflect experimental conditions. The tissue was assumed to be at room temperature (~20°C).

Validation results

Figure 5.5a shows the resulting laser marks imaged using the white light microscope. Series of marks at different pulse energies were created at different locations along the sample. These images were used to measure the coagulation mark widths for each laser setting. Figure 5.5b shows an example of a histological slide compared with its corresponding OCT image. NBTC stains negative for thermal damage such that coagulation marks correspond

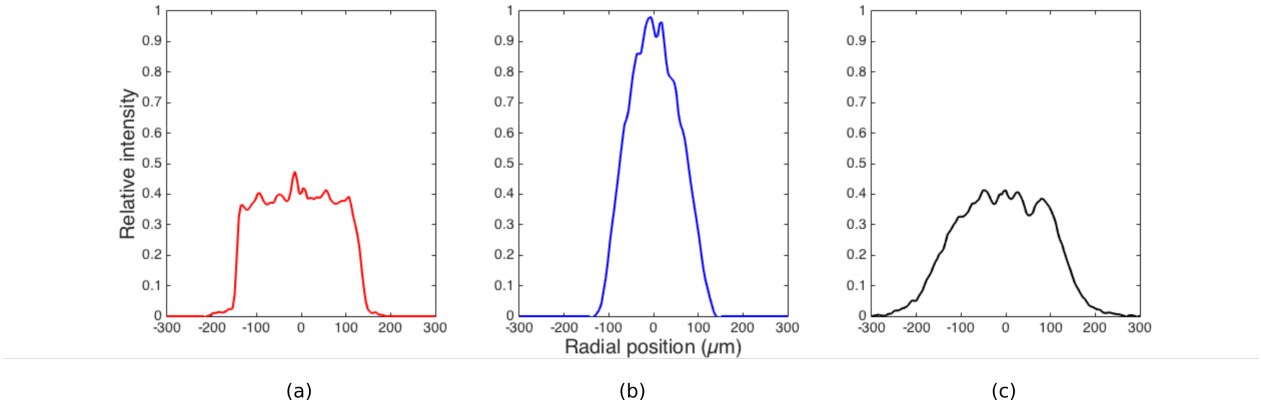

Figure 5.4 Beam profile characterization of the experimental setup (a) at the focal plane, (b) 100 μm and (c) 300 μm away from the focal plane. FWHMs are about 275, 155 and 270 μm, respectively.

to the pinkish regions corresponding to a lack of the blue NBTC stain. On the OCT image, as seen previously, the coagulation marks correspond to the high-scattering regions creating a shadow over underlying structures.

Figure 5.6a presents the results from both simulated cases compared to experimental results and shows the coagulation zone size as a function of pulse energy. For the flat-top beam (red curves), the coagulation threshold is reached for about 6.5 mJ. Once the threshold is reached, the diameter, corresponding to the beam width, stays constant with increasing pulse energy, which is consistent with the fact that no heat diffusion is observed in this regime. The depth of injury increases as a function of pulse energy following an exponential curve.

For the Gaussian profile (blue curves), both the coagulation zone diameter and depth increase as a function of pulse energy. The increase in diameter is due to the fact that, with increasing pulse energy, a larger fraction of the profile will have a radiant exposure above the coagulation threshold. Since the actual optical zone will correspond to a combination of both profiles, the experimental results are expected to fall in between these curves (shaded area). From these results, it is possible to show that a radiant exposure >110 mJ/mm^2 is required to achieve coagulation of esophageal tissue in ex vivo conditions.

Figure 5.6b shows a typical laser mark observed on a histological slide where the coagulated zone is clearly demarcated by the lack of blue NBTC staining. The shape of the coagulation zone appears to reflect the beam profile variation along depth. Indeed, the superficial portion of the coagulated zone appears rectangular, consistent with a flat-top beam, whereas, deeper, the mark shows a shape consistent with a Gaussian profile. Annotations show how diameter

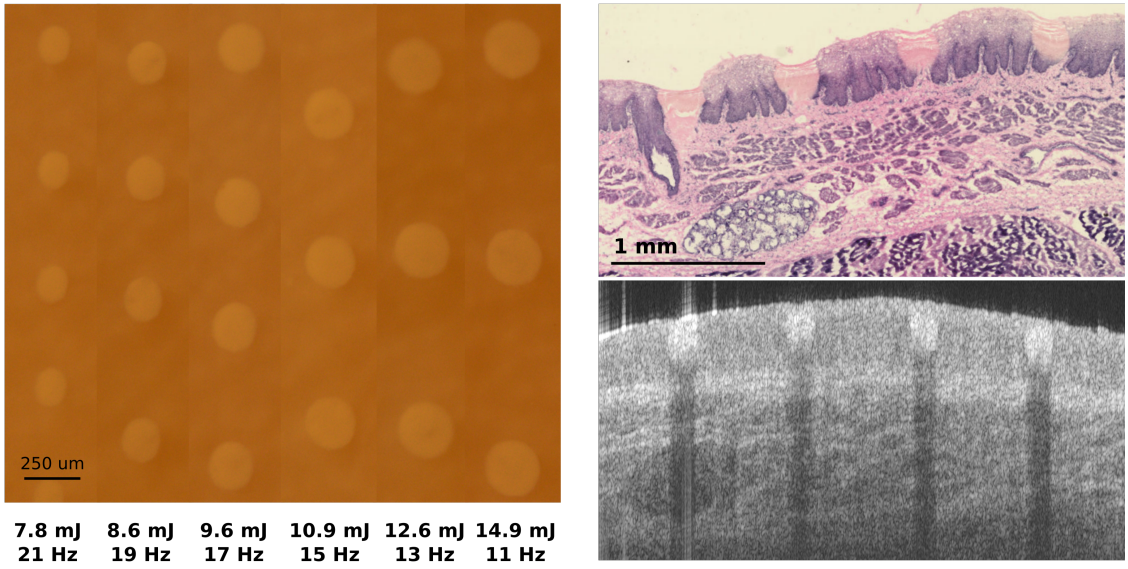

Figure 5.5 Laser marking results. (a) White light microscope images (4X) showing coagulation marks at different pulse energies (using different repetition rates at a constant duty cycle) and (b) histological section compared to its corresponding OCT image showing coagulation marks achieved using a pulse energy of 14.9 mJ.

and depth measurements were taken. The depth was measured in the center of the mark, from the surface to the end of the NBTC-free region. For the diameter, an average of the superficial width of the mark (segmentation shown in red) and the largest width within the tissue was taken to mitigate the effect of tissue deformation due to the microtome as well as from dehydration and shrinkage. Experimental results, both from microscope (black dots) and histology (purple diamonds), correspond to the simulation results. The contribution of the Gaussian profile is clearly seen as the diameter of the marks increases as a function of pulse energy. For the depth of injury, experimental results are explained better by a flat-top beam, although the model appears to slightly overestimate the coagulated depth. This can be explained by the fact that the model assumes a pencil beam such that the effect of the divergence of the beam with depth is not considered. Overall, the model successfully predicted the coagulation threshold as well as the diameter of the mark, which are the important parameters defining the marking visibility.

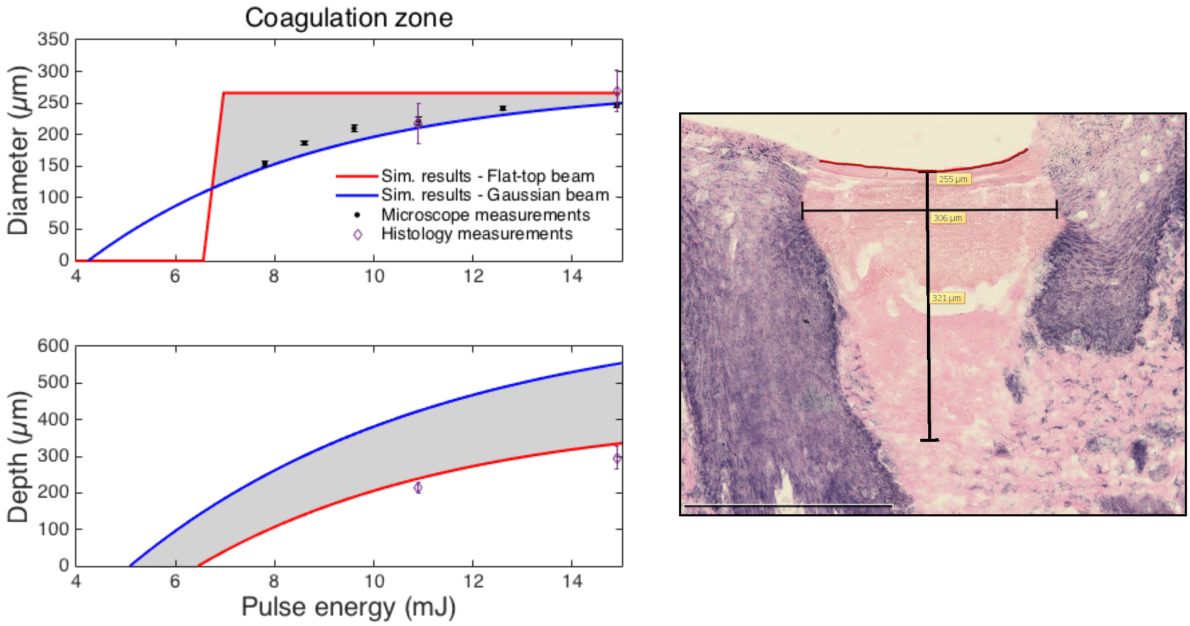

Figure 5.6 Results from the photo-thermal simulation compared to ex vivo measurements using microscope images and histological slides. (a) Coagulation diameter (top) and depth (bottom) as a function of pulse energy. Error bars correspond to the standard deviation (n=4). Inset in (b) shows a histological slide of a typical laser mark produced at ∼15 mJ with measurement annotations. The red line shows the manual segmentation of the coagulation zone at the surface. Scale bar = 250 μm.

5.2.3 Simulation results for a scanning beam

The coagulation threshold presented in the previous section corresponds to the case where the tissue is at room temperature, which is consistent with ex vivo experimental conditions. For in vivo setting, however, we can assume that the tissue will initially be at 37°C, therefore requiring less energy to reach the protein denaturation temperature (>60°C). To compute the in vivo coagulation threshold, a non-scanning configuration was used with a flat-top beam of 400 μm in diameter. Resulting coagulation zone diameter and depth as a function of pulse energy are shown in Figure 5.7. The coagulation threshold is reached at a pulse energy of 9.7 mJ resulting in a radiant exposure of 77 mJ/mm^2. As expected, this threshold is lower than the ex vivo case.

In a clinical setting, the beam is also going to be swept over the tissue at a rather high tangential speed. Because of that, the effective radiant exposure resulting from the beam scanning is to be taken into account. For example, for a 14-mm balloon and an imaging rate

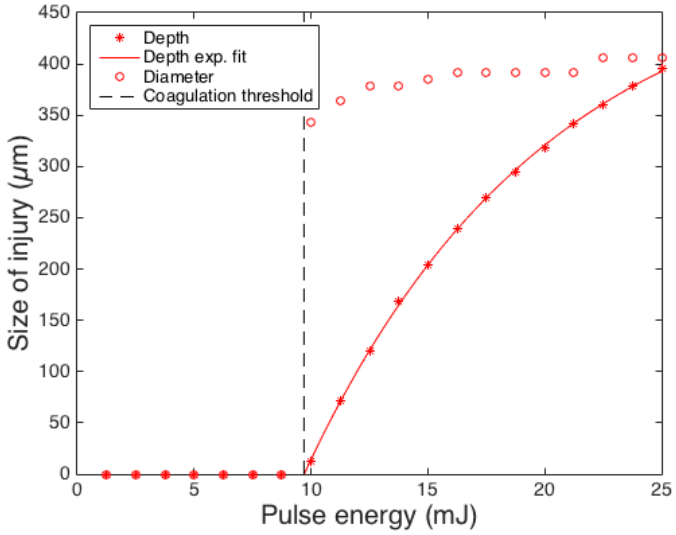

Figure 5.7 Coagulation diameter and depth as a function of pulse energy for a 400-μm diameter beam. The coagulation threshold is indicated by the dashed black line. Tissue initial temperature is set to 37°C.

of 13 frames/second, the tangential component of the speed is about 570 mm/s. This case was simulated using the photo-thermal algorithm for different beam spot sizes, pulse energies and widths. Since the laser beam is scanned over the tissue during the irradiation, dynamic scattering changes were not considered here. To represent in vivo settings, the initial tissue temperature was assumed to be 37°C.

Figure 5.8 shows the effective radiant exposure and fraction of thermal injury resulting from a 20-W peak power illumination with a 400-μm diameter beam with increasing pulse duration and, therefore, increasing pulse energy. For short pulse duration ($\leq$400 μs), one can see that the peak radiant exposure is below the threshold such that the fully coagulated state ($D > 0.95$) is not reached. For that power and speed combination, a pulse energy of at least 10 mJ is required for full coagulation resulting in a mark size of 266 μm x 119 μm, the latter dimension being along the scanning axis (X). Once the threshold is reached, a longer pulse results in an elongated mark as seen for pulse duration of 600 and 700 μs. These results show that, knowing the coagulation threshold, it is possible to use the estimation of the effective radiant exposure to assess the coagulated mark's dimensions.

Figure 5.9a shows the minimal pulse energy required to achieve a mark width of at least 150 μm (our visibility criteria) for different beam spot diameters and pulse widths for each axis. Because of the beam scanning, the mark would not necessarily be symmetrical. For example, for the case of a 200-μm beam spot size, for pulse widths <400 μs, a greater energy

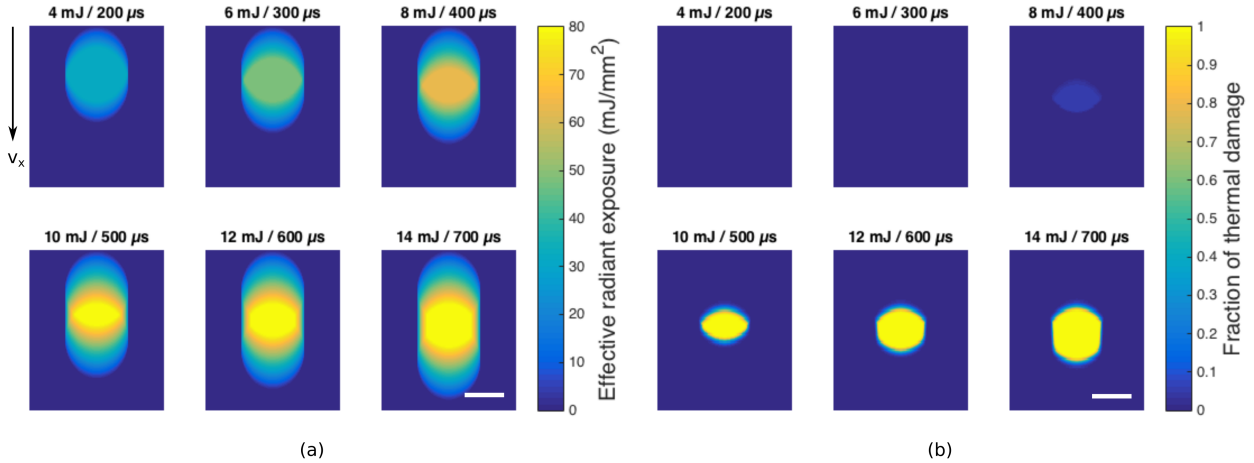

Figure 5.8 Coagulation results for in vivo conditions using a 400-μm diameter beam and a 20-W illumination showing (a) effective radiant exposure and (b) fraction of thermal damage for different pulse widths for the superficial X-Y plane. The scanning direction is indicated by the arrow. Scale bars = 250 μm.

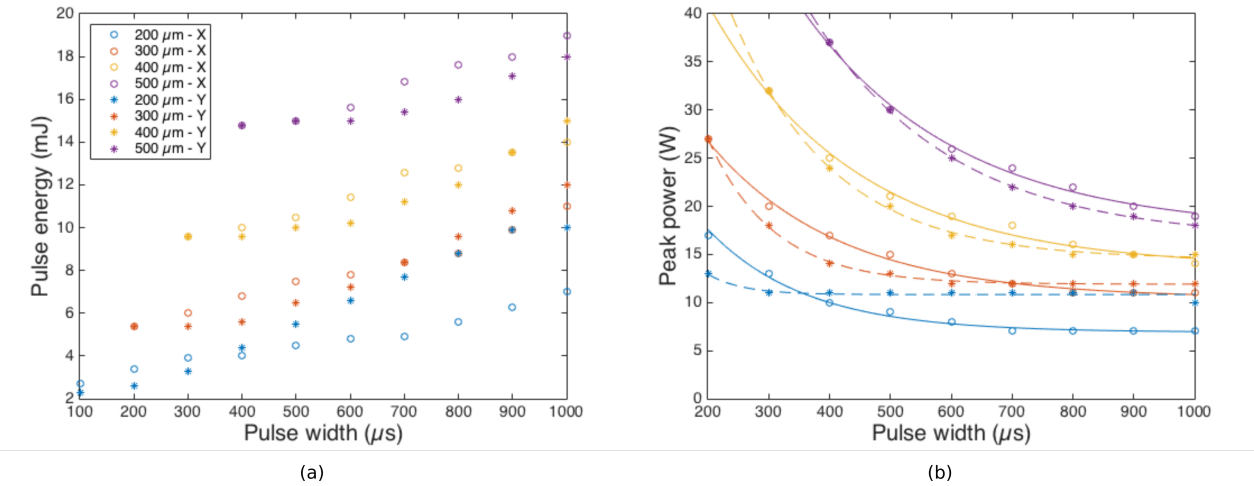

Figure 5.9 Minimal (a) pulse energy and (b) peak power required to achieve a mark width >150 μm as a function of pulse width for different beam diameters for in vivo conditions (T_i = 37°C, speed = 570 mm/s). Solid and dashed lines represent exponential fits for the X and Y directions, respectively. X : along the scanning direction and Y : longitudinal direction.

is needed to achieve the required mark width in the scanning direction (X) as opposed to the longitudinal direction (Y) since the translation of the beam is limited. For longer pulses on the other hand, achieving the required mark width in the Y-direction will require more energy than for the X-direction. This phenomenon can be seen for all beam sizes. Figure 5.9b shows the same results, but in terms of peak power, which were fitted using exponential relations. Different exponential fits are obtained for each direction with a more prominent discrepancy for a small beam spot size. One can observe that, as the pulse width increases, the required peak power plateaued to a constant value.

As shown above, given the coagulation threshold and the effective radiant exposure on the tissue, it is possible to estimate the size of the resulting coagulation mark. This strategy was used to assess marking dimensions for different speed settings. Since the cost of a high-power laser source will be greatly affected by its maximum peak power, reducing the rotation speed of the catheter during the marking procedure could be used to limit the required power. Here, we provide a case study for a 14-mm balloon and a 400-μm diameter beam for speeds corresponding to 4, 8 and 12 rotations/s, which results are presented in Figure 5.10. One can observed that, for short pulse duration (<500 μs), reducing the speed would not affect the minimal power required and a constant pulse energy is required for all speed settings. For longer pulse duration, for which the total displacement of the beam at different speeds will differ more significantly, reducing the speed will result in a lower minimal peak power required to achieve a visible mark. A reduction of 15 and 30% of the required peak power is observed for speeds of 8 and 4 rotations/s, respectively, compared to 12 rotations/s.

5.2.4 Photo-coagulation using other wavelengths

The analyses presented so far were based on a 1436-nm wavelength, which corresponds to one of the absorption peaks of water. This wavelength is also close to the 1310-nm central wavelength of the swept laser source used for OCT imaging therefore avoiding chromatic effects as it propagates through the optical components of the system. However, multimode laser sources at this specific wavelength are rather uncommon since there is no gain medium available to directly generate that wavelength. Therefore, we also investigated the use of 1890 and 1940-nm laser sources for dynamic laser marking. Table 5.4 presents optical properties of esophageal epithelium for these wavelengths. Absorption and scattering coefficients were determined using the same methodology as described in Section 5.2.1.

Figure 5.11 presents the results of non-scanning beam simulations for each of these wavelengths. Coagulation thresholds for 1890 and 1940 nm are ∼40 and ∼20 mJ/mm^2, respectively. As expected, the higher the absorption coefficient, the lower the coagulation threshold

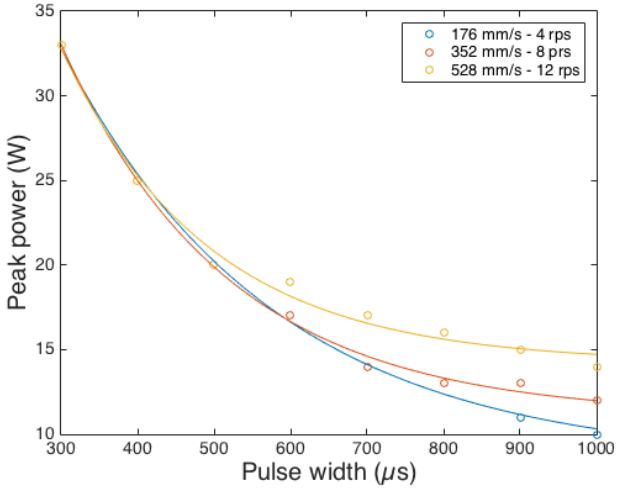

Figure 5.10 Minimal peak power required to achieve a mark width >150 μm (in the scanning direction) as a function of pulse width for different scanning speeds for in vivo conditions ($T_i = 37°C$). Solid lines represent exponential fits.

Table 5.4 Optical properties of esophageal epithelium for different wavelengths

Properties	Symbol	1890 nm	1940 nm
Refractive index	n	1.38	
Absorption coefficient	μ_a	43.0 cm^{-1}	86.5 cm^{-1}
Scattering coefficient	μ_s	20.9 cm^{-1}	20.3 cm^{-1}
Coagulated tissue scattering coefficient	μ_s^c	83.6 cm^{-1}	81.2 cm^{-1}
Anisotropy	g	0.9	

will be. Interestingly, the depth of injury seems to plateau at a lower value for 1940 nm compared to the cases for 1436 and 1890 nm. This can be explained by the changes in scattering coefficient occurring during the coagulation, which limits the penetration depth of the light source. Based on these thresholds, it is possible to determine the minimal power requirements to get a visible mark for a scanning beam configuration as shown in Figure 5.12 for all three different wavelengths. In addition to requiring less power to get a visible mark, the discrepancy between both axis (scanning versus non-scanning axes) is reduced.

Even though lower power is required for longer wavelength, transmission within the system will be affected. Indeed, the absorption in the fiber itself will be higher (see Figure 2.4b) and loss of transmission due to chromatic aberrations within the different optical components will be observed. Therefore, the transmission penalty needs to be taken into consideration when choosing a marking laser and a complete photon budget analysis is required.

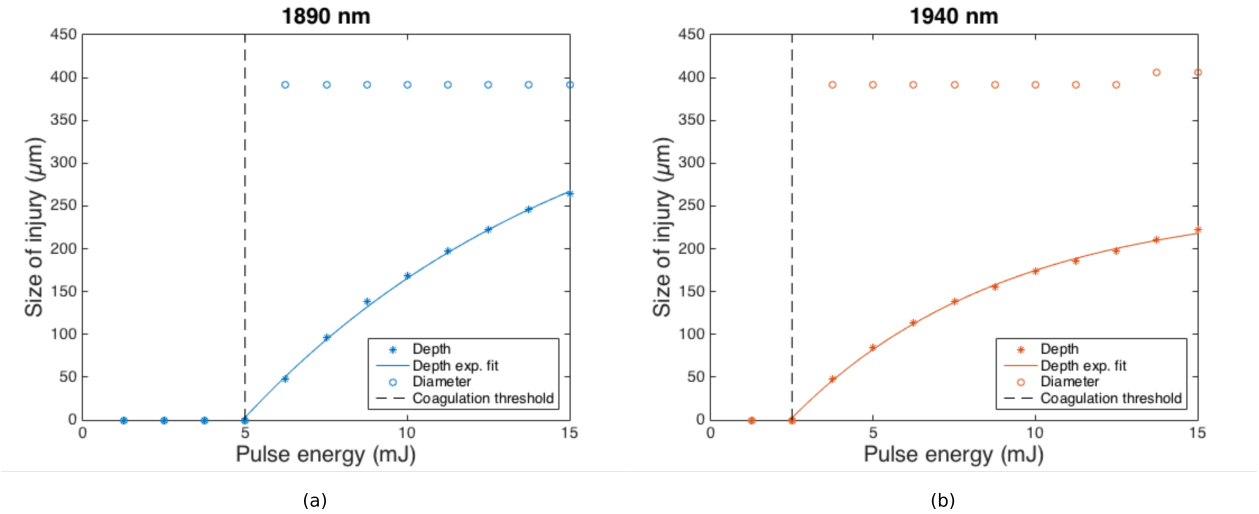

Figure 5.11 Coagulation diameter and depth as a function of pulse energy for a 400-μm diameter beam at (a) 1890 and (b) 1940 nm. Coagulation thresholds are indicated by the dashed black lines. $T_i = 37°$C.

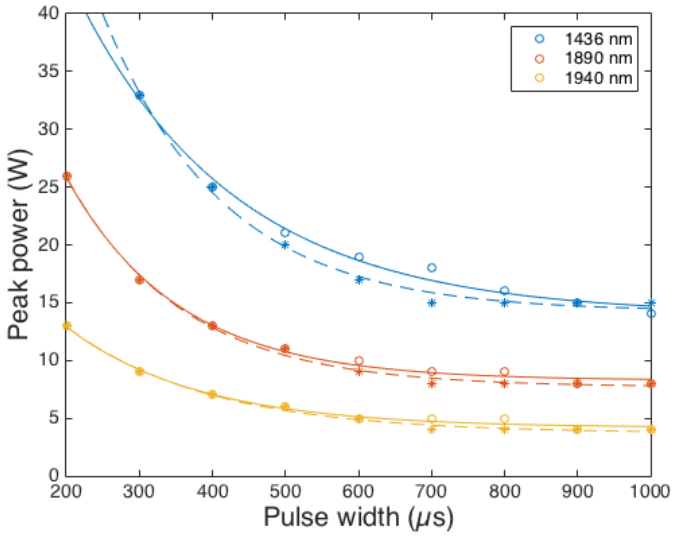

Figure 5.12 Minimal peak power required to achieve a mark width >150 μm as a function of pulse width for different wavelengths for in vivo conditions ($T_i = 37°$C, speed = 570 mm/s). Solid and dashed lines represent exponential fits for the X and Y directions, respectively. X : along the scanning direction and Y : longitudinal direction.

5.3 Endoscopic dynamic laser marking system prototype

In order to evaluate each DCF-based components and decide on a final design for the endoscopic dynamic laser marking system, a system prototype was built and tested. The system prototype, as shown in Figure 5.13, consists of a DCFC, a DCF-based RJ and a balloon-catheter containing a DCF probe. These components were incorporated into a commercial GI OCT system (NVisionVLE, Gen. 1, NinePoint Medical). The marking laser and OCT signal were combined using the DCFC described earlier (Castor Optics, DC1300LJ, prototype version). To assess the imaging quality, DCF-based OCT catheters, compatible with the clinical system, were used. For this prototype, catheters were built according to the commercial specifications providing a SM beam waist diameter between 60 and 70 μm at a working distance of $\sim$9.5 mm, for use with a 17-mm diameter balloon-sheath. As seen in Chapter 4, such a design would provide a MM beam spot diameter of the order of 700 μm at the image plane.

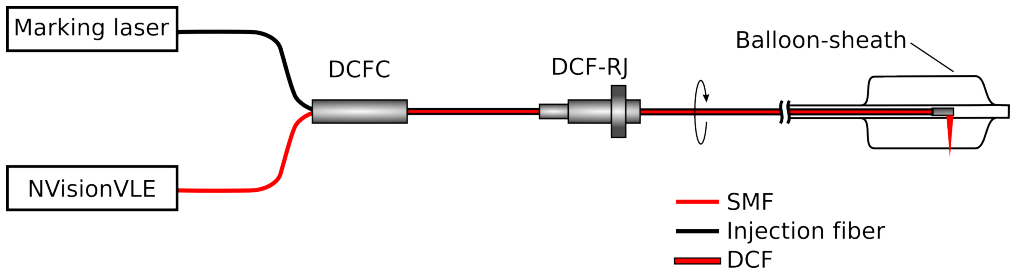

Figure 5.13 Schematic of the DCF-based clinical system prototype.

5.3.1 DCF-based rotary junction

To couple both signals into the spinning catheter, a DCF-RJ was added to the system. Two different models were evaluated to assess 1- the high-power transmission through the inner cladding, and 2- the level of crosstalk-induced artifacts. Both models were manufactured by Princetel, Inc. using the provided DCF (DC1300, Thorlabs). The first model (RPT) tested is based on an index-matching fluid design, therefore minimizing the spacing between the fixed and rotating assemblies. The second model (MJPP) consists of a collimator-based design that is not fluid filled. This model can achieve higher performances in terms of return and insertion losses, thus corresponding to the typical choice for OCT systems. Table 5.5 shows the specifications for both models [120].

Figure 5.14 presents the transmission and insertion loss of a high-power laser (20-W peak power pulsed Raman fiber laser at 1436 nm) through the MM channel of the RJ. A DCFC

Table 5.5 Specifications for the RPT and MJPP rotary junctions

Parameter	RPT	MJPP
Wavelength range	650-1650 nm	1310, 1550 nm, or both
Insertion loss	<2 dB	<2 dB (<1 dB typical)
Return loss	>40 dB	>60 dB

was used to ensure the injection of the high-power laser within the inner cladding. The RPT model shows higher performances with an insertion loss of 0.6 dB for the highest power setting tested compared to almost 1.2 dB for the MJPP model. As mentioned above, the fluid-based design minimizes the spacing between the optical elements, therefore limiting the divergence of the MM beam. None of these models suffered from thermal damage when using the maximum available power (i.e. 1-ms pulses at 20 W peak power).

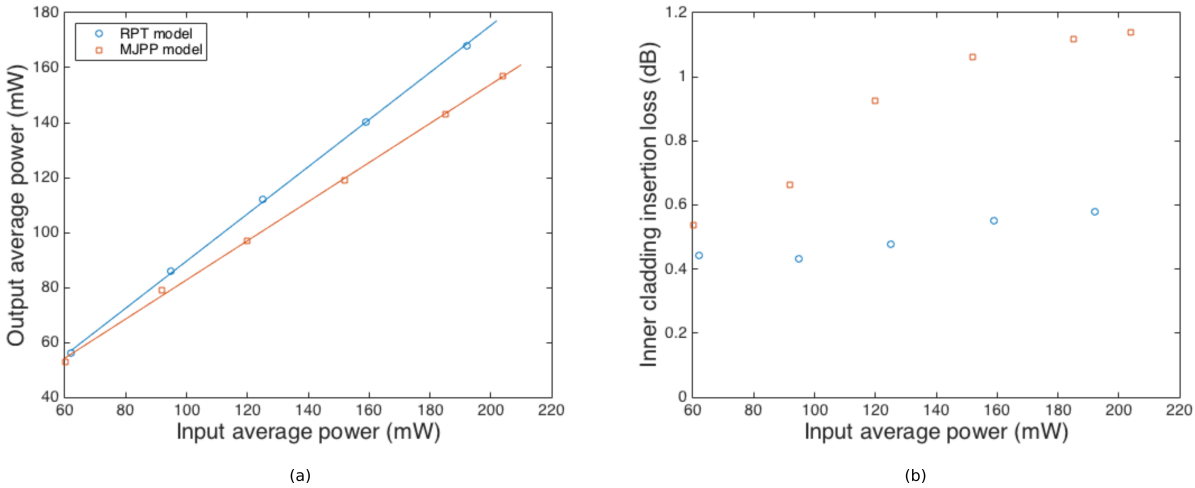

Figure 5.14 DCF inner cladding high-power (a) transmission and (b) insertion loss for two different DCF-RJ models.

Figure 5.15 shows the results of the artifact assessment performed for each RJ model compared to an SMF patchcord. A fibered attenuator was included in the imaging arm to avoid saturation and provide an even signal intensity for each case. M-modes (Figure 5.15a) are shown for each case where the arrow defines the mirror position and curly brackets show the regions used for the sensitivity analysis. Qualitatively, the MJPP model shows very limited crosstalk-induced artifacts compared to the RPT model. To quantitatively assess the sensitivity loss associated with each RJ, signal and artifact levels are defined as the maximum intensity in the regions identified by the arrow and curly brackets, respectively, and averaged over all A-lines of the M-mode image. Signal and artifact levels were measured for different

axial locations within the field of view. Results are presented in Figure 5.15b. The RPT model shows an increase in noise level of up to 16 dB compared to 7 dB for the MJPP model. These artifact levels are higher than for the DCFC setup shown in Chapter 3 for a similar signal intensity level. It can therefore be expected that the DCF-based RJ will be the main contributor of crosstalk-induced artifacts in a DCF imaging setup.

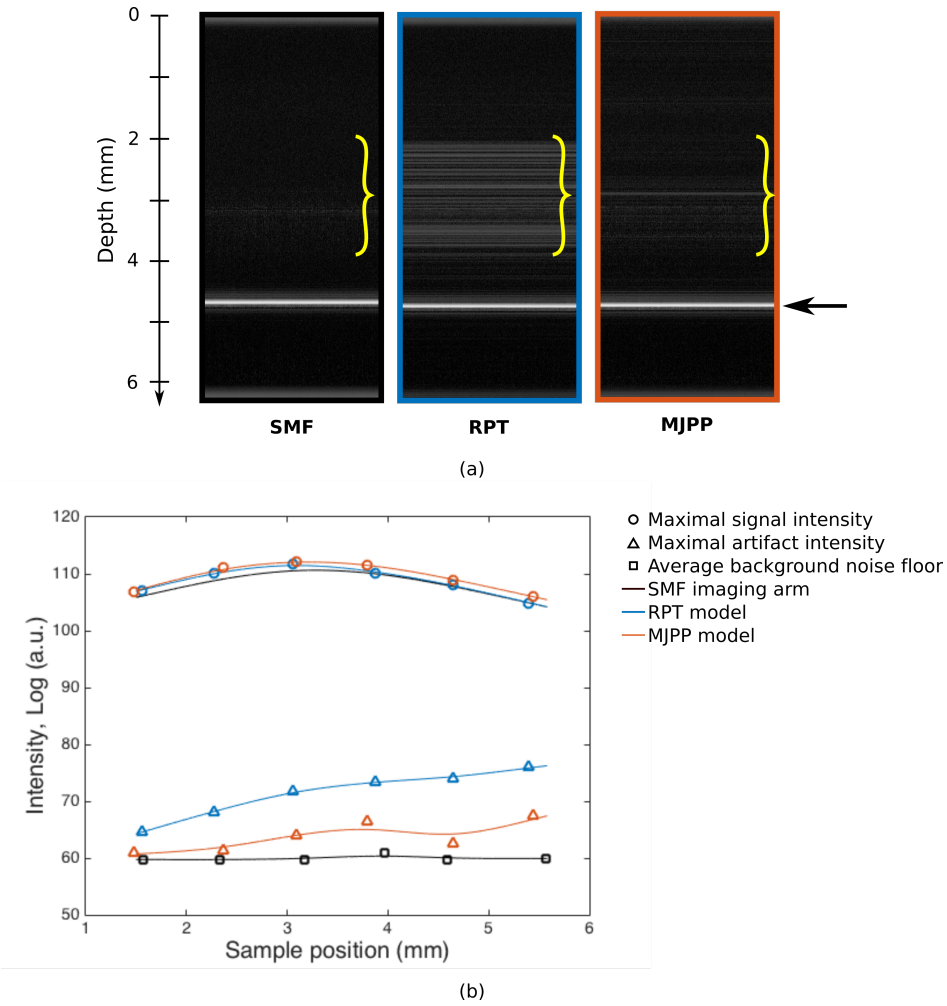

Figure 5.15 DCF inner cladding artifacts characterization for each RJ model compared to an SMF imaging arm. (a) OCT M-mode images of a mirror using an SMF imaging arm compared to both DCF-RJ (RPT or MJPP). Black arrow indicates the position of the mirror while the curly brackets highlight the regions used for artifact assessment. (b) Signal (upper curves) and noise (lower curves) levels for different positions of the sample for each case. Solid lines were obtained using a spline interpolation.

Even though the MM transmission of the RPT model is superior to that of the MJPP model, ensuring a good imaging quality is critical, such that the MJPP model was selected for the DCF-based GI imaging system. Table 5.6 summarizes the characterization of each DCF

component included in the system prototype.

Table 5.6 Characterization of the DCF-based laser marking system prototype

Component	Core insertion loss (1310 nm)	High-power MM transmission (1436 nm)
DCFC	<0.2 dB	∼70%
DCF-RJ (MJPP)	∼0.5 dB	∼77%
DCF catheter	∼0.5 dB	∼80%

5.3.2 Preliminary ex vivo imaging

Figure 5.16 presents the imaging results acquired with the prototype system. To assess the imaging quality, images of fingers wrapped around the balloon were first acquired with an SMF-based imaging arm (Figure 5.16a) and compared to those acquired with the DCF-based system (Figure 5.16b). Both configurations used the Ninepoint Medical Gen. 1 imaging console. Qualitatively, one can observe that the imaging quality in terms of resolution and imaging depth is similar between both configurations.

Ex vivo imaging of a swine esophagus, shown in Figure 5.16c, was performed using the DCF-based system prototype. Typical layered structure of healthy squamous epithelium – epithelium, lamina propria and muscularis mucosae – can be observed. A slight decrease in signal intensity can be observed in the right lower quadrant due to the catheter's sheath being decentered within the inflated balloon. In the same region, a slight increase in background noise, appearing at a shallower depth than the sample, can be observed (highlighted by the red bar) corresponding to crosstalk-induced artifacts. Such ghost artifacts are created due to crosstalk between the core and the inner cladding channels of the DCF occurring at the different connection sites of the system (i.e. connectors, splices, RJ and DCFC). However, the system was optimized to minimize the intensity level of any artifacts in addition to ensuring that fiber lengths between every connection sites are long enough, when possible, to avoid overlapping of these artifacts with tissue signal. In such way, any residual ghost images can be masked to avoid confusion for the clinician.

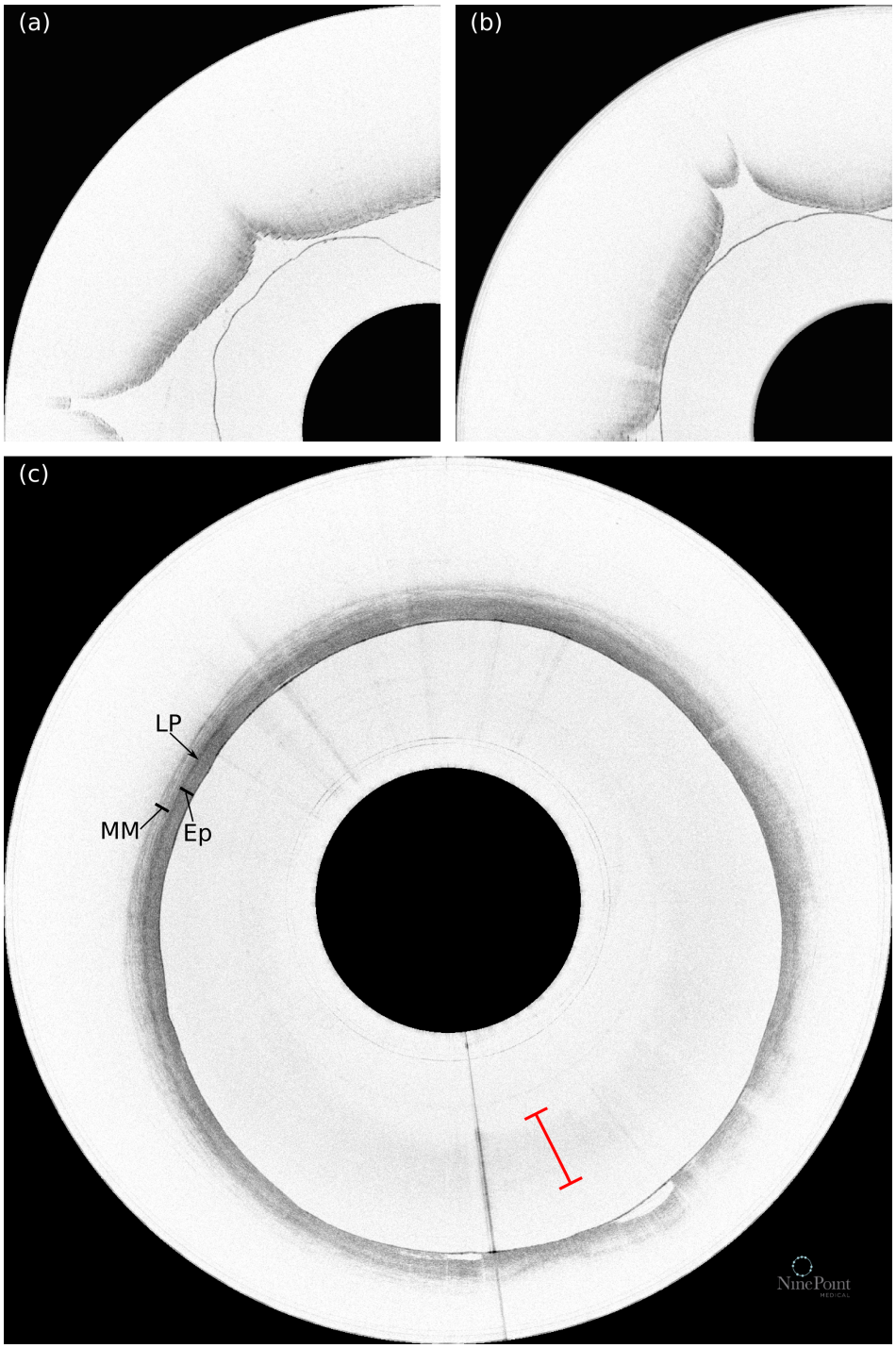

Figure 5.16 Images of fingers taken with (a) an SMF- and (b) a DCF-based GI imaging system. (c) Ex vivo image of a swine esophagus taken with the DCF-based system prototype. The red bar highlights a slight increase in background noise in the region affected by crosstalk-induced artifacts. Ep : Epithelium ; LP : Lamina propria and MM : Muscularis mucosae.

5.4 Discussion

A photo-thermal modeling algorithm, tailored to a MM illumination, was used to simulate single-pulse laser marking. The model was successfully validated using ex vivo single-pulse laser coagulation data. Validation results highlighted the sensitivity of the coagulated zone width and depth to the specific shape of the illumination beam profile. This result emphasizes the relevance of having access to an optical modeling tool for MM propagation such as the one introduced in Chapter 4. The photo-thermal model however appears to overestimate the coagulation depth, even though dynamic changes in scattering properties were considered. As mentioned before, this outcome is to be expected as the model assumes a perfectly collimated beam, thus neglecting the beam divergence beyond the imaging plane.

Photo-thermal modeling of single-pulse laser coagulation for different wavelengths was performed from which wavelength-dependent coagulation thresholds were obtained. It was shown that the coagulation threshold can be used to estimate the coagulated zone lateral dimensions based on the effective radiant exposure. The effective radiant exposure, defined as the energy per surface area, depends upon the beam spot size, the balloon size and probe's rotation speed (providing the tangential speed) as well as the pulse energy and width. A multi-parameter analysis can therefore be performed to assess minimal power (or energy) requirements in order to achieve laser coagulation resulting in visible marks, which criteria were defined in Section 5.1. Such a photo-thermal algorithm can be used to evaluate the capability of different sets of probe- and laser-specific parameters in achieving single-pulse laser marking. Considering the costs and lead-times associated with both high-power laser sources and probes, the model provides an invaluable tool for the design and optimization of a DCF-based dynamic laser marking system.

We also presented an endoscopic DCF-based prototype system for concurrent laser marking and OCT. The system prototype provided satisfying imaging performances, comparable to an equivalent SMF-based system, with minimal crosstalk-induced artifacts. Such artifacts do not overlap with the signal and can thus be filtered out to avoid any ambiguity. Given the MM beam spot diameter ($\sim$700 μm), the system's total transmission for the MM channel ($<$50%), and the maximal power provided by the RFL (30 W), it was not possible to performed dynamic laser marking with the current system prototype. Optical modeling of the laser marking probe, presented in Section 4.3, showed that a beam spot size of $\sim$350 μm can be easily achieved using a GRIN-based design. Assuming no changes in the system's total MM transmission, such a probe could enable dynamic laser marking under in vivo settings providing a laser source with a peak power of more than $\sim$35 W at 1436 nm. This power requirement is however out of the range of our current RFL source. Future work will focus

on the development of such a probe as well as a test bench allowing the tissue temperature to be maintained at 37^{o}C in order to show endoscopic dynamic laser marking

CHAPTER 6 ADDITIONAL IMPACT OF DOUBLE-CLAD FIBER DEVICES FOR BARRETT'S ESOPHAGUS

The following Chapter presents preliminary work aiming at exploring additional modalities enabled by DCF-based systems. We present the implementation of laser therapy monitoring based on a CDV algorithm using the injection DCFC along with ex vivo preliminary results. Additionally, an OCT system with concurrent auto-fluorescence detection is presented. Specific design considerations are discussed and preliminary in vivo testing results are shown.

6.1 Image-guided therapy

A DCF-based system enabling concurrent high-power laser delivery and OCT would be a promising tool for laser therapy monitoring. Such a system could allow for single-fiber microscopic image guidance of epithelial cancers or Barrett's esophagus treatment. To test this hypothesis, the capability of the DCF system to deliver a continuous high-power laser at 1890 nm through the inner cladding while acquiring OCT data for simultaneous quantitative monitoring of the coagulation process was assessed.

6.1.1 System description

To acquire preliminary ex vivo results, a DCF-based benchtop setup was used. Laser therapy is performed using a continuous TFL at 1890 nm. A commercial DCFC (Castor Optics, DC1300LJ, prototype version) is used to combine the OCT SM signal and the therapy laser within the DCF. At this wavelength, a MM coupling of ∼40% from the injection fiber to the DCF inner cladding is obtained [1]. The imaging arm also comprises a collimator, a set of 2D mirror-mounted galvanometers as well as a 5X scanning lens (LSM03, Thorlabs), providing a MM beam spot size diameter of ∼540 μm. The maximum power at the sample is ∼260 mW.

6.1.2 Data processing for quantitative therapy monitoring

To achieve the quantitative monitoring, a CDV algorithm including a signal-to-noise ratio (SNR) correction, as described in Ref. 57, was used. Briefly, for a pair of consecutive A-lines, taken at times t and $t+1$, the CDV is computed as follows :

1. For this version of the coupler, a decrease of the MM coupling as a function of wavelength (from 1436 to 1890 nm) was observed and reported to the manufacturer. An optimized version (DC1300LQ, Castor Optics) providing an increased coupling with a flat spectral behaviour is now available.

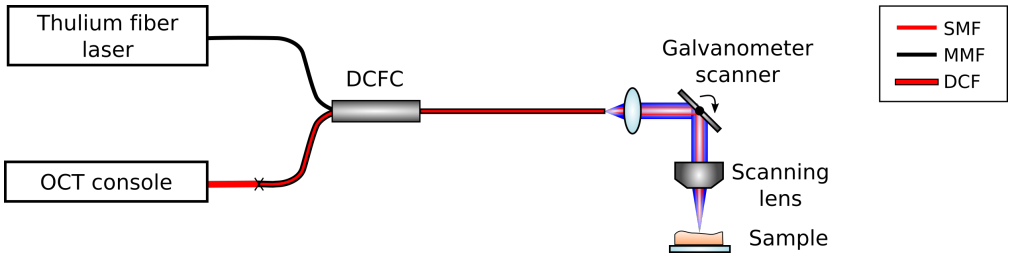

Figure 6.1 Schematic of the setup used for combined OCT and laser therapy.

$$f_{CDV}(z) = \sqrt{1 - \frac{\sum_{t=0}^{M-1} \left| \sum_{l=-L}^{L} w(l) R(z-l,t) R^*(z-l,t+1) \right|}{\sum_{t=0}^{M-1} \sum_{l=-L}^{L} w(l) \frac{1}{2} \left[|R(z-l,t)|^2 + |R(z-l,t+1)|^2 \right]}}, \tag{6.1}$$

where $R(z,t)$ and $R^*(z,t)$ are the complex OCT signal and its complex conjugate, respectively, $w(l)$ is a depth window function with length $2L+1$, and M is the number of consecutive images used for temporal averaging. This equation corresponds to the ratio of the magnitude of the complex correlation term between times t and $t+1$ summed across the depth defined by $w(l)$ to the corresponding summation of magnitudes. The algorithm is therefore sensitive to any phase or intensity modulation due to scatterer motion induced by laser heating, but insensitive to small axial bulk tissue motion and instrument synchronization errors.

Here, we used a temporal window of $M = 5$ images and a Hanning window of length 11 pixels ($L = 5$) for $w(l)$. The SNR-dependent calibration was performed using a static region of the tissue corresponding to a window of 35 x 20 pixels after a 10x downsampling of both intensity and raw CDV images.

6.1.3 Preliminary ex vivo results and discussion

The setup and algorithm were used for laser therapy monitoring of ex vivo swine esophageal tissue. Figure 6.2 shows the SNR-dependent CDV along with its exponential fit, which was subtracted from the raw CDV. Figure 6.3 shows intensity images, calibrated CDV values mapped onto the intensity image as well as the coagulation zone visualization at different time points during the high power illumination. The intensity images (Figure 6.3a) show an increase in scattering superficially, starting in the center of the field of view, and reaching deeper and wider as the coagulation progresses. This half-moon shape is created by the scanning of the beam resulting in higher cumulative radiant exposure in the center of the

tissue. CDV results are presented in Figure 6.3b overlaid onto the intensity images. As the tissue is heated by the scanning high-power laser and coagulation is triggered, scatterers motion will produce a rise in CDV (from yellow to blue). This increase in CDV will progress in depth as the coagulation zone reached deeper into the tissue. Upon complete coagulation of the tissue, CDV will drop again to a value comparable to static regions (i.e. yellow) consistent with the stabilization of the scatterers. Using this dynamic process (i.e. CDV increase followed by a return to baseline value), it is possible to visualize the coagulation zone as shown in Figure 6.3c. Lo et al. showed that the coagulation zone detected using the CDV algorithm corresponds well with histological analysis. At times 1.2 and 1.8 s, some saturation artifacts (caused by the increase in tissue scattering) are visible causing higher CDV values.

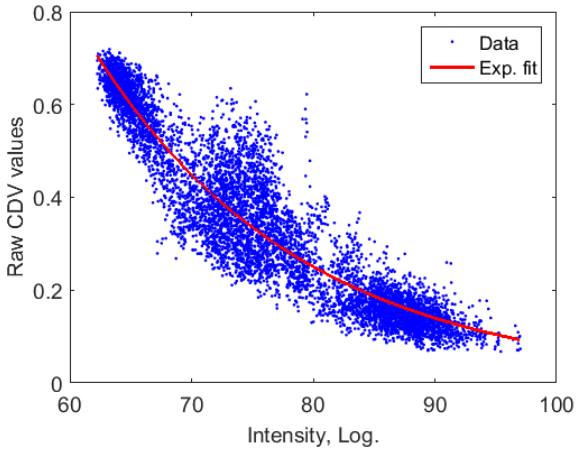

Figure 6.2 Calibration curve obtained for the SNR-dependent CDV.

These results show the potential of a DCF-based system for concurrent laser therapy and OCT-based monitoring. We also show that it is possible to use a CDV algorithm to quantitatively assess the coagulation zone when using the DCF system, even though the therapy beam was scanned concurrently with the imaging beam. One can however observe some higher CDV regions deeper than the actual coagulation zone. This could either be due to the motion of scatterers beyond the coagulation depth or to a background noise associated with crosstalk-induced artifact overlapping with the tissue signal. More investigation is required to assess the contribution of such noise. The endoscopic DCF-based system described in Section 5.3 could readily be used for this application. An optimized version of the CDV algorithm compensating for NURD is currently under development [121], therefore enabling quantitative monitoring to be used endoscopically with a balloon-catheter.

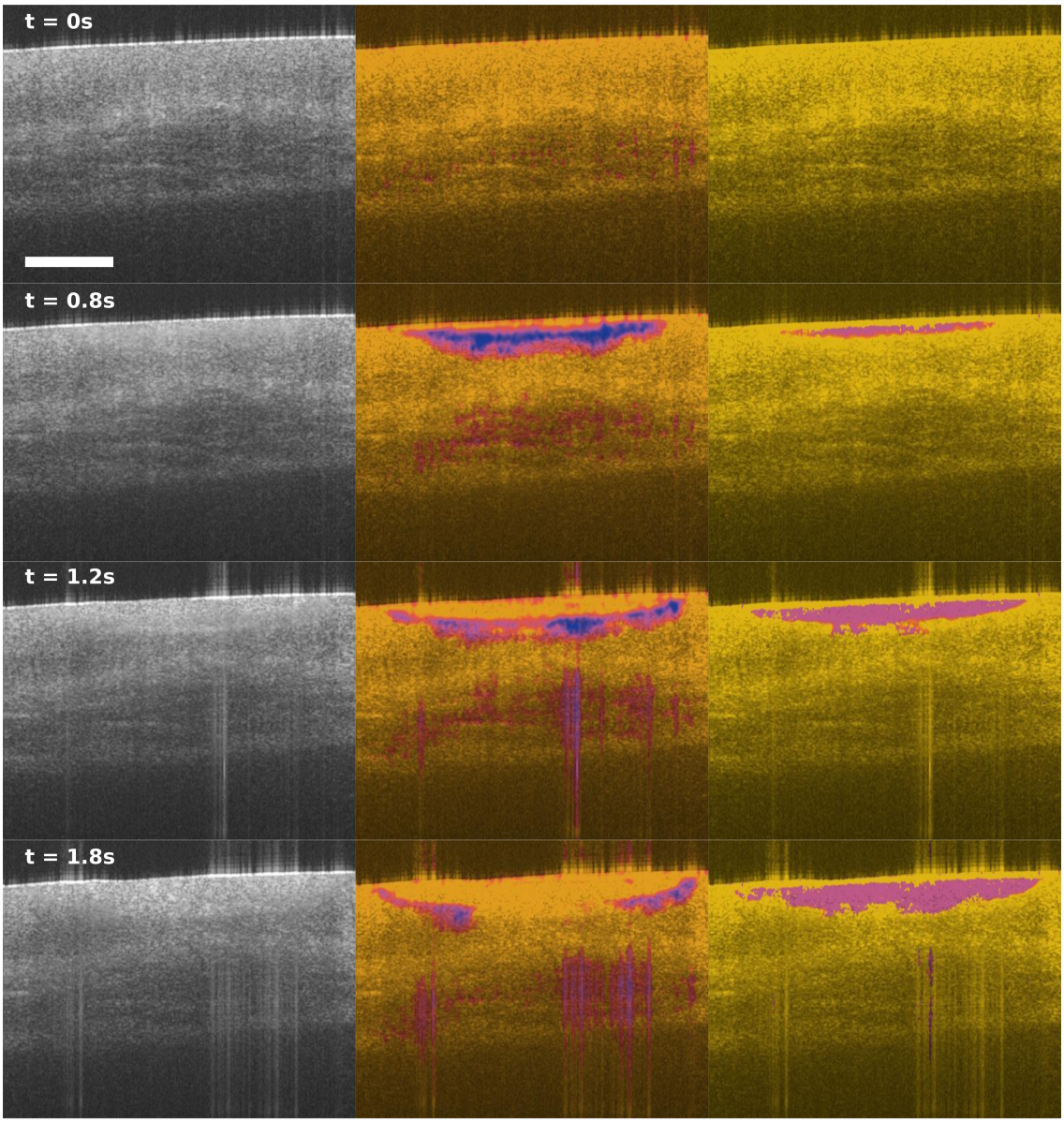

Figure 6.3 Results of concurrent single-fiber OCT and laser therapy monitoring. (a) Intensity images, (b) calibrated CDV values and (c) coagulation zone visualization overlaid with the intensity images at different time points. Scale bar = 500 μm.

6.2 Combined OCT and auto-fluorescence imaging

The goal of this project is to assess whether AFI could be combined to a conventional OCT system to provide molecular contrast for esophageal imaging to probe the submucosal collagen content. When illuminated with blue excitation light, submucosal collagen shows a fluorescence signature in the green band (i.e. ∼500 nm). As mentioned in Chapter 2, AFI was previously used for GI imaging in a wide-field endoscopy configuration ; herein, we investigated AFI implemented through a single-fiber using a DCF-based system. We hypothesize that the use of a DCF allows enough signal collection through the large inner cladding to provide a fluorescence contrast.

6.2.1 System design

The design of the combined OCT and AFI system is based on previously demonstrated DCF-based systems [28, 80]. The fiber core is used for the OCT signal as well as for the excitation light. An SM excitation is chosen as it provides higher resolution as opposed to an inner cladding excitation [28]. The system design is presented in Figure 6.4. A 405-nm laser diode (QFLD-405-20Sm QPhotonics) was chosen for optimal excitation of the collagen content of the submucosa [71]. The output fiber of the diode (S405-XP) was connected to a WDM. The WDM (CDI8881 - custom order, Thorlabs) was optimized to maximize the transfer of the 405-nm signal through the SMF-28 core while maintaining minimal losses at 1310 nm. A custom DCFC (DC1300LEC-S-LT, Castor Optics) was used to couple the OCT and excitation signals into the DCF core as well as extracting the emission signal coming back from the sample via the inner cladding. This coupler uses a 200-μm MM core fiber as the extraction fiber.

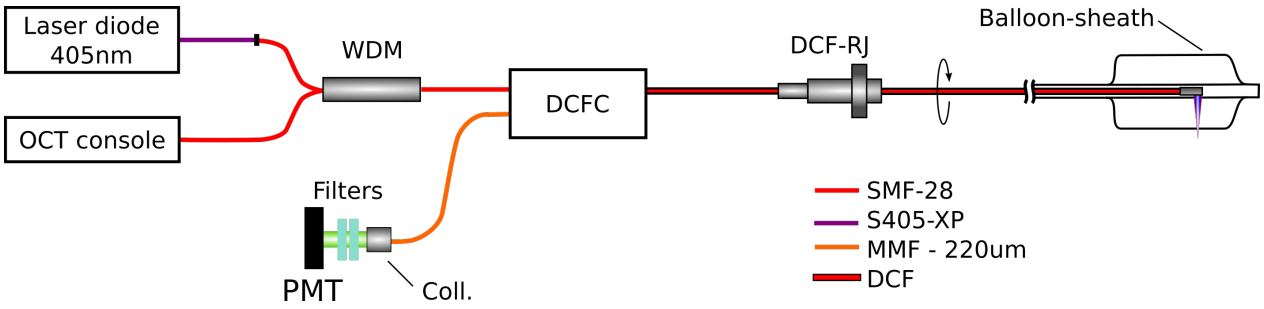

Figure 6.4 Schematic of the setup used for combined OCT and AFI. The legend indicates which fiber is used for each component.

In order to optimize the transmission of the visible light through the RJ, two different models

were tested. The MJPP model, as described in Section 5.3.1, presents very high insertion loss at 405 nm of about 19 dB. Since this model is optimized for an SM transmission at 1310 nm, the blue excitation light suffers from important chromatic aberrations. Therefore, an index-matching fluid based-RJ (MJXP, Princetel) was chosen. This particular model, compared to the RPT model tested in Section 5.3.1, shows better insertion loss performance, which should, therefore, provide better outcome for the crosstalk-induced artifacts. Table 6.1 summarizes insertion loss for each component of the system for the different wavelengths used.

Table 6.1 Insertion loss characterization of the system components

Component	OCT signal 1310 nm - core	Excitation 405 nm - core	Emission ∼530 nm - inner cladding
WDM	0.3 dB	1.7 dB	-
DCFC	0.1-0.3 dB	0.5 dB	0.85 dB
MJXP DCF-RJ	0.5 dB	0.5-0.8 dB	0.3 dB
Total	**∼1 dB**	**∼3 dB**	**1.15 dB**

The detection module consists of a collimator (CFC-2X-A, Thorlabs) connected to the MM port of the DCFC, a long-pass filter for excitation light rejection (ET460lp, Chroma), a band-pass filter (ET510/80m, Chroma) and a photomultiplier tube (PMT) module (H12402-01, Hamamatsu). The detection module was enclosed in an air-tight box to protect the PMT from ambient light.

A DCF GRIN-based catheter was first tested for transmission assessment for the different wavelength bands providing >90% transmission of the core signal (1310 nm), and ∼30% transmission of the green band through the inner cladding. The 405-nm excitation through the core, however, induced significant damage to the assembly even at low power. The damage is due to the high absorption of this wavelength by the adhesive used for the distal optics. To performed preliminary testing, a DCF mirror-based prototype catheter from Ninepoint Medical was therefore used.

6.2.2 Preliminary in vivo testing

The combined AFI-OCT system was tested in vivo on a swine model by Ninepoint Medical. The study protocol was approved by CBSET, Inc. and carried out in accordance with regulations as set forth in the USDA AWA/AWR [2]. The swine was anesthetized, intubated, and ventilated using standard methods. Under endoscopic guidance, the balloon-catheter was inserted and positioned in the esophagus. Once the balloon was properly inflated, simultaneous

2. United States Department of Agriculture's Animal Welfare Act and Animal Welfare Regulations.

OCT and AFI acquisition was performed over a 6-cm long segment.

OCT imaging quality

To evaluate the OCT imaging quality as well as potential contributions to noise level from the DCFC and DCF-RJ, an SMF catheter was first used along with the DCF-based system. Figure 6.5 presents a typical image showing swine esophageal tissue characterized by a layered structure composed of the epithelium, lamina propria, muscularis mucosae and submucosae. Even though an increased background level is observed, satisfying imaging quality and penetration depth are obtained. This background may either be caused by return loss from the RJ, may correspond to crosstalk-induced artifact, or a combination of both effects.

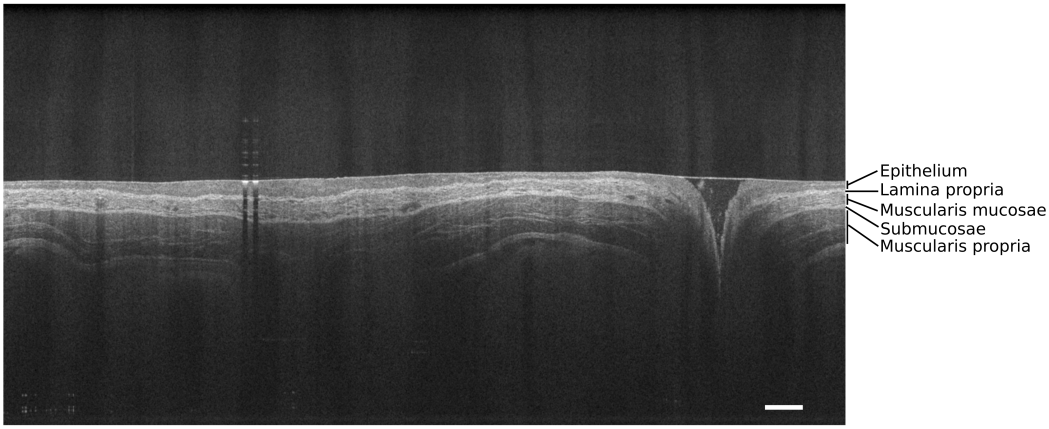

Figure 6.5 In vivo OCT image of a swine esophagus taken with the DCF-based system and an SMF catheter. Increased background is observed. Scale bar = 2 mm.

Fluorescence signal processing

Because of the rather high background in the fluorescence channel (which will be discussed later), some processing steps were required to achieve good imaging quality as shown in Figure 6.6. To remove the constant background coming from the system and modulated by power fluctuations of the diode, the data were first fitted using a 5^{th} order polynomial function and subtracted from the signal. The second row in Figure 6.6 shows the resulting signal and image. One can observe that the intensity appears to be modulated by longitudinal variations (i.e. vertical bands) along the catheter, which could be coming from the balloon or inner sheath. This modulation was rejected by first smoothing the signal using a window size about 10x larger than the frame size and subtracting the resulting background from the

signal. The last row of Figure 6.6 shows the resulting signal and image free of low-frequency fluctuating background.

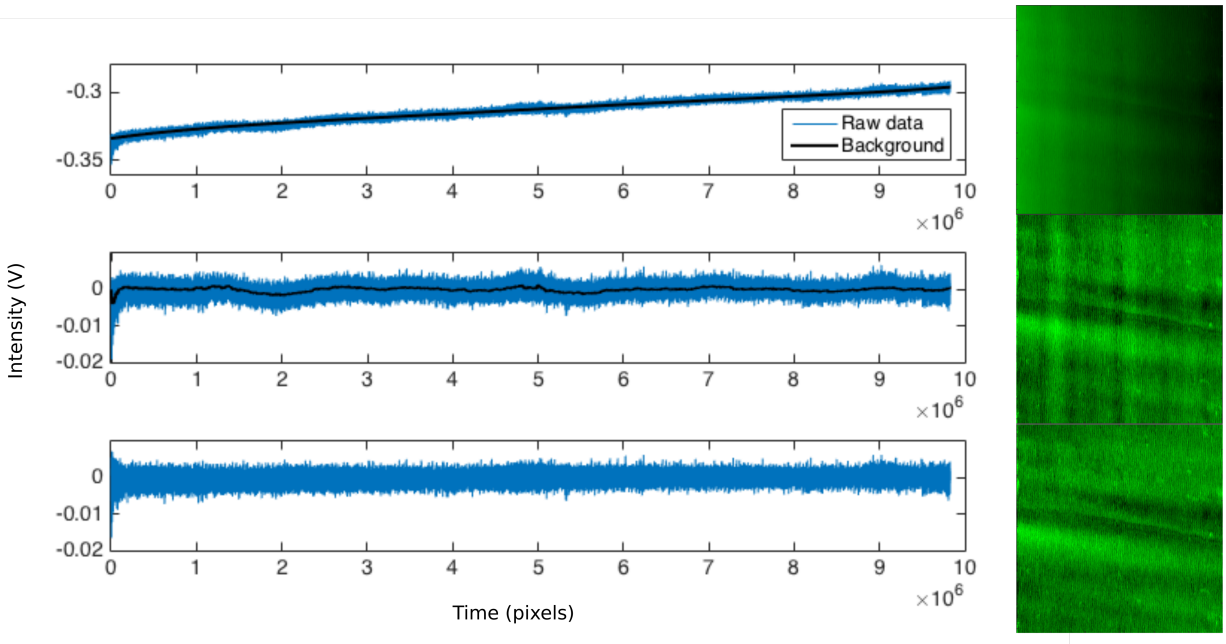

Figure 6.6 Signal intensity as a function of time at each processing step. Insets on the right column show the original image and resulting images after each correction.

Combined AFI and OCT

OCT en face projection of esophageal tissue is shown in Figure 6.7 alongside with its corresponding fluorescence image. On the OCT projection, one can see some variation in intensity due to centering of the catheter. Vascular network is also seen. The left-hand side of the image also suffers from NURD creating zipper-like structures. Since it corresponds to healthy tissue, we do not expect large variation in fluorescence signal such that the contrast mainly comes from the positioning of the tissue with respect to the catheter. However, one can observe some high intensity spots highlighted using black and red arrows. Black arrows indicate laser marks, done with a continuous laser prior to imaging, recognizable by their hyper-scattering properties. Other high intensity spots are however observed on the fluorescence image, which does not correspond to laser marks, indicated by the red arrows. In this case, these spots appear to correspond to round hypo-scattering structure on the OCT projection. Figure 6.8 shows cross-section regions corresponding to these structures. For each of these regions, a spherical structure is observed within the epithelium pressing down onto the lamina propria. More investigation is required to fully understand the nature of these structures. As to their

contribution to the fluorescence contrast, two hypotheses are considered. First, these spheres could directly be responsible for the increased signal in fluorescence. Another hypothesis is that, due to their hypo-scattering nature, they could contribute to more fluorescence signal coming from deeper collagen content to be detected.

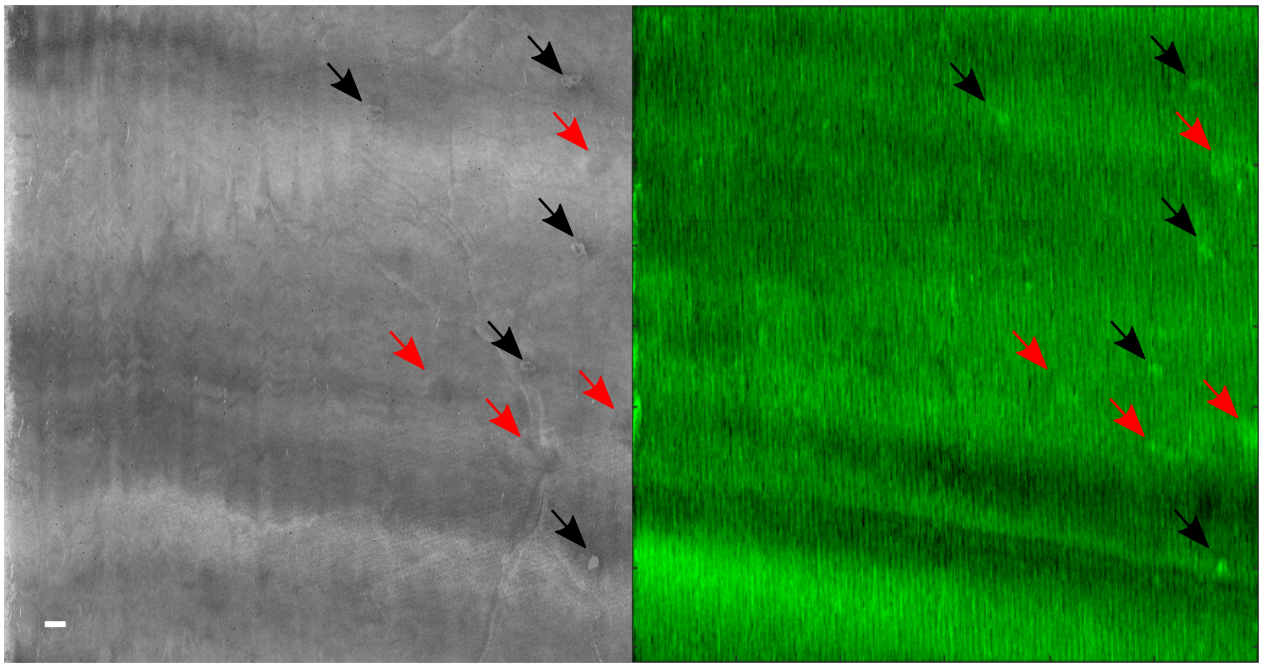

Figure 6.7 In vivo OCT and fluorescence en face images of a swine esophagus. Black arrows indicate laser marks corresponding to hyper-scattering or crater-like spots on the OCT image. Red arrows indicate regions with higher fluorescence signal, but showing low scattering signal on the OCT image. Scale bar = 2 mm.

6.2.3 Discussion

More work must be performed to fully understand the origin of the fluorescence signal obtained using the combined AFI-OCT system. We were nonetheless able to show that the DCF-based system allow for enough signal collection to provide a tissue-specific contrast for the fluorescence channel. Our results also highlight the added advantages of combining structural and molecular imaging, both providing complementary information that is essential for the analysis of the signal. It was indeed possible to, based on the AFI signal, identify structures that could have been missed otherwise.

The system design could be further improved to provide better imaging quality. The system generates significant background such that post-processing is necessary to retrieve the signal.

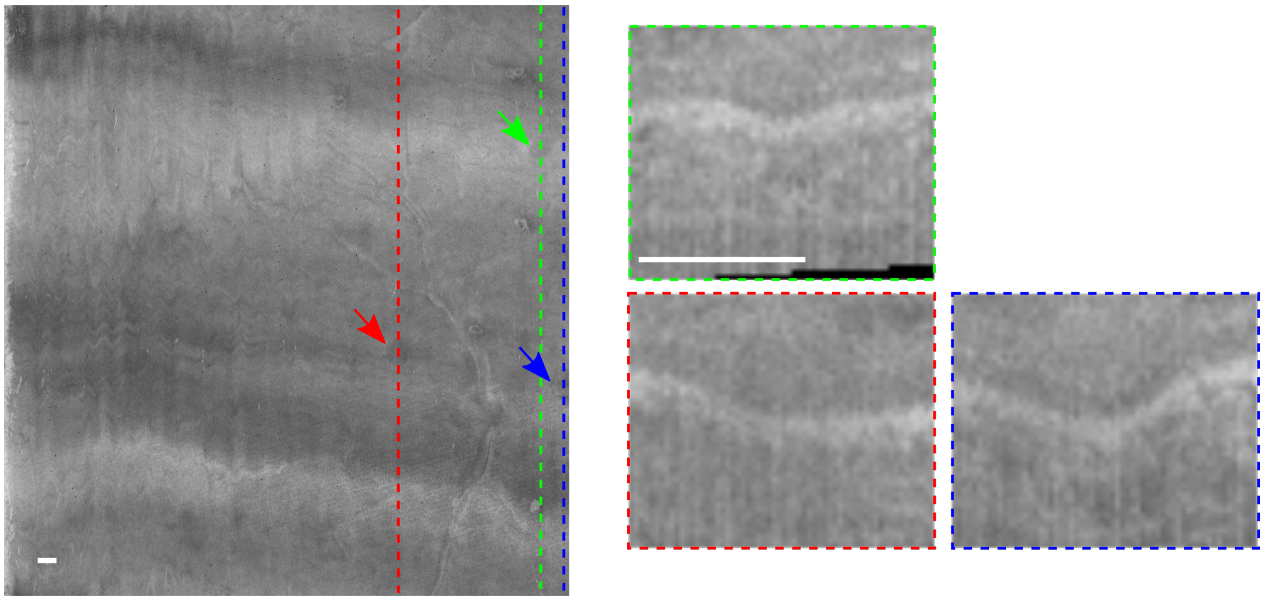

Figure 6.8 In vivo OCT en face image of a swine esophagus. Arrows show round hypo-scattering structures identified on the fluorescence image, and the dashed lines show the location of the corresponding cross-sections shown on the right. Scale bars = 2 mm.

This background is most likely due to scattering or fluorescence generated by the 405-nm excitation light in the fiber itself. The use of a slightly longer wavelength (∼450 nm) could decrease significantly the background while maintaining an efficient excitation of the collagen content. This wavelength change would also allow the use of GRIN-based catheters.

Some questions still remain regarding the sensitivity of the system to detect variation in auto-fluorescence signal associated with esophageal pathologies. Another potential avenue could reside in the use of exogenous agents. Indeed, recent studies have investigated the use of labeled peptides to achieve targeted detection of dysplasia and neoplasia in Barrett's patients [122, 123].

CHAPTER 7 GENERAL DISCUSSION

This dissertation aimed at developing a DCF-based system and devices for dynamic laser marking to guide biopsy procedures for Barrett's esophagus. Several specific objectives were set to achieve that goal. The following Chapter will discuss in details the fulfillment of each of these objectives.

7.1 Development of an injection DCFC and a DCF-based laser delivery system

The first objective of the dissertation was to develop a dedicated DCFC for high-power light delivery. We hypothesized that the etendue tailoring of fused components, as introduced in Section 2.5.2, could be used to obtain an injection DCFC, as shown for extraction DCFCs previously developed. We thus presented the first demonstration of such a DCFC in Ref. 124 and presented in Chapter 3. This first prototype shows a core transmission of >90% as well as 66% of MM coupling. Even though the MM coupling was just above the 50% theoretical limit of symmetric DCFC, this result demonstrated promising avenues for the development of injection DCFCs. Since that first prototype, several versions of the injection DCFC have been developed and built, now providing a MM coupling of ∼85% from 1200 to 1600 nm and >75% up to 2200 nm (DC1300LQ, Castor Optics). Such coupling performance is critical for systems where each photon needs to be accounted for such as a dynamic laser marking system. This new version also opens the door to the deployment of injection DCFCs for laser therapy applications for which higher wavelengths (>1900 nm) are typically used.

The DCF-based benchtop system was used to demonstrate dynamic laser marking, therefore confirming the hypothesis that we issued at the beginning of the dissertation. Indeed, DCF-based systems enable dynamic laser marking through the MM delivery of pulsed illumination through the inner cladding. This first demonstration was however achieved using a benchtop system involving a scanning lens (resulting in a rather small MM beam spot size) and a slow beam scanning speed, which, as we showed in Chapter 5, have a significant impact on the coagulation capability of a system.

The single-fiber scheme allows for simultaneous and co-localized laser coagulation and OCT imaging, thus enabling the real-time assessment of thermal dynamic processes. Chapter 3 presented how the OCT signal can indeed be used to assess dynamic changes in scattering showing attenuation curves at different time points during high-power illumination of a sample. Such a capability also opens the door to the use of a DCF-based system to achieve

laser therapy monitoring. Preliminary results showing the use of a CDV algorithm to perform DCF-based monitoring are therefore presented in Section 6.1. Co-registation of the therapy and monitoring modalities is critical for such application, thus showing the clear advantage of using a DCF. To the best of our knowledge, this is the first demonstration of the use of DCF for laser therapy monitoring.

A quantitative evaluation of crosstalk-induced ghost artifacts was also performed for various DCF components. The use of DCF components for coherent detection introduces image artifacts from the crosstalk between the inner cladding modes and the core fundamental mode. This crosstalk occurs at the different coupling interfaces including splice sites, connectors, the fused section of DCFCs and DCF-RJs. As long as these coupling interfaces show some insertion loss, crosstalk-induced artifacts will be present. In Chapter 3, we discussed strategies to mitigate the effect of this added noise. As these artifacts are created from a delay proportional to the optical path length between crosstalk sites (Eq. 3.2), adjusting the fiber length between these can push the artifacts out of the imaging range. We also showed that the intensity level of such artifacts is proportional to the tissue intensity. Therefore, reducing the specular reflection, which typically does not contribute in providing useful information about the studied tissue, will proportionally decrease the intensity of the crosstalk-induced artifacts. Even though these strategies can mitigate the effect of the artifacts, it is important to note that the signal leaking to the inner cladding will be lost to noise. Throughout this dissertation, we showed that the main contributor to crosstalk-induced artifacts is the DCF-RJ emphasizing the importance of choosing an optical design minimizing core insertion loss.

7.2 Modeling and optimization of an endoscopic laser marking system

In order to translate this system into a clinically-compatible endoscopic system, a modeling and optimization platform for DCF devices was introduced. This two-part platform was achieved by 1- developing an optical model describing both the SM and MM propagations, and 2- tailoring a photo-thermal model to simulate a pulsed MM illumination. Both models were validated and used to simulate different design options.

The optical model presented in Chapter 4 was developed based on the theoretical description of partially coherent light as described in Section 4.1. This theoretical model states that a MM beam, corresponding to a partially coherent beam, can be represented as a combination of beamlets associated with a coherence area of that of a coherent beam. The superposition field created by these beamlets shows, as it propagates, a divergence N_μ times larger than that of a coherent beam, given the same propagation distance and where N_μ corresponds

to the number of modes. To simulate MM propagation and thus provide a representative model of a DCF output, the MM beam was modeled as a non-sequential circular source consisting of a combination of beamlets of NA corresponding to that of the fiber's inner cladding. Both the SM and MM propagation as simulated by the model were validated using experimental data showing successful prediction of the propagation behaviour for both channels. This model however has some limitations. First, even though the MM beam shows some intensity fluctuations across its field (as seen in Figure 4.5b), these do not correspond to the speckle pattern generated by the guided modes of the fiber, but are rather due to the rays' discretization. Also, a non-sequential treatment of the SM beam does not take account of coherent effects such as diffraction and interference, such that a sequential analysis should be preferred for such assessment. The optical model developed however proved to be an invaluable tool to assess the propagation behaviour of both the SM and MM channels of a DCF and to optimize the laser marking probe.

The second part of the modeling platform consists of a photo-thermal model that was tailored for a MM illumination, thus taking into account the beam profile shape of the source. An incremental loop was also added to the algorithm in order to include the effect of dynamic changes in scattering properties occurring during tissue coagulation. It was shown that these dynamic changes have an effect, especially on the coagulation depth, for slow- or non-scanning beam configurations. The photo-thermal modeling allows for multi-parameter simulations to be performed including probe- (beam spot size and profile shape) as well as laser-specific (pulse width and energy or peak power) parameters. Considering costs and lead-times associated with both high-power laser sources and probes, this algorithm provides an invaluable tool for the design and optimization of a DCF-based dynamic laser marking systems.

7.3 Endoscopic DCF-based systems

An endoscopic DCF-based system prototype for concurrent OCT and laser marking was also built to assess imaging quality and high-power transmission of all DCF components. The system prototype shows satisfying performances in terms of resolution and penetration depth, comparable to an equivalent SMF-system, with minimal crosstalk-induced artifacts. The system currently allows for a MM transmission of $\sim$50% such that the laser marking probe optimization is critical in order to achieve dynamic laser marking endoscopically.

Finally, we investigated additional uses of DCF-based systems for Barrett's esophagus, namely laser therapy OCT-based monitoring, as described above, and AFI with concurrent OCT imaging. Section 6.2 presents the design of an endoscopic system combining OCT and AFI. The goal of this project was to investigate whether the use of a DCF can allow sufficient

signal collection to enable in vivo auto-fluorescence detection in the esophagus. Previous studies demonstrated such systems for other organs [28, 74], but the need for a long working distance probe compatible with GI imaging constitutes an additional challenge in this case. With the use of the combined system, OCT and AFI images were acquired in vivo in a swine model showing tissue-specific contrast. Further work is however required to fully understand the origin of this contrast and to assess whether it indeed corresponds to an auto-fluorescence signal.

CHAPTER 8 CONCLUSION

8.1 Recommendations for in vivo dynamic laser marking

As stated previously, the DCF-based endoscopic system prototype for concurrent OCT and laser marking does not provide the required specifications to achieve dynamic laser marking in vivo. However, based on the modeling and optimization work presented in this dissertation, it is possible to issue specific recommendations to achieve such a system.

8.1.1 Laser marking probe

Section 4.3 presented the analysis of different possible designs for the laser marking probe based of the developed optical model. We focused our analysis on designs that presented a certain ease of manufacturing. We showed that the single GRIN lens design corresponds to the best option in terms of performances and robustness. Optimization of such design involves a trade-off in order to maximize the laser marking peak irradiance while optimizing the imaging resolution and depth-of-field. We therefore showed that a probe design providing an SM $1/e^2$ radius between 15 and 20 μm is the best option. Such a design yields a MM beam spot diameter, at the tissue surface, between 275 and 350 μm.

8.1.2 Minimal power requirements to achieve dynamic laser marking

Based on the choice of the laser marking probe design and laser marking visibility criteria, it is possible, with the use of the photo-thermal modeling algorithm, to define the power requirement to achieve dynamic laser marking in vivo. Assuming a 14-mm balloon size, an acquisition rate of 13 frames/s, and a MM beam spot size of about 350 μm, the minimal peak power at 1436 nm required at the sample is about 15 W. The current prototype system is limited to a MM global transmission of <50%. However, using the recently developed injection DCFC, with a MM coupling of 85%, the system's transmission would increase to just above 50%. With such system, the required peak power at the source should be at least 30 W. Similar analysis should be performed for different balloon size, which will involve higher tangential speeds.

We also showed that the peak power requirement at higher wavelengths, namely 1890 and 1940 nm, is significantly reduced. Given that fiber lasers are readily accessible for these wavelengths, performances of the DCF system should be evaluated to assess whether the decrease of the required power can outweigh the potential lower MM transmission of DCF

system.

8.1.3 Other considerations

As mentioned in Section 5.1, the marking visibility could greatly be improved using few coagulation marks on each side of the region of interest as opposed to an individual mark. Such a scheme would however be possible only providing a certain flexibility over the repetition rate and duty cycle permitted by the marking laser. The ideal setup would be the use of a marking laser allowing a single-pulse (or few pulses) to be generated upon a trigger signal, a capability that is available for some fiber lasers. Such capability would further avoid the necessity of a shutter to control the pulse delivery.

8.2 Outlook

We herein were able to demonstrate DCF-based dynamic laser marking and issue specific requirements to achieve endoscopic dynamic laser marking in vivo. Additional work is still required to demonstrate the endoscopic system and to assess the added advantages associated with such system. The developments achieved and presented throughout this dissertation have however impacts beyond the scope of this particular project. Indeed, it was shown that DCF-based systems can be used for additional modalities such as laser therapy and AFI. The development of the injection DCFC also opens the door to a multitude of applications based on light delivery. We focused our attention on laser coagulation processes, but the use of an injection DCFC for ablative or low-level therapy could be further investigated. The capability of DCF-based systems for concurrent monitoring could have a significant impact on the effectiveness of such therapies.

We also introduced an optimization and modeling platform tailored to the use DCF components. The DCF optical model could be used to optimize DCF probes for a variety of modalities including, but not limited to, linear or non-linear fluorescence, confocal, hyperspectral or spectroscopic imaging. In addition to be used to assess the illumination volume, the model can further be used to quantify and localized the collection volume, an aspect that was not fully assessed in previous studies and which has a significant impact for systems using distinct wavelength bands. The model can also be used to assess performances of other DCF components such as RJs to evaluate chromatic effects as well as insertion loss, the latter associated with crosstalk-induced artifacts. In conclusion, the work presented in this dissertation corresponds to important steps in the development and deployment of DCF-based systems, provided invaluable optimization and modeling tools to the community in addition

to opening the door to additional research avenues.

REFERENCES

[1] D. G. King, "SIU SOM Histology GI, 2001," [Accessed : 2017-02-07]. [Online]. Available : http://www.siumed.edu/~dking2/erg/GI006b.htm

[2] ——, "SIU SOM Histology GI, 2002," [Accessed : 2017-02-07]. [Online]. Available : http://www.siumed.edu/~dking2/erg/GI108b.htm

[3] Nephron, "Wikimedia Commons, 2010," [Accessed : 2016-10-18]. [Online]. Available : http://commons.wikimedia.org/wiki/File:Esophageal_adenocarcinoma_-_intermed_mag.jpg

[4] M. J. Suter, B. J. Vakoc, P. S. Yachimski, M. Shishkov, G. Y. Lauwers, M. Mino-Kenudson, B. E. Bouma, N. S. Nishioka, and G. J. Tearney, "Comprehensive microscopy of the esophagus in human patients with optical frequency domain imaging." *Gastrointestinal endoscopy*, vol. 68, no. 4, pp. 745–53, 2008.

[5] D. J. Segelstein, "The complex refractive index of water," Ph.D. dissertation, University of Missouri–Kansas City, 1981.

[6] S. Prahl, "Tabulated molar extinction coefficient for hemoglobin in water, 1998," [Accessed : 2014-02-28]. [Online]. Available : http://omlc.ogi.edu/spectra/hemoglobin/summary.html

[7] R. Kitamura, L. Pilon, and M. Jonasz, "Optical constants of silica glass from extreme ultraviolet to far infrared at near room temperature," *Applied Optics*, vol. 46, no. 33, p. 8118, 2007.

[8] S. Lemire-Renaud, M. Rivard, M. Strupler, D. Morneau, F. Verpillat, X. Daxhelet, N. Godbout, and C. Boudoux, "Double-clad fiber coupler for endoscopy." *Optics express*, vol. 18, no. 10, pp. 9755–64, 2010.

[9] W.-J. Madore, E. De Montigny, O. Ouellette, S. Lemire-renaud, M. Leduc, X. Daxhelet, N. Godbout, and C. Boudoux, "Asymmetric double-clad fiber couplers for endoscopy," *Optics Letters*, vol. 38, no. 21, pp. 4514–4517, 2013.

[10] T. Perrillat-Bottonet, M. Strupler, M. Leduc, L. Majeau, N. Godbout, and C. Boudoux, "All-fiber nonlinear microscopy at 1550 nm using a double-clad fiber coupler," in *Proc. of SPIE 10069, Multiphoton Microscopy in the Biomedical Sciences XVII*, vol. 10069, 2017, pp. 1–10.

[11] J. Mertz, *Introduction to optical microscopy.* Roberts and Company Publishers, 2010.

[12] M. A. Eloubeidi, A. C. Mason, R. A. Desmond, and H. B. El-Serag, "Temporal trends (1973–1997) in survival of patients with esophageal adenocarcinoma in the United States : a glimmer of hope&quest," *The American journal of gastroenterology*, vol. 98, no. 7, pp. 1627–1633, 2003.

[13] K. K. Wang and R. E. Sampliner, "Updated guidelines 2008 for the diagnosis, surveillance and therapy of Barrett's esophagus." *The American journal of gastroenterology*, vol. 103, no. 3, pp. 788–97, 2008.

[14] H. Pohl and H. G. Welch, "The role of overdiagnosis and reclassification in the marked increase of esophageal adenocarcinoma incidence." *Journal of the National Cancer Institute*, vol. 97, no. 2, pp. 142–6, 2005.

[15] M. J. Suter, P. A. Jillella, B. J. Vakoc, E. F. Halpern, M. Mino-Kenudson, G. Y. Lauwers, B. E. Bouma, N. S. Nishioka, and G. J. Tearney, "Image-guided biopsy in the esophagus through comprehensive optical frequency domain imaging and laser marking : a study in living swine." *Gastrointestinal endoscopy*, vol. 71, no. 2, pp. 346–53, 2010.

[16] D. Huang, E. A. Swanson, C. P. Lin, J. S. Schuman, W. G. Stinson, W. Chang, M. R. Hee, T. Flotte, K. Gregory, C. A. Puliafito, and E. al., "Optical coherence tomography," *Science*, vol. 254, no. 5035, pp. 1178–1181, 1991.

[17] G. J. Tearney, M. E. Brezinski, B. E. Bouma, S. A. Boppart, C. Pitris, J. F. Southern, and J. G. Fujimoto, "In vivo endoscopic optical biopsy with optical coherence tomography," *Science*, vol. 276, no. 5321, pp. 2037–2039, 1997.

[18] J. Evans, J. Poneros, and B. Bouma, "Optical coherence tomography to identify intramucosal carcinoma and high-grade dysplasia in Barrett's esophagus," *Clinical gastroenterology and hepatology*, vol. 3565, no. 05, pp. 38–43, 2006.

[19] J. M. Poneros, S. Brand, B. E. Bouma, G. J. Tearney, C. C. Compton, and N. S. Nishioka, "Diagnosis of specialized intestinal metaplasia by optical coherence tomography," *Gastroenterology*, vol. 120, no. 1, pp. 7–12, 2001.

[20] J. A. Evans, B. E. Bouma, J. Bressner, M. Shishkov, G. Y. Lauwers, M. Mino-Kenudson, N. S. Nishioka, and G. J. Tearney, "Identifying intestinal metaplasia at the squamocolumnar junction by using optical coherence tomography." *Gastrointestinal endoscopy*, vol. 65, no. 1, pp. 50–6, 2007.

[21] G. Isenberg and A. Chak, "Should there be light in the esophageal tunnel? An appraisal of optical coherence tomography in Barrett's esophagus." *Gastrointestinal endoscopy*, vol. 65, no. 1, pp. 57–9, 2007.

[22] B. J. Vakoc, M. Shishkov, S. H. Yun, W.-Y. Oh, M. J. Suter, A. E. Desjardins, J. A. Evans, N. S. Nishioka, G. J. Tearney, and B. E. Bouma, "Comprehensive esophageal microscopy by using optical frequency-domain imaging (with video)." *Gastrointestinal endoscopy*, vol. 65, no. 6, pp. 898–905, 2007.

[23] M. J. Suter, M. J. Gora, G. Y. Lauwers, T. Arnason, J. Sauk, K. A. Gallagher, L. Kava, K. M. Tan, A. R. Soomro, T. P. Gallagher, J. A. Gardecki, B. E. Bouma, M. Rosenberg, N. S. Nishioka, and G. J. Tearney, "Esophageal-guided biopsy with volumetric laser endomicroscopy and laser cautery marking : a pilot clinical study," *Gastrointestinal Endoscopy*, vol. 79, no. 6, pp. 886–896, 2014.

[24] C. Guarner-Argente, T. Buoncristiano, E. E. Furth, G. W. Falk, and G. G. Ginsberg, "Long-term outcomes of patients with Barrett's esophagus and high-grade dysplasia or early cancer treated with endoluminal therapies with intention to complete eradication." *Gastrointestinal endoscopy*, vol. 77, no. 2, pp. 190–9, 2013.

[25] M. Villiger, A. Soroka, G. J. Tearney, B. E. Bouma, and B. J. Vakoc, "Injury depth control from combined wavelength and power tuning in scanned beam laser thermal therapy." *Journal of biomedical optics*, vol. 16, no. 11, p. 118001, 2011.

[26] K. Mönkemüller, "Radiofrequency Ablation for Barrett Esophagus With Confirmed Low-Grade Dysplasia," *JAMA*, vol. 311, no. 12, pp. 1205–1206, 2014.

[27] W. L. Curvers, L. A. Herrero, M. B. Wallace, L. M. Wong Kee Song, K. Ragunath, H. C. Wolfsen, G. A. Prasad, K. K. Wang, V. Subramanian, B. L. A. M. Weusten, F. J. Ten Kate, and J. J. G. H. M. Bergman, "Endoscopic tri-modal imaging is more effective than standard endoscopy in identifying early-stage neoplasia in Barrett's esophagus," *Gastroenterology*, vol. 139, no. 4, pp. 1106–1114.e1, 2010.

[28] H. Pahlevaninezhad, A. M. D. Lee, G. Hohert, S. Lam, T. Shaipanich, E.-L. Beaudoin, C. MacAulay, C. Boudoux, and P. Lane, "Endoscopic high-resolution autofluorescence imaging and OCT of pulmonary vascular networks," *Optics Letters*, vol. 41, no. 14, pp. 3209–3212, 2016.

[29] V. Kumar, A. K. Abbas, N. Fausto, and J. C. Aster, *Robbins and Cotran pathologic basis of disease*. Elsevier Health Sciences, 2014.

[30] N. R. Barrett, "Chronic peptic ulcerz of the œophagus and 'œsophagitis'," *British Journal of Surgery*, vol. 38, no. 150, pp. 175–182, 1950.

[31] N. J. Shaheen and J. E. Richter, "Barrett's oesophagus." *Lancet*, vol. 373, no. 9666, pp. 850–61, 2009.

[32] M. Choma, M. Sarunic, C. Yang, and J. A. Izatt, "Sensitivity advantage of swept source and Fourier domain optical coherence tomography." *Optics express*, vol. 11, no. 18, pp. 2183–9, 2003.

[33] S. Yun, G. Tearney, J. de Boer, N. Iftimia, and B. E. Bouma, "High-speed optical frequency-domain imaging." *Optics express*, vol. 11, no. 22, pp. 2953–63, 2003.

[34] A. Sergeev, V. Gelikonov, G. Gelikonov, F. Feldchtein, R. Kuranov, N. Gladkova, N. Shakhova, L. Snopova, A. Shakhov, I. Kuznetzova, A. Denisenko, V. Pochinko, Y. Chumakov, and O. Streltzova, "In vivo endoscopic OCT imaging of precancer and cancer states of human mucosa." *Optics express*, vol. 1, no. 13, pp. 432–40, 1997.

[35] S. Jäckle, N. Gladkova, and F. Feldchtein, "In Vivo Endoscopic Optical Coherence Tomography of the Human Gastrointestinal Tract- Toward Optical Biopsy," *Endoscopy*, vol. 32, no. 10, pp. 743–749, 2000.

[36] M. Tsuboi, A. Hayashi, N. Ikeda, H. Honda, Y. Kato, S. Ichinose, and H. Kato, "Optical coherence tomography in the diagnosis of bronchial lesions." *Lung cancer (Amsterdam, Netherlands)*, vol. 49, no. 3, pp. 387–94, 2005.

[37] C. Pitris, A. Goodman, S. A. Boppart, J. J. Libus, J. G. Fujimoto, and M. E. Brezinski, "High-resolution imaging of gynecologic neoplasms using optical coherence tomography," *Obstetrics & Gynecology*, vol. 93, no. 1, pp. 135–139, 1999.

[38] C. Jesser and S. Boppart, "High resolution imaging of transitional cell carcinoma with optical coherence tomography : feasibility for the evaluation of bladder pathology." *The British journal of Radiology*, vol. 72, no. December, 1999.

[39] B. Bouma and G. Tearney, "High-resolution imaging of the human esophagus and stomach in vivo using optical coherence tomography," *Gastrointestinal Endoscopy*, vol. 51, no. 4, 2000.

[40] S. H. Yun, G. J. Tearney, B. J. Vakoc, M. Shishkov, W. Y. Oh, A. E. Desjardins, M. J. Suter, R. C. Chan, J. A. Evans, I.-K. Jang, N. S. Nishioka, J. F. de Boer, and B. E. Bouma, "Comprehensive volumetric optical microscopy in vivo." *Nature medicine*, vol. 12, no. 12, pp. 1429–33, 2006.

[41] H. W. Baac, N. Uribe-Patarroyo, and B. E. Bouma, "High-energy pulsed Raman fiber laser for biological tissue coagulation," *Optics Express*, vol. 22, no. 6, p. 7113, 2014.

[42] D. Manstein, G. S. Herron, R. K. Sink, H. Tanner, and R. R. Anderson, "Fractional photothermolysis : A new concept for cutaneous remodeling using microscopic patterns of thermal injury," *Lasers in Surgery and Medicine*, vol. 34, no. 5, pp. 426–438, 2004.

[43] S. L. Trokel, R. Srinivasan, and B. Braren, "Excimer laser surgery of the cornea," *American Journal of Opthalmology*, vol. 96, no. 6, pp. 710–715, 1983.

[44] A. Welch and M. V. Gemert, *Optical-thermal response of laser-irradiated tissue*, 2nd ed., A. Welch and M. van Gemert, Eds. Dordrecht : Springer Netherlands, 2011. [Online]. Available : http://link.springer.com/book/10.1007%2F978-90-481-8831-4

[45] R. J. Stafford, D. Fuentes, A. A. Elliott, J. S. Weinberg, and K. Ahrar, "Laser-induced thermal therapy for tumor ablation," *Critical Reviews^{TM} in Biomedical Engineering*, vol. 38, no. 1, 2010.

[46] N. M. Fried, "High-power laser vaporization of the canine prostate using a 110 W thulium fiber laser at 1.91 μm," *Lasers in Surgery and Medicine*, vol. 36, no. 1, pp. 52–56, 2005.

[47] G. S. Dulai, "Surveying the case for surveillance." *Gastroenterology*, vol. 122, no. 3, pp. 820–3, 2002.

[48] B. Chen, S. L. Thomsen, R. J. Thomas, and A. J. Welch, "Modeling thermal damage in skin from 2000-nm laser irradiation." *Journal of biomedical optics*, vol. 11, no. 6, p. 064028, 2006.

[49] C. Barham, R. Jones, and L. Biddlestone, "Photothermal laser ablation of Barrett's oesophagus : endoscopic and histological evidence of squamous re-epithelialisation," *Gut*, vol. 41, pp. 281–284, 1997.

[50] L. Gossner, A. May, M. Stolte, G. Seitz, E. G. Hahn, and C. Ell, "KTP laser destruction of dysplasia and early cancer in columnar-lined Barrett's esophagus," *Gastrointestinal Endoscopy*, vol. 49, no. 1, pp. 8–12, 1999.

[51] M. H. Johnston, "Technology insight : ablative techniques for Barrett's esophagus—current and emerging trends," *Nature Clinical Practice Gastroenterology & Hepatology*, vol. 2, no. 7, pp. 323–330, 2005.

[52] D. E. Fleischer, R. Odze, B. F. Overholt, J. Carroll, K. J. Chang, A. Das, J. Goldblum, D. Miller, C. J. Lightdale, J. Peters, R. Rothstein, V. K. Sharma, D. Smith, V. Velanovich, H. Wolfsen, and G. Triadafilopoulos, "The case for endoscopic treatment of non-dysplastic and low-grade dysplastic Barrett's esophagus." *Digestive diseases and sciences*, vol. 55, no. 7, pp. 1918–31, 2010.

[53] J. De Boer, S. Srinivas, A. Malekafzali, Z. Chen, and J. Nelson, "Imaging thermally damaged tissue by Polarization Sensitive Optical Coherence Tomography." *Optics express*, vol. 3, no. 6, pp. 212–8, 1998.

[54] S. A. Boppart, J. Herrmann, C. Pitris, D. L. Stamper, M. E. Brezinski, and J. G. Fujimoto, "High-resolution optical coherence tomography-guided laser ablation of surgical tissue." *The Journal of surgical research*, vol. 82, no. 2, pp. 275–84, 1999.

[55] H. H. Müller, L. Ptaszynski, K. Schlott, C. Debbeler, M. Bever, S. Koinzer, R. Birngruber, R. Brinkmann, and G. Hüttmann, "Imaging thermal expansion and retinal tissue changes during photocoagulation by high speed OCT." *Biomedical optics express*, vol. 3, no. 5, pp. 1025–46, 2012.

[56] B. J. Vakoc, G. J. Tearney, and B. E. Bouma, "Real-time microscopic visualization of tissue response to laser thermal therapy." *Journal of biomedical optics*, vol. 12, no. 2, p. 020501, 2007.

[57] W. C. Y. Lo, N. Uribe-Patarroyo, A. S. Nam, M. Villiger, B. J. Vakoc, and B. E. Bouma, "Laser thermal therapy monitoring using complex differential variance in optical coherence tomography." *Journal of Biophotonics*, vol. 8, pp. 1–8, 2016.

[58] N. A. Patel, X. Li, D. L. Stamper, J. G. Fujimoto, and M. E. Brezinski, "Guidance of aortic ablation using optical coherence tomography." *The international journal of cardiovascular imaging*, vol. 19, no. 2, pp. 171–8, 2003.

[59] B. Y. C. Leung, P. J. L. Webster, J. M. Fraser, and V. X. D. Yang, "Real-time guidance of thermal and ultrashort pulsed laser ablation in hard tissue using inline coherent imaging." *Lasers in surgery and medicine*, vol. 44, no. 3, pp. 249–56, 2012.

[60] C. A. Banzhaf, B. S. Wind, M. Mogensen, A. A. Meesters, U. Paasch, A. Wolkerstorfer, and M. Haedersdal, "Spatiotemporal closure of fractional laser-ablated channels imaged by optical coherence tomography and reflectance confocal microscopy." *Lasers in surgery and medicine*, no. June, pp. 1–9, 2015.

[61] T.-H. Tsai, C. Zhou, Y. K. Tao, H.-C. Lee, O. O. Ahsen, M. Figueiredo, T. Kirtane, D. C. Adler, J. M. Schmitt, Q. Huang, J. G. Fujimoto, and H. Mashimo, "Structural markers observed with endoscopic 3-dimensional optical coherence tomography correlating with Barrett's esophagus radiofrequency ablation treatment response (with videos)." *Gastrointestinal endoscopy*, vol. 76, no. 6, pp. 1104–12, 2012.

[62] C. Zhou, T.-H. Tsai, H.-C. Lee, T. Kirtane, M. Figueiredo, Y. K. Tao, O. O. Ahsen, D. C. Adler, J. M. Schmitt, Q. Huang, J. G. Fujimoto, and H. Mashimo, "Characterization of buried glands before and after radiofrequency ablation by using 3-dimensional optical coherence tomography (with videos)." *Gastrointestinal endoscopy*, vol. 76, no. 1, pp. 32–40, 2012.

[63] S. D. Murgu and H. G. Colt, "Combined Optical Coherence Tomography and Endobronchial Ultrasonography for Laser-Assisted Treatment of Postintubation Laryngotracheal Stenosis," *Annals of Otology, Rhinology and Laryngology*, vol. 122, no. 5, pp. 299–307, 2013.

[64] Z. Li, J. H. Shen, J. A. Kozub, R. Prasad, P. Lu, and K. M. Joos, "Miniature forward-imaging B-scan optical coherence tomography probe to guide real-time laser ablation." *Lasers in surgery and medicine*, vol. 46, no. 3, pp. 193–202, 2014.

[65] N. Thekkek, S. Anandasabapathy, and R. Richards-Kortum, "Optical molecular imaging for detection of Barrett's-associated neoplasia," *World Journal of Gastroenterology*, vol. 17, no. 1, pp. 53–62, 2011.

[66] M. A. Kara, R. S. Dacosta, C. J. Streutker, N. E. Marcon, J. J. G. H. M. Bergman, and B. C. Wilson, "Characterization of tissue autofluorescence in Barrett's esophagus by confocal fluorescence microscopy," *Diseases of the Esophagus*, vol. 20, no. 2, pp. 141–150, 2007.

[67] G. H. Patterson, S. M. Knobel, P. Arkhammar, O. Thastrup, and D. W. Piston, "Separation of the glucose-stimulated cytoplasmic and mitochondrial NAD(P)H responses in pancreatic islet beta cells." *Proceedings of the National Academy of Sciences of the United States of America*, vol. 97, no. 10, pp. 5203–7, 2000.

[68] R. Benson, R. Meyer, M. Zaruba, and G. M. McKhann, "Cellular autofluorescence–is it due to flavins ?" *Journal of Histochemistry & Cytochemistry*, vol. 27, no. 1, pp. 44–48, 1979.

[69] C. Yang, V. W. Hou, E. J. Girard, L. Y. Nelson, and E. J. Seibel, "Target-to-background enhancement in multispectral endoscopy with background autofluorescence mitigation for quantitative molecular imaging," *J Biomed Opt*, vol. 19, no. 7, p. 76014, 2014.

[70] D. M. Harris and J. Werkhaven, "Endogenous porphyrin fluorescence in tumors," *Lasers in Surgery and Medicine*, vol. 7, no. 6, pp. 467–472, 1987.

[71] J. A. Holz, D. F. Boerwinkel, S. L. Meijer, M. Visser, T. G. van Leeuwen, M. C. Aalders, and J. J. Bergman, "Optimized endoscopic autofluorescence spectroscopy for the identification of premalignant lesions in Barrett's oesophagus," *European Journal of Gastroenterology & Hepatology*, vol. 25, pp. 1442–1449, 2013.

[72] D. F. Boerwinkel, J. A. Holz, M. C. G. Aalders, M. Visser, S. L. Meijer, M. I. Van Berge Henegouwen, B. L. A. M. Weusten, and J. J. G. H. M. Bergman, "Third-generation autofluorescence endoscopy for the detection of early neoplasia in Barrett's esophagus : A pilot study," *Diseases of the Esophagus*, vol. 27, no. 3, pp. 276–284, 2014.

[73] H. Pahlevaninezhad, A. M. D. Lee, S. Lam, C. MacAulay, and P. M. Lane, "Coregistered autofluorescence-optical coherence tomography imaging of human lung sections." *Journal of biomedical optics*, vol. 19, no. 3, p. 36022, 2014.

[74] H. Pahlevaninezhad, A. M. D. Lee, T. Shaipanich, R. Raizada, L. Cahill, G. Hohert, V. X. D. Yang, S. Lam, C. MacAulay, and P. Lane, "A high-efficiency fiber-based

imaging system for co-registered autofluorescence and optical coherence tomography," *Biomedical Optics Express*, vol. 5, no. 9, p. 2978, 2014.

[75] L. Zenteno, "High-power double-clad fiber lasers," *Journal of Lightwave Technology*, vol. 11, no. 9, pp. 1435–1446, 1993.

[76] D. Yelin, B. E. Bouma, S. H. Yun, and G. J. Tearney, "Double-clad fiber for endoscopy." *Optics letters*, vol. 29, no. 20, pp. 2408–10, 2004.

[77] S. Lemire-Renaud, M. Strupler, F. Benboujja, N. Godbout, and C. Boudoux, "Double-clad fiber with a tapered end for confocal endomicroscopy." *Biomedical optics express*, vol. 2, no. 11, pp. 2961–72, 2011.

[78] S. Y. Ryu, H. Y. Choi, J. Na, E. S. Choi, and B. H. Lee, "Combined system of optical coherence tomography and fluorescence spectroscopy based on double-cladding fiber." *Optics letters*, vol. 33, no. 20, pp. 2347–9, 2008.

[79] H. Yoo, J. W. Kim, M. Shishkov, E. Namati, T. Morse, R. Shubochkin, J. R. McCarthy, V. Ntziachristos, B. E. Bouma, F. A. Jaffer, and G. J. Tearney, "Intra-arterial catheter for simultaneous microstructural and molecular imaging in vivo." *Nature medicine*, vol. 17, no. 12, pp. 1680–4, 2011.

[80] J. Mavadia, J. Xi, Y. Chen, and X. Li, "An all-fiber-optic endoscopy platform for simultaneous OCT and fluorescence imaging." *Biomedical optics express*, vol. 3, no. 11, pp. 2851–9, 2012.

[81] D. Lorenser, B. C. Quirk, M. Auger, W.-J. Madore, R. W. Kirk, N. Godbout, D. D. Sampson, C. Boudoux, and R. A. McLaughlin, "Dual-modality needle probe for combined fluorescence imaging and three-dimensional optical coherence tomography." *Optics letters*, vol. 38, no. 3, pp. 266–8, 2013.

[82] A. M. Fard, P. Vacas-Jacques, E. Hamidi, H. Wang, R. W. Carruth, J. A. Gardecki, and G. J. Tearney, "Optical coherence tomography – near infrared spectroscopy system and catheter for intravascular imaging," *Optics Express*, vol. 21, no. 25, p. 30849, 2013.

[83] M. T. Myaing, J. Y. Ye, T. B. Norris, T. Thomas, J. R. Baker, W. J. Wadsworth, G. Bouwmans, J. C. Knight, and P. S. J. Russell, "Enhanced two-photon biosensing with double-clad photonic crystal fibers." *Optics letters*, vol. 28, no. 14, pp. 1224–6, 2003.

[84] L. Fu, X. Gan, and M. Gu, "Nonlinear optical microscopy based on double-clad photonic crystal fibers." *Optics express*, vol. 13, no. 14, pp. 5528–34, 2005.

[85] L. Fu and M. Gu, "Double-clad photonic crystal fiber coupler for compact nonlinear optical microscopy imaging." *Optics letters*, vol. 31, no. 10, pp. 1471–3, 2006.

[86] T. Xie, D. Mukai, S. Guo, M. Brenner, and Z. Chen, "Fiber-optic-bundle-based optical coherence tomography." *Optics letters*, vol. 30, no. 14, pp. 1803–5, 2005.

[87] J.-H. Han and J. U. Kang, "Effect of multimodal coupling in imaging micro-endoscopic fiber bundle on optical coherence tomography." *Applied physics. B, Lasers and optics*, vol. 106, no. 3, pp. 635–643, 2012.

[88] S. Moon and Z. Chen, "Mode-filtered large-core fiber for optical coherence tomography." *Applied Optics*, vol. 51, no. 34, pp. 8262–70, 2012.

[89] S. Liang, A. Saidi, J. Jing, G. Liu, J. Li, J. Zhang, C. Sun, J. Narula, and Z. Chen, "Intravascular atherosclerotic imaging with combined fluorescence and optical coherence tomography probe based on a double-clad fiber combiner." *Journal of biomedical optics*, vol. 17, no. 7, p. 070501, 2012.

[90] B. B. Zhang and H. Zhang, "Fiber optic rotary coupler," U.S. Patent Application No. 12/042,126, 2008.

[91] W. Kim, X. Chen, J. A. Jo, and B. E. Applegate, "Lensless, ultra-wideband fiber optic rotary joint for biomedical applications," *Optics Letters*, vol. 41, no. 9, p. 1973, 2016.

[92] S. Lee, M. W. Lee, H. S. Cho, J. W. Song, H. S. Nam, D. J. Oh, K. Park, W.-Y. Oh, H. Yoo, and J. W. Kim, "Fully Integrated High-Speed Intravascular Optical Coherence Tomography/Near-Infrared Fluorescence Structural/Molecular Imaging In Vivo Using a Clinically Available Near-Infrared Fluorescence-Emitting Indocyanine Green to Detect Inflamed Lipid-Rich Atherom," *Circulation. Cardiovascular interventions*, vol. 7, no. 4, pp. 560–9, 2014.

[93] E. De Montigny, W.-J. Madore, O. Ouellette, G. Bernard, M. Leduc, M. Strupler, C. Boudoux, and N. Godbout, "Double-clad fiber coupler for partially coherent detection," *Optics Express*, vol. 23, no. 7, p. 9040, 2015.

[94] L. Wang, H. Y. Choi, Y. Jung, B. H. Lee, and K.-T. Kim, "Optical probe based on double-clad optical fiber for fluorescence spectroscopy." *Optics express*, vol. 15, no. 26, pp. 17 681–9, 2007.

[95] F. F. Gonthier, L. Martineau, N. Azami, M. Faucher, F. Séguin, D. Stryckman, A. Villeneuve, and F. Seguin, "High-power All-Fiber components : the missing link for high-power fiber lasers," in *Proc. SPIE 5335, Fiber Lasers : Technology, Systems, and Applications*, vol. 5335, 2004, pp. 266–276. [Online]. Available : http://dx.doi.org/10.1117/12.548946

[96] G. Liu and Z. Chen, "Fiber-based combined optical coherence and multiphoton endomicroscopy." *Journal of biomedical optics*, vol. 16, no. 3, p. 036010, 2011.

[97] Y. Wu, J. Xi, M. J. Cobb, and X. Li, "Scanning fiber-optic nonlinear endomicroscopy with miniature aspherical compound lens and multimode fiber collector." *Optics letters*, vol. 34, no. 7, pp. 953–5, 2009.

[98] J. Xi, Y. Chen, Y. Zhang, K. Murari, M.-J. Li, and X. Li, "Integrated multimodal endomicroscopy platform for simultaneous en face optical coherence and two-photon fluorescence imaging." *Optics letters*, vol. 37, no. 3, pp. 362–4, 2012.

[99] M. Shishkov, G. J. Tearney, and B. E. Bouma, "Scultpured optical fiber tips for narrow diameter optical catheters," in *Biomedical Topical Meeting*. Optical Society of America, 2004, p. SE5.

[100] S. L. Jacques, "Role of tissue optics and pulse duration on tissue effects during high-power laser irradiation." *Applied optics*, vol. 32, no. 13, pp. 2447–54, 1993.

[101] M. Tsai, C. Yang, S. Shen, F. Chang, J. Lee, J. Yi, and C. Fan, "Noninvasive characterization of fractional photothermolysis induced by ablative and non-ablative lasers with optical coherence tomography," *Laser Physics*, vol. 23, 2013.

[102] C. Boudoux, "Wavelength Swept Spectrally Encoded Confocal Microscopy for Biological and Clinical Applications," Ph.D. dissertation, Harvard Medical School, 2007.

[103] S.-Y. Ryu, H.-Y. Choi, M.-J. Ju, J.-H. Na, W.-J. Choi, and B.-H. Lee, "The Development of Double Clad Fiber and Double Clad Fiber Coupler for Fiber Based Biomedical Imaging Systems," *Journal of the Optical Society of Korea*, vol. 13, no. 3, pp. 310–315, 2009.

[104] S. Lacroix, N. Godbout, and X. Daxhelet, "Optical fiber components : design and applications of fused biconical tapered components," *Research Signpost, Kerala, India*," 2006.

[105] S. H. Yun, G. J. Tearney, J. F. de Boer, and B. E. Bouma, "Removing the depth-degeneracy in optical frequency domain imaging with frequency shifting," *Optics Express*, vol. 12, no. 20, p. 4822, 2004.

[106] S. H. Yun, C. Boudoux, G. J. Tearney, and B. E. Bouma, "High-speed wavelength-swept semiconductor laser with a polygon-scanner-based wavelength filter." *Optics letters*, vol. 28, no. 20, pp. 1981–3, 2003.

[107] W. C. Lin, M. Motamedi, and A. J. Welch, "Dynamics of tissue optics during laser heating of turbid media." *Applied Optics*, vol. 35, no. 19, pp. 3413–20, 1996.

[108] K. Beaudette, W. Lo, M. Villiger, M. Shishkov, N. Godbout, B. E. Bouma, and C. Boudoux, "Towards in vivo laser coagulation and concurrent optical coherence tomography through double-clad fiber devices," in *Proc. SPIE 9701, Multimodal Biomedical Imaging XI*, 2016, p. 97010B.

[109] G. van Soest, J. G. Bosch, and A. F. W. van der Steen, "Azimuthal registration of image sequences affected by nonuniform rotation distortion," *IEEE Transactions on Information Technology in Biomedicine*, vol. 12, no. 3, pp. 348–355, 2008.

[110] L. Wang, S. L. Jacques, and L. Zheng, "MCML - Monte Carlo modeling of light transport in multi-layered tissues," *Computer Methods and Programs in Biomedicine*, vol. 47, pp. 131–146, 1995.

[111] S. Thomsen and J. A. Pearce, "Thermal damage and rate processes in biologic tissues," in *Optical-thermal response of laser-irradiated tissue*, 2nd ed. Springer, 2011, pp. 487–549. [Online]. Available : http://link.springer.com/chapter/10.1007/978-90-481-8831-4_13

[112] D. M. Wieliczka, S. Weng, and M. R. Querry, "Wedge shaped cell for highly absorbent liquids : infrared optical constants of water." *Applied Optics*, vol. 28, no. 9, pp. 1714–1719, 1989.

[113] M. H. Khan, R. K. Sink, D. Manstein, D. Eimerl, and R. R. Anderson, "Intradermally focused infrared laser pulses : thermal effects at defined tissue depths." *Lasers in surgery and medicine*, vol. 36, no. 4, pp. 270–80, 2005.

[114] T. Collier, M. Follen, A. Malpica, and R. Richards-Kortum, "Sources of scattering in cervical tissue : determination of the scattering coefficient by confocal microscopy." *Applied optics*, vol. 44, no. 11, pp. 2072–81, 2005.

[115] B.-M. Kim, S. L. Jacques, S. Rastegar, S. Thomsen, and M. Motamedi, "Nonlinear finite-element analysis of the role of dynamic changes in blood perfusion and optical properties in laser coagulation of tissue," *IEEE Journal of Selected Topics in Quantum Electronics*, vol. 2, no. 4, pp. 922–933, 1996.

[116] J. W. Valvano, "Tissue thermal properties and perfusion," in *Optical-thermal response of laser-irradiated tissue*, 2nd ed. Springer, 2011, pp. 455–485. [Online]. Available : http://link.springer.com/chapter/10.1007/978-90-481-8831-4_12

[117] S. Puccini, N.-K. Bär, M. Bublat, T. Kahn, and H. Busse, "Simulations of thermal tissue coagulation and their value for the planning and monitoring of laser-induced interstitial thermotherapy (LITT)." *Magnetic resonance in medicine : official journal of the Society of Magnetic Resonance in Medicine / Society of Magnetic Resonance in Medicine*, vol. 49, no. 2, pp. 351–62, 2003.

[118] C. P. Cain, G. D. Polhamus, W. P. Roach, D. J. Stolarski, K. J. Schuster, K. L. Stockton, B. A. Rockwell, B. Chen, and A. J. Welch, "Porcine skin visible lesion thresholds for near-infrared lasers including modeling at two pulse durations and spot sizes." *Journal of biomedical optics*, vol. 11, no. 4, p. 041109, 2006.

[119] R. Neumann, R. Knobler, F. Pieczkowski, and W. Gebhart, "Enzyme histochemical analysis of cell viability after argon laser-induced coagulation necrosis of the skin," *Journal of the American Academy of Dermatology*, vol. 25, no. 6, pp. 991–998, 1991.

[120] Princetel Inc., "Products : Fiber optic rotary joints, N/A," [Accessed : 2017-04-07]. [Online]. Available : http://www.princetel.com/product_forj.asp

[121] W. C. Y. Lo, N. Uribe-Patarroyo, , K. Hoebel, K. Beaudette, M. Villiger, A. S. Nam, N. S. Nishioka, B. J. Vakoc, and B. E. Bouma, "Microscopic image guidance : Balloon catheter-based radiofrequency ablation monitoring for epithelial lesions using optical coherence tomography," *In preparation*," 2017.

[122] M. Li, C. P. Anastassiades, B. Joshi, C. M. Komarck, C. Piraka, B. J. Elmunzer, D. K. Turgeon, T. D. Johnson, H. Appelman, D. G. Beer, and T. D. Wang, "Affinity peptide for targeted detection of dysplasia in barrett's esophagus," *Gastroenterology*, vol. 139, no. 5, pp. 1472–1480, 2010.

[123] M. B. Sturm, B. P. Joshi, S. Lu, C. Piraka, S. Khondee, B. J. Elmunzer, R. S. Kwon, D. G. Beer, H. D. Appelman, D. K. Turgeon, and T. D. Wang, "Targeted imaging of esophageal neoplasia with a fluorescently labeled peptide : first-in-human results." *Science translational medicine*, vol. 5, no. 184, p. 184ra61, 2013.

[124] K. Beaudette, H. W. Baac, W.-J. Madore, M. Villiger, N. Godbout, B. E. Bouma, and C. Boudoux, "Laser tissue coagulation and concurrent optical coherence tomography through a double-clad fiber coupler," *Biomedical Optics Express*, vol. 6, no. 4, p. 1293, 2015.

[125] Zemax LLC, *OpticStudio 16.5 SP3 Help Files*, February 2017. [Online]. Available : www.zemax.com

APPENDIX A GRADIENT INDEX DEFINITION IN ZEMAX

There are several ways to define a gradient index profile and no consensus among GRIN lenses manufacturers. Here, we define the different notations used to describe a gradient index profile, $n(r)$, and relate them to Zemax's definitions [125]. Both sequential and non-sequential modes used the same definitions.

Gradient 1 :

$$n(r) = n_0 + n_{r1}r + n_{r2}r^2, \tag{A.1}$$

where r is the radial position defined as $r^2 = x^2 + y^2$.

Gradient 5 :

$$n_{ref} = n_0 + n_{r2}r^2 + n_{r4}r^4 + n_{z1}z + n_{z2}z^2 + n_{z3}z^3 + n_{z4}z^4. \tag{A.2}$$

This surface is furthermore described by its dispersion data using Sellmeier formula :

$$n(\lambda)^2 = n(\lambda_{ref})^2 + \sum_{i=1}^{3} \frac{K_i(\lambda^2 - \lambda_{ref}^2)}{\lambda^2 - L_i}, \tag{A.3}$$

where

$$K_i = \sum_{j=1}^{K_{MAX}} K_{ij}[n(\lambda_{ref})]^{j-1} \text{ and } L_i = \sum_{j=1}^{L_{MAX}} L_{ij}[n(\lambda_{ref})]^{j-1}. \tag{A.4}$$

This notation is used by GRINTECH GmbH. An example is shown in Table A.1. Dispersion data are available online on their website. In non-sequential mode, *Gradient 5* does not take dispersion data in such that n_0 at the working wavelength should be used.

Table A.1 Parameters describing a GRINTECH lens using the *Gradient 5* notation

Lens	$n_0(\lambda_{ref})$	n_0(1310nm)	n_{r2}	n_{r4}	Material
Rod lens 0.2NA	1.524	1.515	-0.05	1.49e-3	GTLINEU

Gradient 9 :

$$n(r) = n_0 \left[1.0 - \frac{A}{2} r^g\right]. \tag{A.5}$$

In sequential mode, g is set to 2. A and n_0 are defined as a function of the wavelength as :

$$A = \left[K_0 + \frac{K_1}{\lambda^2} + \frac{K_2}{\lambda^4}\right], \tag{A.6}$$

and

$$n_0 = B + \frac{C}{\lambda^2}, \tag{A.7}$$

where the wavelength is provided in micrometers. This notation is used by NSG America, Inc. for all their SELFOC® lenses. Table A.2 specifies some GRIN materials used for the Zemax simulations and their parameters as defined by the *Gradient 9* notation.

Table A.2 Parameters describing SELFOC® lenses using the *Gradient 9* notation

Material	g	B	C	K_0	K_1	K_2
SLW-1.8	2	1.5868	8.14e-3	0.3238	5.364e-3	2.626e-4
SLW-1.0	2	1.5868	8.14e-3	0.5945	3.936e-3	5.539e-4

APPENDIX B LIST OF CONTRIBUTIONS

Articles

1. **K. Beaudette**, M. Strupler, J. Ren, M. Villiger, B. E. Bouma, and C. Boudoux, "Single- and multimode output beams modeling for double-clad fiber applications". In preparation.
2. **K. Beaudette**, M. Villiger, N. Uribe-Patarroyo, B. E. Bouma, and C. Boudoux, "Modeling and optimization of tissue laser coagulation for endoscopic dynamic laser marking". In preparation.
3. X. Liu, **K. Beaudette**, X. Wang, L. Lium, B. E. Bouma, and M. Villiger, "Tissue-like phantoms for quantitative birefringence imaging". In preparation.
4. W. C. Y. Lo, N. Uribe-Patarroyo, , K. Hoebel, **K. Beaudette**, M. Villiger, A. S. Nam, N. S. Nishioka, B. J. Vakoc, and B. E. Bouma, "Microscopic image guidance : Balloon catheter-based radiofrequency ablation monitoring for epithelial lesions using optical coherence tomography," In preparation.
5. F. Benboujja, J. A. Garcia, **K. Beaudette**, M. Strupler, C. J. Hartnick, and C. Boudoux, "Intraoperative imaging of pediatric vocal fold lesions using optical coherence tomography," *Journal of Biomedical Optics*, vol. 21, no. 1, p. 16007, 2016.
6. **K. Beaudette**, H. W. Baac, W.-J. Madore, M. Villiger, N. Godbout, B. E. Bouma, and C. Boudoux, "Laser tissue coagulation and concurrent optical coherence tomography through a double-clad fiber coupler," *Biomedical Optics Express*, vol. 6, no. 4, p. 1293, 2015.

Conference proceedings

1. **K. Beaudette**, W. Lo, M. Villiger, M. Shishkov, N. Godbout, B. E. Bouma, and C. Boudoux, "Towards in vivo laser coagulation and concurrent optical coherence tomography through double-clad fiber devices," in *Proc. SPIE 9701, Multimodal Biomedical Imaging XI*, 2016, p. 97010B.
2. **K. Beaudette**, J. Ren, M. Villiger, M. Strupler, W. Madore, M. Shishkov, N. Godbout, B. E. Bouma, and C. Boudoux, "Towards Endoscopic Image-Guided Laser Coagulation Using a Double-Clad Fiber Coupler," in *CLEO 2015*, 2015, AW4J.5.
3. L. Bernstein, **K. Beaudette**, K. Patten, É. Beaulieu-Ouellet, M. Strupler, F. Moldovan, and C. Boudoux, "Non-invasive imaging of zebrafish with spinal deformities using

optical coherence tomography : a preliminary study," in *Proc. SPIE 8565, Photonic Therapeutics and Diagnostics IX*, 2013, p. 85656H.

Selected oral presentations

1. **Beaudette, K.**, Lo, W., Villiger, M., Bouma, B. E., and Boudoux, C. "Towards double-clad fiber-based endoscopic dynamic laser marking and concurrent optical coherence tomography ", *SPIE Photonics West*, USA, 2017.
2. **Beaudette, K.**, Lo, W., Villiger, M., Shishkov, M., Godbout, N., Bouma, B. E., and Boudoux, C. "Towards in vivo laser coagulation and concurrent optical coherence tomography through double-clad fiber devices", *SPIE Photonics West*, USA, 2016.
3. **Beaudette, K.**, Lo, W., Villiger, M., Shishkov, M., Godbout, N., Bouma, B. E., and Boudoux, C. "Image-guided dynamic laser coagulation using a double-clad fiber-based system", *SPIE Photonics West*, USA, 2016.
4. **Beaudette, K.**, Villiger, M., Strupler, M., Shishkov, M., Ren, J., Madore, W.-J., Godbout, N., Bouma, B. E. and Boudoux, C. "Double clad fiber devices for combined optical coherence tomography and laser coagulation". *SPIE Photonics West*, USA, 2015.
5. Hariri, L. P., Bernstein, L., Adams, D. C., Madore, W.-J., Miller, A. J., Wang, Y., Strupler, M., De Montigny, É., **Beaudette, K.**, Godbout, N., Boudoux, C., and Suter, M. J. "Multimodal optical coherence tomography and fluorescence spectroscopy MEMS probe to assess inflammation in acute lung injury". SPIE Photonics West, USA, 2015.
6. **Beaudette, K.**, Madore, W.-J., De Montigny, É., Baac, H. W., Villiger, M., Godbout, N., Bouma, B. E. and Boudoux, C. "Simultaneous and colocalized optical coherence tomography and laser marking through double-clad fiber". Photonics North, Canada, 2014.
7. **Beaudette, K.**, Baac, H.W., Madore, W.-J., Villiger, M., Godbout, N., Bouma, B. E. and Boudoux, C. "Towards simultaneous and co-localized optical frequency domain imaging and laser therapy through a double clad fiber". SPIE Photonics West, USA, 2014.